Block Copolymer Thin Films: Self-Assembly of Large Molecular Weight Systems and the Fabrication of Novel Metal/Metal Oxide Nanomaterials.

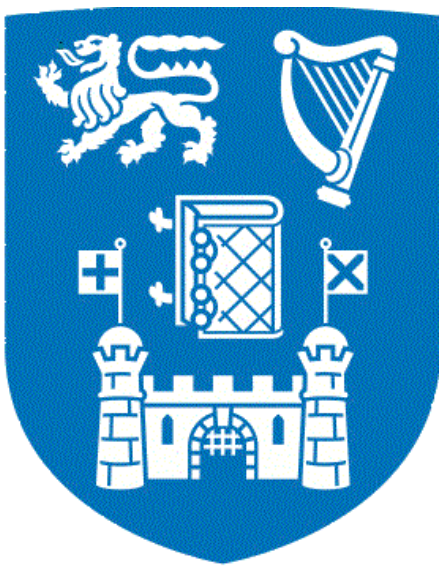

A thesis submitted to the School of Chemistry,

Trinity College Dublin,

For the degree of Doctor of Philosophy

By **Andrew Selkirk, B.Sc. (Hons)**

Supervisor: Prof. Michael A. Morris

Co-supervisor: Dr. Parvaneh Mokarian

2021

Acknowledgements:

I can say without a doubt that the work contained in this thesis would not have been possible without the guidance and support of my colleagues, family, and friends. I sincerely thank every single person who took some time out of their day (no matter how small) to assist me over the past 5 years.

Firstly, I would like to thank my supervisor Prof. Mick Morris for trusting me with the opportunity to work on such interesting projects in an open, friendly, and collaborative group. His advice over the years was invaluable and for this I express my sincere gratitude. I am especially thankful to my co-supervisor, Dr. Parvaneh Mokarian, for being a pillar of support and guidance throughout my studies. I am forever grateful for all the time you took out of your busy schedule to lend me your ideas and thoughts.

I thank Matt Shaw and Richard Twohig for the opportunity to be part of such a fascinating set of research projects. To the postdoctoral researchers both past and present, especially Cian, Ross, Dave, Riley, Brian, and Sajjad, I express my gratitude for the wealth of expertise and general PhD advice you shared with me over the years. I greatly appreciate the support and friendship I received from all my colleagues both in unit 9 and in CRANN, including Nadia, Tom, Eleanor, Elsa, Bríd, Phil, Lipeeka, Aislan, Pravind, Jhonattan, Hande, Niall, Hossein, and Sudhakar. I would like to especially thank Nadia, who, along with providing significant experimental contributions to this work, always kept me level-headed and brought me back to reality when I needed it. A special thanks also to Eleanor, Elsa, Tom and Bríd for all the tea, coffee and (pre-covid) 8am pav breakfasts that always successfully dragged me out of bed.

I would never have reached this final chapter without the unwavering support I have received from my family and friends. To Ana, your friendship and communication has been invaluable. To Seán and Caolán, our trips together were an essential part of energising me to complete this work. My parents Mary and Dave guided me through many of my most difficult moments, and for that I cannot thank them enough. A special thanks to my grandmother Ann for always being supportive of me (and for all the lovely card messages over the past year).

Last (but certainly not least) I thank my partner Carlos for his endless patience and positivity, and for always being there for me.

Abstract:

The self-assembly of block copolymers (BCPs) is considered an excellent candidate to further the development and progression of nanoscale technologies. While lithographic applications remain a primary topic of focus for BCP research, less conventional areas of interest such as optics, catalysis, and sensing present unique challenges to the field. In the case of these aforementioned areas, the advantages of BCP-templated nanostructures include low cost, high scalability, morphological tunability, and large-area ordering. This thesis reports the development of an innovative strategy for the self-assembly of large BCP systems with optics-scale dimensionality, along with expanding the potential of BCP templating via fabricating novel catalytic and sensing materials. Firstly, the rapid self-assembly of a large BCP system (poly(styrene)-*b*-poly-2-vinylpyridine (PS-*b*-P2VP)) into lamellar domains via a controlled solvent vapour annealing (SVA) strategy is detailed. The influence of variables such as the film thickness, SVA time and the rate of swelling on the morphology of the BCP system are analysed. A liquid phase infiltration (LPI) strategy is utilised to convert the lamellar BCP films into a metal oxide hardmask, which is then etched into a Si substrate to create large period nanowall features. The resulting self-assembled BCP films are also utilised for synthesizing 3-dimensional metallic lamellae, again using a LPI strategy. The relationship between the BCP film thickness on the heights of the metal structures is detailed, enabling precise control over the heights of the nanowall structures. These structures are utilised as photocatalytic structures for the degradation of methyl orange, revealing a height-dependent performance relationship. Finally, a novel, multifunctional catalytic device is fabricated and characterised using BCP templating. A PS-*b*-P4VP BCP system is self-assembled into cylindrical domains on an indium-tin oxide (ITO) substrate via SVA, which is then converted into WO_3 nanowires using a LPI strategy. The device is successfully utilised for both water oxidation and highly selective epinephrine detection.

List of Publications:

1) **Selkirk, A.**; Prochukhan, N.; Lundy, R.; Cummins, C.;, Gatensby, R.; Kilbride, R.; Parnell, A.; Vasquez, J. B.; Morris, M.; Mokarian-Tabari, P. Optimization and Control of Large Block Copolymer Self-Assembly via Precision Solvent Vapor Annealing. *Macromolecules* **2021**, 54 (3), 1203-1215.

2) **Selkirk, A.;** Bas, S. Z.; Cummins, C.; Aslan, E.; Patir, E. H.; Zhussupbekova, A.; Prochukhan, N.; Borah, D.; Paiva, A.; Ozmen, M.; Morris, M. Block Copolymer Templated WO_3 Surface Nanowires as Catalysts for Enhanced Epinephrine Sensing and the Oxygen Evolution Reaction. *Electrochimica Acta* **2021**, (under review).

3) Prochukhan, N.; **Selkirk, A.;** Lundy, R.; Giraud, E.; Ghoshal, T.; Downing, C.; Morris, M. Large-Area Fabrication of Vertical Silicon Nanotube Arrays via Toroidal Micelle Self-Assembly. *Langmuir* **2021**, 37 (5), 1932-1940.

4) Lundy, R.; Yadav, P.; **Selkirk, A.;** Mullen, E.; Ghoshal, T.; Cummins, C.; Morris, M. Optimizing Polymer Brush Coverage To Develop Highly Coherent Sub-5 nm Oxide Films by Ion Inclusion. *Chemistry of Materials* **2019**, 31 (22), 9338-9345.

5) Bas, S. Z.; Cummins, C.; **Selkirk, A.;** Borah, D.; Ozmen, M.; Morris, M. A novel electrochemical sensor based on metal ion infiltrated block copolymer thin films for sensitive and selective determination of dopamine. *ACS Applied Nanomaterials* **2019**, 2 (11), 7311-7318.

6) Mir, S. H.; Jennings, B D.; Akinoglu, G. E.; **Selkirk, A.;** Gatensby, R.; Mokarian, P. Enhanced Dye Degradation through Multi-Particle Confinement in a Porous Silicon Substrate: A Highly Efficient, Low Band Gap Photocatalyst. *Advanced Optical Materials* **2021**, 9, 2002238.

7) Ghoshal, T.; Senthamaraikannan, R.; Shaw, M. T.; Lundy, R.; **Selkirk, A.;** Morris, M. Fabrication of Graphoepitaxial Gate-All-Around Si Circuitry Patterned Nanowire Arrays Using Block Copolymer Assisted Hard Mask Approach. *ACS Nano* **2021**, 15 (6), 9550-9558.

8) Lundy, R.; Yadav, P.; Prochukhan, N.; Giraud, E. C.; O'Mahony, T. F.; **Selkirk, A.;** Mullen, E.; Conway, J.; Turner, M.; Danielas, S.; mani-Gonzelez, P. G.; Snelgrove, M.; Bogan, J.; McFeely, C.; O'Connor, R.; McGlynn, E.; Hughes, G.; Cummins, C.; Morris, M. Precise Definition of a "Monolayer Point" in Polymer Brush Films for Fabricating Highly Coherent TiO2 Thin Films by Vapor-Phase Infiltration. *Langmuir* **2020**, 36 (410, 12394-12402.

Table of Contents:

Chapter 1. Introduction **1**

1.1. Block copolymer Self-Assembly – Overview and Challenges 1
1.2. Polymer Structures and Families 2
1.3. Theory of Block Copolymer Self-Assembly 4
1.3.1. Film Thickness and Interfacial Effects 6
1.4. Experimental Strategies for Self-Assembly 7
1.4.1. Thermal Annealing 8
1.4.2. Solvent Vapour Annealing 8
1.5. Inorganic Nanostructures via Block Copolymer Templates 11
1.5.1. Vapour Phase Infiltration 12
1.5.2. Liquid Phase Infiltration 14
1.6. Thesis Overview 17

Chapter 2. Optimization and Control of Large Block Copolymer Self-Assembly via Precision Solvent Vapor Annealing **27**

2.1. Abstract 27
2.2. Introduction 28
2.3. Experimental Section 31
2.3.1. Materials & Sample Preparation 31
2.3.2. Annealing Rig 31
2.3.3. SVA Process 32
2.3.4. Oxide Nanostructure Formation, Pattern Transfer 32
2.3.5. Sample Characterisation 33
2.3.6. Image Analysis 33
2.4. Results and Discussion 34
2.5. Conclusion 49
2.6. References 51
2.7. Appendix – Chapter 2 56

Chapter 3. Large Period 3-Dimensional Metallic Lamellae with Tailored Thickness via Liquid Phase Infiltration of a Block Copolymer Film 69

3.1. Abstract 69
3.2. Introduction 69
3.3. Experimental Section 72
3.3.1 Materials 72
3.3.2. Au, Pt 3D nanostructure preparation 72
3.3.3. MO Photocatalytic degradation: 73
3.3.4. Sample Characterisation 73
3.4. Results and Discussion 74
3.5. Conclusion 83
3.6. References 84
3.7. Appendix – Chapter 3 87

Chapter 4. Block Copolymer Templated WO_3 Surface Nanowires as Catalysts for Enhanced Epinephrine Sensing and the Oxygen Evolution Reaction 88

4.1. Abstract 88
4.2. Introduction 88
4.3. Experimental Section 90
4.3.1. Reagents 90
4.3.2. Fabrication of WO_3NWs-ITO electrode 91
4.3.3. Apparatus and Instrumentation 91
4.4. Results and Discussion 92
4.4.1. Electrode preparation and characterization: 92
4.4.2. Water Oxidation Properties 95
4.4.3. Epinephrine Sensing Properties 97
4.5. Conclusion 103
4.6. References 104
4.7. Appendix – Chapter 4 109

Chapter 5. Conclusions and Future Work **111**

5.2. References 114

List of Common Abbreviations and Acronyms:

AFM: Atomic Force Microscopy

BCP: Block Copolymer

***f*:** Block volume fraction

EIS: Electronic Impedance Spectrometry

EP: Epinephrine

GISAXS: Grazing Incidence Small Angle X-ray Scattering

ICP: Inductively Coupled Plasma

ITO: Indium Tin Oxide

LPI: Liquid Phase Infiltration

LSV: Linear Sweep Voltammetry

***N*:** Degree of Polymerization

OER: Oxygen Evolution Reaction

PxVP: Poly(*x*-vinylpyridine)

PS: Poly(styrene)

PMMA: Poly(methyl methacrylate)

SEM: Scanning Electron Microscopy

Si: Silicon

SIS: Sequential Infiltration Synthesis

SMO: Semiconducting Metal Oxide

SVA: Solvent Vapour Annealing

VPI: Vapour Phase Infiltration

χ: Flory-Huggins interaction parameter

ϕ_s: Solvent concentration in polymer film

ξ: Correlation length

1. Introduction

1.1 Block Copolymer Self-Assembly – Overview & Challenges

Materials with the ability to self-assemble and self-organise are critical to the development of scalable and cost-effective nanofabrication technologies of the future. 'Bottom-up' strategies to develop these self-assembled materials are becoming increasingly relevant as economically viable candidates for the generation of tailored nanostructures for industrial purposes.[1] Scalability and the lack of necessity for expensive manufacturing equipment makes these strategies inherently attractive compared to conventional 'top-down' approaches.[1] There exists a plethora of bottom-up self-assembly approaches, including colloidal,[2, 3] DNA,[4] and polymer phase separation[5, 6] to name a few. Block copolymer (BCP) self-assembly, in particular, is arguably the most suitable of these bottom-up approaches for attaining the key criteria for future nanomanufacturing.[6] The advantages of BCP-based self-assembly include a diverse range of potential architectures, low production costs, rapid processing time and high degree of scalability.[6]

The self-assembly of BCPs arises from the ability of the incompatible blocks within the polymer chain to microphase separate into nanometre-sized structures. Microphase separation is a highly intricate process, with the resulting BCP morphology governed by numerous interdependent variables including the molecular weight of the polymer chains, the degree of repulsion between the constituent blocks, substrate chemistry, film deposition kinetics, annealing method, among many others.[7-10] A significant portion of the BCP-based research has focussed on understanding and controlling the thermodynamic mechanism of microphase separation. As a result, there have been significant advances in recent years using a variety of self-assembly strategies, which include thermal annealing,[11] solvent vapour annealing (SVA),[12, 13] laser annealing,[14] electric field,[15, 16] or a combination of these.[17, 18] Such advances have enabled the controlled synthesis of a myriad of thin film and bulk morphologies utilising a variety of polymer block chemistries.

The ability to controllably self-assemble into ordered patterns and structures has enabled BCP-based nanopatterning to meet many of the fundamental criteria for industrial nanomanufacturing.[6]

The list of potential applications is extensive and ever-evolving – spanning a range of fields such as integrated circuits,[19] nanoporous membranes,[20] nanostructured electrocatalytic systems,[21, 22] nanotextured surfaces such as antireflective coatings,[23-25] photonic crystals,[26-29] to name a few. Nonetheless, there exists several critical roadblocks that must be addressed or circumvented in order to facilitate large-scale industrial uptake. The primary focal points of contemporary BCP research encompass many of these challenges – some examples include further optimization of the self-assembly process,[30] controlling defect formation,[31, 32] engineering of novel BCP materials,[33] enhancing the selective infiltration of metal precursors,[34] and further expanding the domain size restrictions beyond the 5—200 nm limit.[35, 36]

1.2 Polymer Structures & Families

In the most simplistic description, polymers are chemical structures composed of repeating individual units known as monomers that are bonded together to form a chain. The polymer chains may be linear, or alternatively they may branch out and/or recombine into multiple sub-chains. The four fundamental types of polymer structures are shown below in **figure 1.1**; they consist of linear, branched, crosslinked, and network polymers**.** Many structurally idiosyncratic sub-types exist, including dendritic, cyclic, star, and graft polymers; nevertheless, all of these sub-types are understood to fit into one or more of the four aforementioned polymer structures.

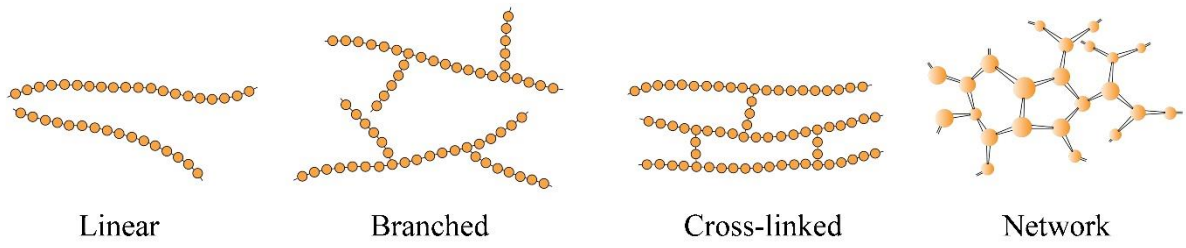

Figure 1.1. Diagrams of the four basic polymer structures. Adapted from Fig. 4.7, Callister & Rethwisch 5th edit.[37]

In an additional layer of complexity, the constituent monomers may either be completely identical across a single chain or consist of alternating chemically dissimilar groups. In the case where two or more chemically distinct monomers are present on a single chain, the polymer is referred to as a copolymer. The precise monomeric arrangement of copolymers can be somewhat ordered or entirely random, which allows for an incalculable number of structural iterations. These iterations can be indexed into four principal types of copolymers as outlined in **figure 1.2**. Note that the examples shown in **figure 1.2** are for the case of a 'bipolymer', i.e., a polymer consisting of two monomer species. In the case of copolymers containing 3 or more constituent monomer species (such as terpolymers, quaterpolymers, etc.), a greater number of variations can exist, however these may also typically be categorised into the four types shown below.

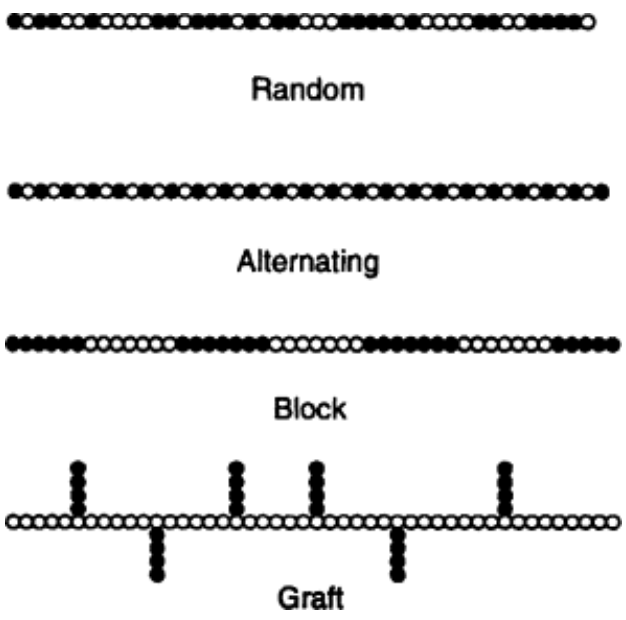

Figure 1.2. The four principal types of copolymers. Adapted from Cheremisinoff et al.[38]

A multitude of copolymer sub-types also exist, which include gradient,[39] periodic,[40] bottlebrush,[41] and rod-coil,[42] each with its own unique range of applications. For the purposes of the research outlined in this thesis, linear di-block copolymers are examined. These contain two chemically distinct blocks A and B, which, under the correct thermodynamic conditions, can self-assemble into ordered nanostructures depending on the chemical differences between the two constituent blocks. The theory behind how such self-assembly can occur is examined in the next section.

1.3 Theory of Block Copolymer Self-Assembly

As briefly mentioned in **section 1.1**, the self-assembly of BCPs arises from their capacity to microphase separate according to chemical differences between the two blocks of the diblock copolymer. Segregation is primarily driven by repulsion between the immiscible blocks, resulting in patterned structures. Thermodynamically, this occurs due to an unfavourable mixing enthalpy, combined with a small entropy of mixing.[43] The covalent bond that links the two components prevents macroscopic phase separation, and therefore precipitates microphase separation into domains with macromolecular dimensions. The type of morphology generated by these domains is a function of the composition of the BCP; in the case of di-BCPs, this can include cylinders, spheres, gyroids, lamellae, among others – each uniquely applicable to different systems and processes.

The morphology of a self-assembled BCP film can be tailored by varying a number of chemical parameters - most importantly: the degree of polymerisation N, the volume fraction f, and the Flory-Huggins parameter χ.[44] N is defined as the number of monomer units present in a polymer; in the case of di-BCPs, where two distinctive monomers are present, it can be expressed in terms of N_A and N_B, where $N = N_A + N_B$. The domain period L_0 of self-assembled BCP films is known to scale with value of N as $L_0 \sim N^{\delta}$, where δ is a parameter that typically has a value between 0.5–1.[45] The possibility of varying the N components of di-BCPs is one reason why they are especially suited to designing nanoscale patterns, as this enables the facile manipulation of feature sizes. f is defined as the number of monomers of one component A, divided by the total amount of monomers in the polymer: $f = \frac{N_A}{N}$. For di-BCPs, these are expressed as f_A and f_B where $f_A + f_B = 1$. The Flory-Huggins parameter χ is a unitless parameter that characterises the energetic interaction between dissimilar blocks in a copolymer mixture or polymer blend, with a higher value of χ corresponding to a greater degree of thermodynamic incompatibility. χ is inversely proportional to temperature, and as its value increases so does the tendency of a polymer mixture to separate. The various parameters outlined above can be combined into one thermodynamic expression of the free energy of the polymer system:[46]

$$\frac{\Delta G_{mix}}{k_B T} = \frac{1}{N_A}\ln(f_A) + \frac{1}{N_B}\ln(f_B) + f_A f_B \chi \qquad (1)$$

where ΔG_{mix} is the Gibbs free energy, k_B is the Boltzmann constant, and T is temperature. This is known as the Flory-Huggins equation, which describes how these various chemical parameters can influence the free energy (and thereby the phase behaviour) of a polymer mixture. The first two terms in **eq. 1** are related to the entropy of configuration of the polymer system, and can be manipulated through varying the chain length and relative volume fractions of the constituent chains A and B. The third term, containing χ, accounts for the entropic and enthalpic cost of the covalent bond between A and B monomers, and is a function of both the polymer chemistry, temperature, and N. An expression for χ as a function of *T* is shown below:

$$\chi(T) = \chi_S + \frac{\chi_H}{T} \tag{2}$$

where χ_S is the temperature-independent entropic term, and $\frac{\chi_H}{T}$ is the temperature-dependent enthalpic term. The values of χ_S and χ_H are typically determined via experimental studies and are subject to the specific block chemistry.[47-49] In the case of chemically dissimilar components, as is the case with the majority of BCP systems, the enthalpic term will dominate, allowing experimental control of χ through temperature.[50] Note that when N is sufficiently large (as is typically the case for BCP systems used in experimental studies) its influence on χ can be ignored and is hence not included in the above expression.[49]

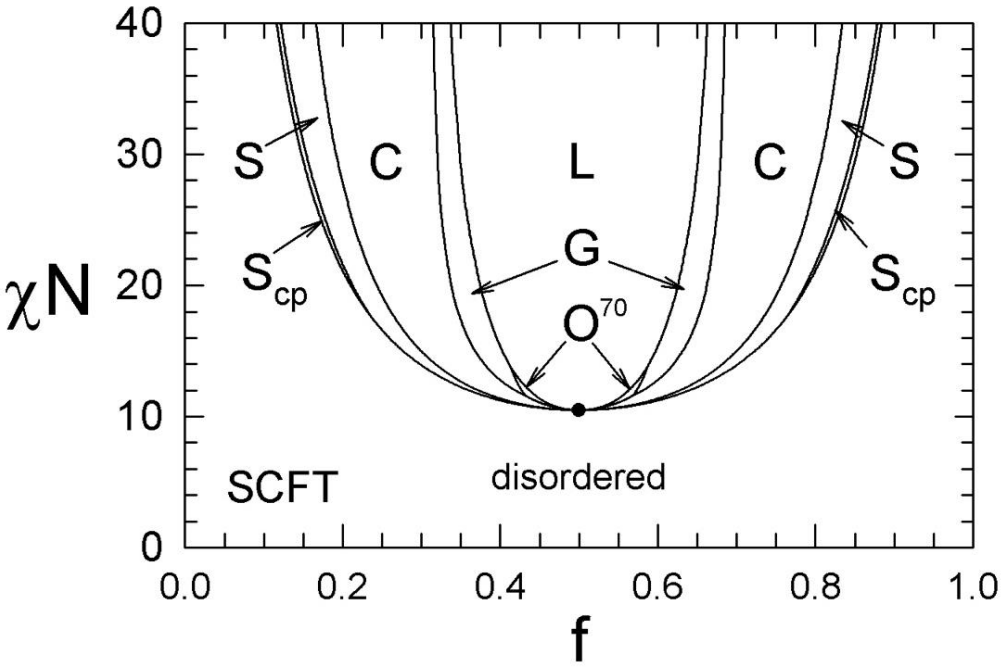

Figure 1.3. Phase diagram of an AB di-BCP melt as calculated from self–consistent field theory (SCFT). Phase stability regions are shown for ordered lamellar (L), cylindrical (C), bcc spherical (S), and gyroid (G), hcp spherical (S_{cp}) and *Fddd* (O^{70}) morphologies. Adapted from Matsen et al.[51]

According to Leibler's mean-field theory,[9] there are only two important quantities in determining phase equilibria in a block copolymer melt: the volume fraction f and the product χN. The relationship between χN and f is commonly depicted in a phase diagram, which outlines the range of possible morphologies that can be generated through the interplay of these parameters. Phase diagrams can be constructed either from experimental data or via simulations (most often via Monte Carlo and self–consistent field theory (SCFT)). A recent phase diagram by Matsen is shown in figure **1.3**, which has been generated via SCFT. Note however that the number and types of morphologies documented has changed significantly over the course of research in this field, with many historical variations of this diagram published.[51-53]

The phase diagram displayed in **figure 1.3** shows that above a certain minimum value of χN, when f (in this case the volume fraction of one component block A or B) possesses small values, the resulting morphology will consist of spheres in a body-centred cubic lattice, with an encompassing region of *B*. As f increases, cylindrical nanodomains are formed, followed by a bicontinuous (or gyroid) structure, and finally lamellae. The minimum value of χN arises from the point at which the block copolymer transitions from a locally segregated state to a homogenous state that is devoid of any long-range ordering. This is known as an order-disorder transition (ODT), which in the case of the χN value is written as χN_{ODT}. In the phase diagram calculated using SCFT as shown in **figure 1.3**, the value of χN_{ODT} at $f = 0.5$ is approximately 10.5.[54] In the case of lower molecular weight BCP systems (where N is reduced), it is desirable to use polymer systems with high values of χ in order to maintain block segregation. Hence, such high-χ BCP materials are of great interest for the generation of ever-smaller (< 20 nm) BCP pitch dimensions.[55] It is important to note that the variation of a number of key parameters can result in deviations from this SCFT χN_{ODT} value – these include block asymmetry ($f \neq 0.5$), ultrathin films, and the relative selectivity of film interfaces, the latter two of which are discussed in the next section.[56, 57]

1.3.1 Film thickness and interfacial effects

When the thickness t of a BCP film is within or below the polymer domain spacing L_0, confinement effects will significantly influence the surface behaviour and morphology. In quantitative terms, the degree of confinement can be estimated by the difference between the ratio of t/L_0 and commensurability.[58] There are two types of confinement that are commonly referred to in literature – hard confinement, where the polymer film is confined between two rigid interfaces, and soft confinement, where one interface is instead exposed to atmosphere. For the purposes of the experimental approaches undertaken in this thesis, soft confinement will be discussed in detail. The result of soft confinement in BCP films depends on the interaction between the substrate surface and the BCP film. The incommensurability between the polymer film thickness and the domain spacing causes compression and/or stretching of the polymer chains, which in the case of a preferential substrate is relieved via the generation of islands or holes.[46] In the case of a non-preferential or neutral surface, this will instead result in a nanostructure reorientation. Only when the film thickness matches a specific 'natural' thickness value h will a smooth film be obtained – in the case where both interfaces attract the same block, $h = nL_0$ where n is an integer, and for interfaces with preferential selectivity, $h = (n + 0.5)L_0$. Hence, in ultrathin BCP films, slight variations in films thickness can substantially influence the resulting pattern formation and film topography.[59] The thickness of BCP films can be tuned using the chosen deposition strategy – these include spin-coating,[10] dip-coating,[60] or spray-coating.[61] The resulting film thickness can be tailored by varying parameters such as the spin speed, solution concentration, or substrate temperature. Alternative deposition techniques have also been developed such as electrospray deposition, which aim to address the high wastage of polymer material during the spin or dip-coating.[62]

In order to maintain precise control over the self-assembly of BCP thin films, the interfacial selectivity of BCP films may be manipulated in a number of ways. Perhaps the most simplistic strategy is to vary the underlying substrate on which the film resides. Alternatively, brush layers may be deposited prior to the placement of the BCP film, which may be selective, neutral, or non-selective to a particular block chemistry.[63] In terms of the polymer-air interface, the presence of a solvent atmosphere can be used to influence the surface morphology as described in the next section.

1.4 Experimental Strategies for Self-Assembly

While the manipulation of N is relatively straightforward (via longer or shorter polymer chains), altering χ is somewhat more complex and can be achieved using a multitude of experimental approaches. The most commonly utilised of these strategies are thermal and solvent vapour annealing (SVA),[11] which are discussed below in detail.

1.4.1 Thermal Annealing

Thermal annealing is a straightforward and ubiquitously employed approach to eliminate defects and promote the ordering of the BCP films. This strategy is made possible due to the temperature dependency of χ (see **eq. 2**), which allows for a reduction of χ with increasing temperature.[64] As a BCP film is heated above the glass transition temperature T_g, the polymer chains acquire increased mobility, thus facilitating microphase-separation. There are plenty of examples of thermal annealing in the literature, in particular for PS-*b*-PMMA systems, where temperatures of between 160—250 °C are generally used to facilitate self-assembly.[65] Nonetheless, there are significant limitations to a purely thermal approach, as many BCP systems possess χN values of such magnitude that the minimum temperature required to induce self-assembly exceeds the degradation temperature of the polymer material itself. This issue can arise in two separate scenarios – firstly, in the case of high molecular weight BCPs where N is large,[11, 12] and secondly, in the case that the inherent χ value of one of the blocks (vs. the other block) is exceedingly high (such as P4VP or PEO-based BCP systems).[66]

1.4.2 Solvent Vapour Annealing

SVA is an experimentally proven alternative to thermal annealing, in particular for cases where the aforementioned limitations to a thermal approach must be overcome.[18, 30, 67] Briefly, a BCP film is firstly placed in a controlled atmosphere containing selective or neutral solvent vapours for a predetermined time period. The solvent vapours are uptaken into the BCP film, causing the film to swell. Once the desired exposure time has been reached, the film is removed from the solvent atmosphere; this allows for the evaporation of the solvent within the film, thereby returning the film to its original pre-SVA thickness.

The mechanism of microphase separation during SVA is described by a number of mathematical (or thermodynamic) expressions.[11] Firstly, chain mobility is greatly enhanced via a reduction in the T_g of the blocks as the BCP film swells with solvent.

Secondly, the addition of non-selective good solvents causes a screening effect between the immiscible blocks of the polymer system, hence reducing χ.[68] This screening effect can be quantitatively represented by an effective interaction parameter χ_{eff}, which is given by:

$$\chi_{eff} = \chi\phi_s^{\alpha} \tag{3}$$

where ϕ is the solvent concentration in the BCP film and α is a scaling exponent with a value of between ~1 and ~2 (depending on the polymer system).[69, 70] The amount of solvent absorbed into the BCP film (and hence ϕ_s) depends on the solvent vapour pressure, which thereby influences the resulting film morphology and ordering.[71, 72] A more comprehensive explanation of the relationship between χ_{eff} and ϕ_s is given in **chapter 2**. Finally, the addition of solvent results in a modification of the surface energies of the film (BCP-substrate and BCP-atmosphere interfaces).[73] Depending on the relative selectivity of the solvent(s) for the BCP film and substrate, this can cause preferential wetting of one block to one or both interfaces, consequently altering the morphological behaviour of the film.[74, 75] As mentioned before, polymer brush layers may also be used in conjunction with SVA to precisely tailor the interfacial energies of the BCP films, in particular when the underlying substrate exhibits poor selectivity for the particular type of BCP in use.[76-78]

Although a range of custom SVA setups exist, the majority can be categorised into two primary types that both indirectly rely on the manipulation of the solvent vapour pressure.[71] The first strategy involves the use of a solvent reservoir that is placed inside a closed vessel containing the BCP sample (see **figure 1.4** below).

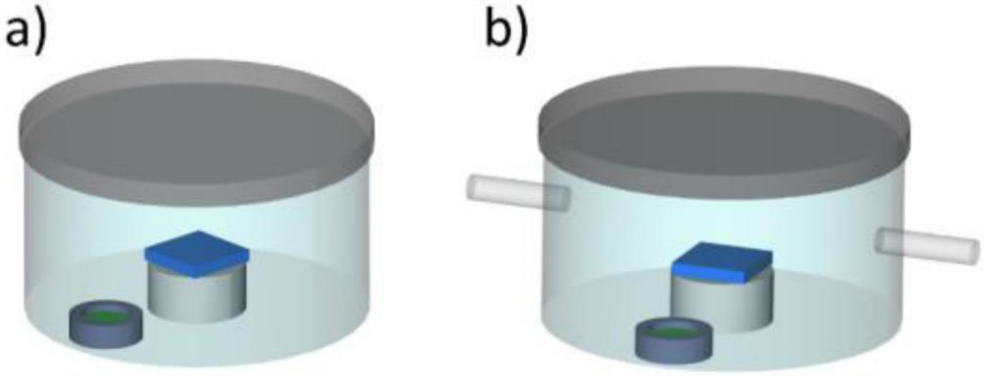

Figure 1.4. Examples of 'static' SVA setups. (a) shows the most simplistic setup, with a solvent vessel contained within the sample chamber. (b) shows a slightly more complex setup with inlet and outlet lines for an inert carrier gas. Adapted from Nelson et al.[13]

In the solvent reservoir strategy, the vapour pressure of the solvent within the vessel can be influenced by a number of variables including the temperature, solvent exposure time, surface area of the solvent reservoir, position of the sample within the vessel, among others. This strategy, often referred to as 'static' SVA, is advantageous in terms of its experimental simplicity, however its scalability, precision, and repeatability are severely limited due to the lack of precise temporal control over the solvent vapour pressures.[18] Furthermore, any minor humidity or temperature fluctuations in the lab environment can negatively affect the reproducibility.[79] More sophisticated static SVA setups may have some type of *in-situ* monitoring of the BCP film thickness (e.g. reflectometry or ellipsometry), however lack the means to fully direct the swelling kinetics over the entire course of the SVA process.[80, 81]

The second strategy, which will be referred to as 'precision' SVA (pSVA), involves maintaining precise, *in-situ* control over the vapour pressure of the sample chamber over the entire course of annealing. Rather than situating the exposed solvent reservoir within the sample chamber, the solvent is instead placed in an external vessel where an inert gas is bubbled through. The vapour is then controllably directed into the sample chamber (via flow, temperature control), where the swelling kinetics of the BCP film are monitored using techniques such as reflectometry,[12, 79] GISAXS,[82-84] AFM,[85] or ellipsometry.[86] An example of such a setup is shown below in **figure 1.5**.

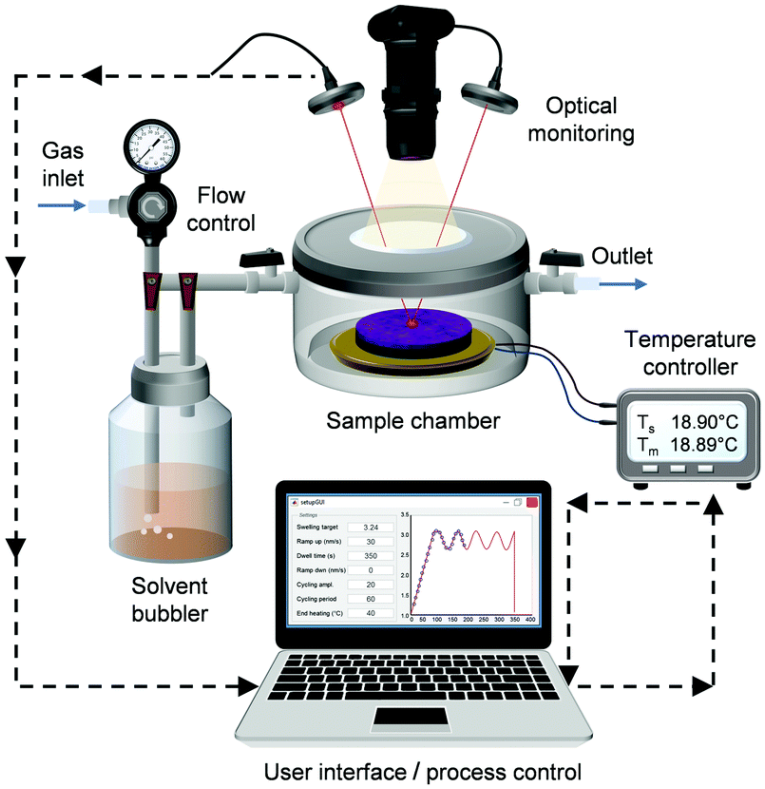

Figure 1.5. Example of a pSVA setup. Precise temperature control over the solvent and the stage temperature via PID controllers enables regulated variation of solvent uptake (and by extension film thickness), which is monitored using a reflectometer. Adapted from Hulkkonen et al.[12]

The vapour pressure – and thus the kinetic parameters such as film swelling, swelling/de-swelling rates and dwell time - are manipulated via minute changes in the solvent gas flow,[87] the temperature of the BCP film and/or solvent gas,[18] or a combination of these. Aside from the expected improvements in experimental reliability, such meticulous control over the self-assembly process has facilitated significant advances in the understanding of the morphological evolution and kinetics of the BCP films.[13, 17, 79, 88] The reader is referred to **chapter 2** for further details on BCP swelling kinetics.

1.5 Inorganic Nanostructures via Block Copolymer Templates

The ability of BCPs to act as spatially modifiable host templates for metal ion infiltration has facilitated a vast diversification of potential applications as of late. The potential mechanisms and strategies of metal infiltration are equally as varied, with the applicability of each method depending on variables such as the block chemistry, the type of precursor, the desired oxidation state of the resulting metal structures, and the

dimensionality of the polymer template. In comparison to alternative nanostructure deposition strategies such as sol-gel synthesis or vapour-liquid-solid growth, BCP templates enable a more simplistic, low cost, and low temperature route to develop 1, 2 and 3-dimensional inorganic nanostructures over a range of surface materials.[34, 89] For example, in the case of optical applications where flexible or curved substrates may be necessary, the spin-on deposition process of BCP films provides a low energy method of facilitating large-area nanostructure coverage.

The techniques most commonly used for selectively incorporating metal species into BCP domains can be divided into two main categories – vapour phase infiltration (VPI) and liquid phase infiltration (LPI). These are described below in order to provide background information for the results described in **chapters 3 and 4**.

1.5.1 Vapour Phase Infiltration

The two most common strategies for the vapour phase infiltration of inorganic precursors into the BCP films are atomic layer deposition (ALD) and sequential infiltration synthesis (SIS). ALD is a widely adopted technique for controllably depositing thin layers of inorganic materials. Thin films of atomic-scale precision are produced by sequential exposure to gaseous species facilitated by their self-limiting reaction with the substrate. Early work using ALD on BCP templates by *Peng* et al. involved the infiltration of PS-*b*-PMMA systems with precursors such as trimethylaluminium (TMA) or titanium tetrachloride to make patterned nanowire surfaces.[90] Freestanding TiO_2 structures have also successfully been created by *Ku* et al. via etching of the central PMMA domain of a cylindrical BCP film followed by ALD.[91]

SIS is a similar vapour phase technique that originally evolved from the adoption of ALD to BCP materials. In comparison to alternative techniques, SIS is considered a strong candidate for the integration of BCP-based patterning into industrial manufacturing due to the already widespread use of ALD methods. SIS was initially developed as a consequence of preliminary attempts to apply ALD techniques to polymer films, with the earliest SIS research focussing on the infiltration of TMA into various polymer species.[92] The nucleation of the inorganic material within a polymer template is facilitated by cyclical exposure to a gaseous metal precursor, which is typically selective to one domain of the BCP (process outlined in **figure 1.6**). In comparison to ALD, however, the

exposure cycles in SIS processes are generally longer in order to facilitate the infiltration of a 3D polymer volume.[93] Upon successful infiltration, the polymer matrix can be removed using techniques such as calcining, oxygen plasma, or UV-ozone, resulting in templated metal or metal oxide structures.[89] As the technique has evolved and advanced, the range of possible precursors has substantially expanded, with many identical to those used in conventional ALD processes.[93, 94]

Earlier SIS studies focused primarily on the utilisation of PS-*b*-PMMA BCP systems, owing to the extensive prior use of PMMA for directed self-assembly. For example, *Peng* et al. patterned nanoscopic structures via SIS-mediated Si, W and Zn precursor infiltration into cylindrical PS-*b*-PMMA domains.[95] *Kamsev* et al. further demonstrated the ability to adapt SIS to specifically target non-PMMA blocks via photooxidation of PS nanodomains, enabling the generation of Al_2O_3, TiO_2 and ZnO structures along with their corresponding inverse patterns.[96] Aside from PMMA systems, more recent publications have applied SIS to include many habitually studied block chemistries such as polyvinyl pyridine (PVP),[70] polylactic acid (PLA),[97] among others.[93] Furthermore, recent studies have demonstrated the high degree of controllability of the SIS process – for example, *Ishchenko* et al. analysed the influence of water pulses during the exposure step, demonstrating significantly enhanced growth of TiO_2 nanoparticle arrays in the presence of water.[98]

The development and optimization of SIS for BCP systems has resulted in the utilisation of SIS-templated structures across a host of applications. *She* et al. demonstrated the synthesis of large area, catalytically active heterostructures composed of Al_2O_3 and PdO via the SIS of a PS-*b*-P4VP BCP system.[99] Nanoporous ultrafiltration membranes were created by *Zhou* et al. via SIS of a PMMA majority PS-*b*-PMMA BCP system with an aluminium precursor.[100] The uniform and dense inorganic structures facilitated by SIS have also enabled the development of a number of electronic applications. For example, *Subramanian* et al. created a 3D, multi-layered electroactive ZnO nanomesh via the SIS stacked layers of a PS-*b*-P2VP BCP system, demonstrating a correlation between the electrical conductance and the number of stacked ZnO layers.[101] The SIS technique was also utilised by *Wang* et al. to fabricate polymer-inorganic hybrid materials via ZnO infiltration into polyaniline (PANI). The conductivity of these PANI/ZnO hybrid films exhibited a strong dependency on the number of exposure cycles, further demonstrating

the tuneability of SIS-templated nanomaterials.[102] Many studies have also utilised SIS to fabricate surface nanostructures capable of acting as etch masks for lithographic applications. *Doerk* et al. used a PS-*b*-PMMA system to as a template for fabrication Al_2O_3 nanowires atop a Si substrate, which upon etching yielded sub-10 nm grating nanostructures.[103] Similarly, *Dallarto* et al. utilised SIS infiltration of a PS-*b*-PMMA system to generate a Al_2O_3 hard mask, which was used to generate 15nm carbon lines via pattern transfer.[104] In addition to semiconductor lithographic applications, other studies have utilised SIS-based pattern transfer for areas such as antireflective coatings. *Rahman* et al. fabricated a nanotextured Si surface with broadband antireflectivity by using Al_2O_3 nanodot arrays as a hard mask for nanopillar etching (again using a PS-*b*-PMMA system with an aluminium precursor).[105]

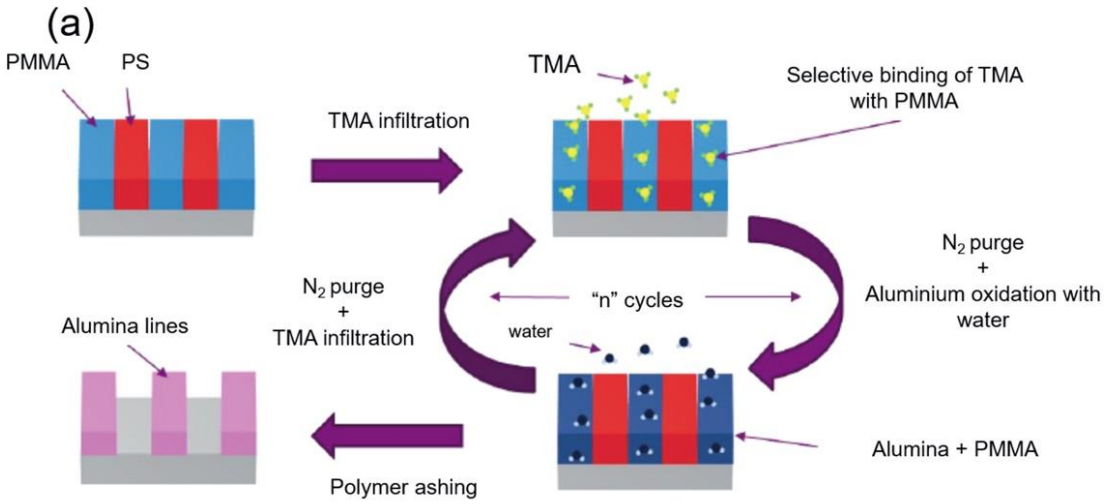

Figure 1.6. (a) Example process flow for SIS of trimethyl aluminium (TMA) into a PS-*b*-PMMA template. Adapted from Singh et al.[106]

1.5.2 Liquid Phase Infiltration

One notable drawback of vapour phase processes is the need for high vapour pressures to facilitate the infiltration process. The attainment of these pressures often requires high temperatures that exceed the glass transition temperature of the polymer material itself.[107] In contrast, LPI is a more facile strategy that involves the coordination of metal ions to a reactive block site via immersion or spin-coating of a liquid-phase metal ion solution. Aside from the more elementary processing environment, other advantages of LPI include the low cost, avoidance of volatile precursors, and high degree of scalability. Additionally, LPI is not limited by the diffusion depth of the vapour phase SIS precursor,

which severely restricts the maximum potential thickness of SIS-fabricated nanostructures.

There are two primary factors that influence the effectiveness of LPI - firstly, the diffusivity of the precursor species into the polymer domains, and secondly, the binding interaction between the precursor and the reactive sites within the polymer.[108] The relative importance of these factors depends strongly on the chemical nature of both the polymer domains and the desired precursor species. Commonly utilised reactive blocks for LPI include poly(vinyl-pyridine) (PVP) or poly(ethylene oxide) (PEO), both of which contain coordinative groups that can bind to the precursor species. Additionally, in order for LPI to be effective, the reactive block must swell in the solvent containing the dissolved metal precursor to facilitate effective diffusion. Common solvents used for LPI include water, ethanol and propanol, owing to the ease of dissolving common precursor materials.[108-111] By extension, the unreactive block must be inert to the solvent (PS, for example). In the case where strongly binding sites are not present in a BCP system, the equilibrium between the solvent and film will dominate the inclusion process.

The range of inorganic precursors that have been utilised for LPI is extensive - these include nitrate and chloride salts, along with cyanate and acetylacetonate coordination complexes.[107]. *Morris* et al. developed a facile inclusion strategy that involves spin-coating ethanolic solutions of precursors onto PS-*b*-PVP or PS-*b*-PEO templates, yielding CuO, Fe_xO_y, Al_2O_3, CeO_2, HfO_2, and NiO nanostructures among others.[112-114] It was found that the degree of precursor uptake could be partially controlled by varying the concentration of the precursor solution, demonstrating that while the coordination site within the reactive domains is important, diffusion kinetics also play a crucial role in LPI processes.[111] An alternative LPI technique that was first demonstrated by *Buriak* et al. (commonly referred to as aqueous metal reduction (AMR)) is to immerse the BCP films in an acidic solvent medium containing metal anions (derived from dissolved Au, Pt, Pd salts).[115] This technique has proven highly successful for developing metallic nanostructures via infiltration of PxVP-based BCP systems, owing to the coordinative bonding ability of the nitrogen in the pyridine group (see **chapter 3** for further details). Diffusion effects have also been found to influence the immersion strategy, with higher temperatures leading to faster diffusion kinetics and greater precursor uptake.[89]

Following the insertion of the metal precursor, the polymer film is removed via a number of possible techniques; these include oxidative process such as O_2 plasma[116] or UV-ozone,[117] or reductive process such as Ar/H_2 plasma.[118] A templated metal/metal oxide structure is obtained as a result, with the chemical state of the resulting material determined by the choice of polymer removal technique (see **figure 1.7** below).

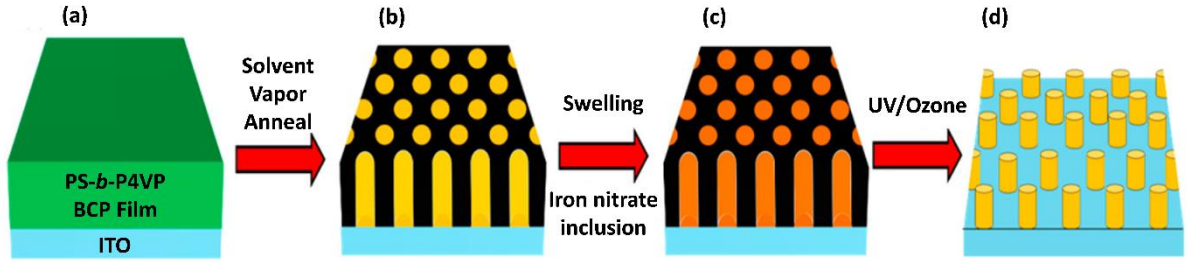

Figure 1.7. Schematic of an LPI strategy for fabricating iron oxide (Fe_2O_3) nanodots using a PS-*b*-P4VP BCP template. Adapted from *Bas* et al.[119]

Oxidative etching techniques typically give rise to/generate/yield a metal oxide structure, whereas reductive techniques produce metallic templates.[118] LPI also allows for the synthesis of bimetallic nanostructures via the dissolution of multiple metal precursors in the same solution. The composition of the resulting metal structures can be tuned by varying the stoichiometric ratio of the precursors in solution prior to the infiltration.[120] The loading of the precursor into the BCP domains can be marginally tuned by varying the concentration of the precursor in solution.[99]

Similarly to SIS, the dimensionality of the LPI-templated metal/metal oxide structures is not solely limited to surface features. One such strategy to fabricate multilayer metal structures is to place a second BCP layer atop the first layer of metallised features, which is then infiltrated following the same LPI procedure as before. This strategy also allows for the synthesis of multicomponent patterns where the second layer is infiltrated with a different metal species to the first.[121] Alternatively, a second BCP layer may be placed immediately atop the infiltrated first layer, which are then metallised in a single step.[108] Recent work has even demonstrated how a combination of LPI and SIS may be selectively used in multi-layered BCP films to produce core-satellite nanoclusters of varying metal species.[122] The length of time that the BCP film is exposed to the metal precursor solution is also known to influence the topographical height of the resulting

metal structures, with increased time allowing for an augmented uptake of coordinated metal ions into the active nanodomain.[123]

In terms of applications, LPI-templated metal/metal oxide structures are equally as diverse as their VPI counterparts, again owing to their low fabrication cost and high degree of scalability. *Cummins* et al. utilised the metal salt inclusion strategy to fabricate ~10 nm aligned nanofin architectures on silicon and germanium substrates.[110, 124] This was achieved via LPI of a cylindrical PS-*b*-P4VP BCP system with Fe or Al salts, which were then converted to oxide nanostructures via UV-ozone treatment and used as masks to etch into the underlying substrate. Owing to their long-range order, facile fabrication method and sub-16 nm dimensions, such structures have potential applications in nanocircuitry and lithographic patterning. A similar strategy was also utilised by *Mokarian* et al. for fabricating antireflective silicon and glass surfaces, whereby an UHMW PS-*b*-P2VP system was infiltrated with a nickel precursor via LPI. Following UV-ozone treatment, the resulting NiO nanodot array was used as an etch mask to create high aspect ratio nanopillars with antireflective properties.[23] Other successful areas of application include catalysis,[123] sensing,[21, 119] and nanoelectronics.[108]

1.6 Thesis Overview

The primary goals of the work contained in this thesis focuses are firstly, to address the challenge of producing large-period structures in a rapid and reliable process, and secondly, to develop novel nanodevices and applied materials via metal incorporation of BCP films. The BCP systems of choice for the work outlined herein are PS-*b*-P2VP and PS-b-P4VP of varying molecular weights.

In Chapter 2, the self-assembly of an UHMW BCP system is extensively studied and optimised using a custom-built SVA chamber. We demonstrate that such a system can be induced to phase-separate on timescales as short as 10 minutes by rapidly and controllably swelling the film to very high levels of solvent concentration (ϕ_s). Andrew Selkirk conceived and coordinated the study, along with performing the SVA experiments and characterisation via AFM, SEM and statistical orientational analysis. Nadezda Prochukhan and Andrew Selkirk performed the etching, while GISAXS was performed by Rachel Kilbride and Andrew Parnell.

In Chapter 3, the effect of the BCP film thickness on the resulting metal feature heights for photocatalytic applications is examined. Andrew Selkirk conceived the experiments and performed the sample preparation, characterisation via AFM, SEM, and reflectometry. Andrew Selkirk and Riley Gatensby conducted XPS characterisation. Sajjad Hossein Mir and Brian Jennings conducted the photocatalytic experiments.

In Chapter 4, a nanostructured tungsten oxide (WO_3) catalytic device capable of water splitting and adrenaline sensing is fabricated using block copolymer templating. This involves the deposition and self-assembly of a PS-*b*-P4VP BCP film atop an indium tin oxide (ITO) substrate, followed by tungsten precursor infiltration and polymer removal. Andrew Selkirk and Aislan Paiva performed the sample preparation and characterisation via AFM, SEM and reflectometry. Salih Zeki Bas coordinated and performed the sensing experiments. Ainur Zhussupbekova performed XPS characterisation. Nadezda Prochukhan performed Raman experiments.

Chapter 5 details an overall summary of the results shown herein and provides a perspective on the future direction of the field.

1.7 References

1. Liddle, J. A.; Gallatin, G. M., Nanomanufacturing: A Perspective. *ACS Nano* **2016,** *10* (3), 2995-3014.
2. Glotzer, S. C.; Solomon, M. J.; Kotov, N. A., Self-assembly: From nanoscale to microscale colloids. *AIChE Journal* **2004,** *50* (12), 2978-2985.
3. Solomon, M. J., Directions for targeted self-assembly of anisotropic colloids from statistical thermodynamics. *Current Opinion in Colloid & Interface Science* **2011,** *16* (2), 158-167.
4. Li, H.; Carter, J. D.; LaBean, T. H., Nanofabrication by DNA self-assembly. *Materials Today* **2009,** *12* (5), 24-32.
5. Black, C. T.; Ruiz, R.; Breyta, G.; Cheng, J. Y.; Colburn, M. E.; Guarini, K. W.; Kim, H.; Zhang, Y., Polymer self assembly in semiconductor microelectronics. *IBM Journal of Research and Development* **2007,** *51* (5), 605-633.
6. Cummins, C.; Lundy, R.; Walsh, J. J.; Ponsinet, V.; Fleury, G.; Morris, M. A., Enabling future nanomanufacturing through block copolymer self-assembly: A review. *Nano Today* **2020,** *35*, 100936.
7. Hamley, I. W., *The Physics of Block Copolymers*. Oxford University Press: 1998.
8. Hamley, I. W., Ordering in thin films of block copolymers: Fundamentals to potential applications. *Progress in Polymer Science* **2009,** *34* (11), 1161-1210.
9. Leibler, L., Theory of Microphase Separation in Block Copolymers. *Macromolecules* **1980,** *13* (6), 1602-1617.
10. Leniart, A. A.; Pula, P.; Tsai, E. H. R.; Majewski, P. W., Large-Grained Cylindrical Block Copolymer Morphologies by One-Step Room-Temperature Casting. *Macromolecules* **2020,** *53* (24), 11178-11189.
11. Yu, X.; Han, Y., 3 - Thermal and solvent annealing of block copolymer films. In *Directed Self-assembly of Block Co-polymers for Nano-manufacturing*, Gronheid, R.; Nealey, P., Eds. Woodhead Publishing: 2015; pp 47-66.
12. Hulkkonen, H.; Salminen, T.; Niemi, T., Automated solvent vapor annealing with nanometer scale control of film swelling for block copolymer thin films. *Soft Matter* **2019,** *15* (39), 7909-7917.
13. Nelson, G.; Drapes, C. S.; Grant, M. A.; Gnabasik, R.; Wong, J.; Baruth, A., High-Precision Solvent Vapor Annealing for Block Copolymer Thin Films. *Micromachines* **2018,** *9* (6).
14. Leniart, A. A.; Pula, P.; Sitkiewicz, A.; Majewski, P. W., Macroscopic Alignment of Block Copolymers on Silicon Substrates by Laser Annealing. *ACS Nano* **2020,** *14* (4), 4805-4815.
15. Pester, C. W.; Schmidt, K.; Ruppel, M.; Schoberth, H. G.; Böker, A., Electric-Field-Induced Order–Order Transition from Hexagonally Perforated Lamellae to Lamellae. *Macromolecules* **2015,** *48* (17), 6206-6213.
16. Jeon, H. U.; Jin, H. M.; Kim, J. Y.; Cha, S. K.; Mun, J. H.; Lee, K. E.; Oh, J. J.; Yun, T.; Kim, J. S.; Kim, S. O., Electric field directed self-assembly of block copolymers for rapid formation of large-area complex nanopatterns. *Molecular Systems Design & Engineering* **2017,** *2* (5), 560-566.
17. Cheng, X.; Böker, A.; Tsarkova, L., Temperature-Controlled Solvent Vapor Annealing of Thin Block Copolymer Films. *Polymers* **2019,** *11* (8), 1312.
18. Lundy, R.; Flynn, S. P.; Cummins, C.; Kelleher, S. M.; Collins, M. N.; Dalton, E.; Daniels, S.; Morris, M. A.; Enright, R., Controlled solvent vapor annealing

of a high χ block copolymer thin film. *Physical Chemistry Chemical Physics* **2017,** *19* (4), 2805-2815.
19. Tang, C.; Lennon, E. M.; Fredrickson, G. H.; Kramer, E. J.; Hawker, C. J., Evolution of Block Copolymer Lithography to Highly Ordered Square Arrays. *Science* **2008,** *322* (5900), 429-432.
20. Warren, S. C.; Messina, L. C.; Slaughter, L. S.; Kamperman, M.; Zhou, Q.; Gruner, S. M.; DiSalvo, F. J.; Wiesner, U., Ordered Mesoporous Materials from Metal Nanoparticle–Block Copolymer Self-Assembly. *Science* **2008,** *320* (5884), 1748-1752.
21. Bas, S. Z.; Cummins, C.; Selkirk, A.; Borah, D.; Ozmen, M.; Morris, M. A., A Novel Electrochemical Sensor Based on Metal Ion Infiltrated Block Copolymer Thin Films for Sensitive and Selective Determination of Dopamine. *ACS Applied Nano Materials* **2019,** *2* (11), 7311-7318.
22. Harandizadeh, Z.; Ito, T., Block Copolymer-Derived Recessed Nanodisk-Array Electrodes as Platforms for Folding-Based Electrochemical DNA Sensors. *ChemElectroChem* **2019,** *6* (22), 5627-5632.
23. Mokarian-Tabari, P.; Senthamaraikannan, R.; Glynn, C.; Collins, T. W.; Cummins, C.; Nugent, D.; O'Dwyer, C.; Morris, M. A., Large Block Copolymer Self-Assembly for Fabrication of Subwavelength Nanostructures for Applications in Optics. *Nano Lett* **2017,** *17* (5), 2973-2978.
24. Stefik, M.; Guldin, S.; Vignolini, S.; Wiesner, U.; Steiner, U., Block copolymer self-assembly for nanophotonics. *Chemical Society Reviews* **2015,** *44* (15), 5076-5091.
25. Li, X.; Xue, L.; Han, Y., Broadband antireflection of block copolymer/homopolymer blend films with gradient refractive index structures. *Journal of Materials Chemistry* **2011,** *21* (15), 5817-5826.
26. Song, D.-P.; Jacucci, G.; Dundar, F.; Naik, A.; Fei, H.-F.; Vignolini, S.; Watkins, J. J., Photonic Resins: Designing Optical Appearance via Block Copolymer Self-Assembly. *Macromolecules* **2018,** *51* (6), 2395-2400.
27. Noro, A.; Tomita, Y.; Shinohara, Y.; Sageshima, Y.; Walish, J. J.; Matsushita, Y.; Thomas, E. L., Photonic Block Copolymer Films Swollen with an Ionic Liquid. *Macromolecules* **2014,** *47* (12), 4103-4109.
28. Chan, E. P.; Walish, J. J.; Urbas, A. M.; Thomas, E. L., Mechanochromic Photonic Gels. *Advanced Materials* **2013,** *25* (29), 3934-3947.
29. Kang, Y.; Walish, J. J.; Gorishnyy, T.; Thomas, E. L., Broad-wavelength-range chemically tunable block-copolymer photonic gels. *Nature Materials* **2007,** *6* (12), 957-960.
30. Selkirk, A.; Prochukhan, N.; Lundy, R.; Cummins, C.; Gatensby, R.; Kilbride, R.; Parnell, A.; Baez Vasquez, J.; Morris, M.; Mokarian-Tabari, P., Optimization and Control of Large Block Copolymer Self-Assembly via Precision Solvent Vapor Annealing. *Macromolecules* **2021**.
31. Li, W.; Müller, M., Defects in the Self-Assembly of Block Copolymers and Their Relevance for Directed Self-Assembly. *Annual Review of Chemical and Biomolecular Engineering* **2015,** *6* (1), 187-216.
32. IEEE. International Roadmap for Devices and Systems 2017 Emerging Research Materials 2017. https://irds.ieee.org/editions/2017.
33. Cummins, C.; Pino, G.; Mantione, D.; Fleury, G., Engineering block copolymer materials for patterning ultra-low dimensions. *Molecular Systems Design & Engineering* **2020,** *5* (10), 1642-1657.
34. Cummins, C.; Ghoshal, T.; Holmes, J. D.; Morris, M. A., Strategies for Inorganic Incorporation using Neat Block Copolymer Thin Films for Etch Mask

Function and Nanotechnological Application. *Advanced Materials* **2016,** *28* (27), 5586-5618.
35. Chen, Q. P.; Barreda, L.; Oquendo, L. E.; Hillmyer, M. A.; Lodge, T. P.; Siepmann, J. I., Computational Design of High-χ Block Oligomers for Accessing 1 nm Domains. *ACS Nano* **2018,** *12* (5), 4351-4361.
36. Carmean, R. N.; Becker, T. E.; Sims, M. B.; Sumerlin, B. S., Ultra-High Molecular Weights via Aqueous Reversible-Deactivation Radical Polymerization. *Chem* **2017,** *2* (1), 93-101.
37. Callister, W. D., *Fundamentals of materials science and engineering*. Wiley London: 2000; Vol. 471660817.
38. Cheremisinoff, N. P., *Condensed Encyclopedia of Polymer Engineering Terms*. Butterworth-Heinemann: Boston, 2001; p 39-81.
39. Alam, M. M.; Jack, K. S.; Hill, D. J. T.; Whittaker, A. K.; Peng, H., Gradient copolymers – Preparation, properties and practice. *European Polymer Journal* **2019,** *116*, 394-414.
40. Yokota, K.; Kougo, T.; Hirabayashi, T., Syntheses and Properties of Periodic Copolymers. *Polymer Journal* **1983,** *15* (5), 349-354.
41. Verduzco, R.; Li, X.; Pesek, S. L.; Stein, G. E., Structure, function, self-assembly, and applications of bottlebrush copolymers. *Chemical Society Reviews* **2015,** *44* (8), 2405-2420.
42. Xu, F.; Zhang, J.; Zhang, P.; Luan, X.; Mai, Y., "Rod–coil" copolymers get self-assembled in solution. *Materials Chemistry Frontiers* **2019,** *3* (11), 2283-2307.
43. Mai, Y.; Eisenberg, A., Self-assembly of block copolymers. *Chem Soc Rev* **2012,** *41* (18), 5969-85.
44. Lennon, E. M.; Katsov, K.; Fredrickson, G. H., Free Energy Evaluation in Field-Theoretic Polymer Simulations. *Physical Review Letters* **2008,** *101* (13), 138302.
45. Kim, S.; Nealey, P. F.; Bates, F. S., Directed Assembly of Lamellae Forming Block Copolymer Thin Films near the Order–Disorder Transition. *Nano Letters* **2014,** *14* (1), 148-152.
46. Segalman, R. A., Patterning with block copolymer thin films. *Materials Science and Engineering: R: Reports* **2005,** *48* (6), 191-226.
47. Dudowicz, J.; Freed, K. F., Relation of effective interaction parameters for binary blends and diblock copolymers: lattice cluster theory predictions and comparisons with experiment. *Macromolecules* **1993,** *26* (1), 213-220.
48. Clarke, C. J.; Eisenberg, A.; La Scala, J.; Rafailovich, M. H.; Sokolov, J.; Li, Z.; Qu, S.; Nguyen, D.; Schwarz, S. A.; Strzhemechny, Y.; Sauer, B. B., Measurements of the Flory−Huggins Interaction Parameter for Polystyrene−Poly(4-vinylpyridine) Blends. *Macromolecules* **1997,** *30* (14), 4184-4188.
49. Zha, W.; Han, C. D.; Lee, D. H.; Han, S. H.; Kim, J. K.; Kang, J. H.; Park, C., Origin of the Difference in Order−Disorder Transition Temperature between Polystyrene-block-poly(2-vinylpyridine) and Polystyrene-block-poly(4-vinylpyridine) Copolymers. *Macromolecules* **2007,** *40* (6), 2109-2119.
50. Kozuch, D. J.; Zhang, W.; Milner, S. T., Predicting the Flory-Huggins χ Parameter for Polymers with Stiffness Mismatch from Molecular Dynamics Simulations. *Polymers* **2016,** *8* (6).
51. Matsen, M. W., Effect of Architecture on the Phase Behavior of AB-Type Block Copolymer Melts. *Macromolecules* **2012,** *45* (4), 2161-2165.
52. Bates, F. S.; Schulz, M. F.; Khandpur, A. K.; Förster, S.; Rosedale, J. H.; Almdal, K.; Mortensen, K., Fluctuations, conformational asymmetry and block copolymer phase behaviour. *Faraday Discussions* **1994,** *98* (0), 7-18.

53. Matsen, M. W.; Schick, M., Stable and unstable phases of a diblock copolymer melt. *Physical Review Letters* **1994,** *72* (16), 2660-2663.
54. Matsen, M. W.; Bates, F. S., Origins of Complex Self-Assembly in Block Copolymers. *Macromolecules* **1996,** *29* (23), 7641-7644.
55. Sinturel, C.; Bates, F. S.; Hillmyer, M. A., High χ–Low N Block Polymers: How Far Can We Go? *ACS Macro Letters* **2015,** *4* (9), 1044-1050.
56. Ahn, H.; Lee, Y.; Lee, H.; Kim, Y.; Ryu, D. Y.; Lee, B., Substrate interaction effects on order to disorder transition behavior in block copolymer films. *Journal of Polymer Science Part B: Polymer Physics* **2013,** *51* (7), 567-573.
57. Kim, Y.; Yong, D.; Lee, W.; Ahn, H.; Kim, J. H.; Kim, J. U.; Ryu, D. Y., Order-to-Disorder Transition of Lamella-Forming PS-b-P2VP Films Confined between the Preferential Surface and Neutral Substrate. *Macromolecules* **2019,** *52* (22), 8672-8681.
58. Albert, J. N. L.; Epps, T. H., Self-assembly of block copolymer thin films. *Materials Today* **2010,** *13* (6), 24-33.
59. Knoll, A.; Horvat, A.; Lyakhova, K. S.; Krausch, G.; Sevink, G. J. A.; Zvelindovsky, A. V.; Magerle, R., Phase Behavior in Thin Films of Cylinder-Forming Block Copolymers. *Physical Review Letters* **2002,** *89* (3), 035501.
60. Vapaavuori, J.; Grosrenaud, J.; Siiskonen, A.; Priimagi, A.; Pellerin, C.; Bazuin, C. G., Photocontrol of Supramolecular Azo-Containing Block Copolymer Thin Films during Dip-Coating: Toward Nanoscale Patterned Coatings. *ACS Applied Nano Materials* **2019,** *2* (6), 3526-3537.
61. Bucher, T.; Clodt, J. I.; Abetz, C.; Bajer, B.; Filiz, V., Spraying of Ultrathin Isoporous Block Copolymer Membranes—A Story about Challenges and Limitations. *Membranes* **2020,** *10* (12), 404.
62. Hu, H.; Rangou, S.; Kim, M.; Gopalan, P.; Filiz, V.; Avgeropoulos, A.; Osuji, C. O., Continuous Equilibrated Growth of Ordered Block Copolymer Thin Films by Electrospray Deposition. *ACS Nano* **2013,** *7* (4), 2960-2970.
63. In, I.; La, Y.-H.; Park, S.-M.; Nealey, P. F.; Gopalan, P., Side-Chain-Grafted Random Copolymer Brushes as Neutral Surfaces for Controlling the Orientation of Block Copolymer Microdomains in Thin Films. *Langmuir* **2006,** *22* (18), 7855-7860.
64. Sinturel, C.; Vayer, M.; Morris, M.; Hillmyer, M. A., Solvent Vapor Annealing of Block Polymer Thin Films. *Macromolecules* **2013,** *46* (14), 5399-5415.
65. Hashimoto, T.; Bodycomb, J.; Funaki, Y.; Kimishima, K., The Effect of Temperature Gradient on the Microdomain Orientation of Diblock Copolymers Undergoing an Order−Disorder Transition. *Macromolecules* **1999,** *32* (3), 952-954.
66. Russell, T. P.; Hjelm, R. P.; Seeger, P. A., Temperature dependence of the interaction parameter of polystyrene and poly(methyl methacrylate). *Macromolecules* **1990,** *23* (3), 890-893.
67. Kim, S. H.; Misner, M. J.; Xu, T.; Kimura, M.; Russell, T. P., Highly Oriented and Ordered Arrays from Block Copolymers via Solvent Evaporation. *Advanced Materials* **2004,** *16* (3), 226-231.
68. Jung, Y. S.; Ross, C. A., Solvent-Vapor-Induced Tunability of Self-Assembled Block Copolymer Patterns. *Advanced Materials* **2009,** *21* (24), 2540-2545.
69. Doerk, G. S.; Li, R.; Fukuto, M.; Yager, K. G., Wet Brush Homopolymers as "Smart Solvents" for Rapid, Large Period Block Copolymer Thin Film Self-Assembly. *Macromolecules* **2020,** *53* (3), 1098-1113.
70. Xiong, S.; Wan, L.; Ishida, Y.; Chapuis, Y.-A.; Craig, G. S. W.; Ruiz, R.; Nealey, P. F., Directed Self-Assembly of Triblock Copolymer on Chemical Patterns for

Sub-10-nm Nanofabrication via Solvent Annealing. *ACS Nano* **2016,** *10* (8), 7855-7865.
71. Gu, X. Self-assembly of block copolymers by solvent vapor annealing, mechanism and lithographic applications. Doctoral Thesis, University of Massachusetts Amherst, 2014.
72. Gu, X.; Gunkel, I.; Hexemer, A.; Russell, T. P., Controlling Domain Spacing and Grain Size in Cylindrical Block Copolymer Thin Films by Means of Thermal and Solvent Vapor Annealing. *Macromolecules* **2016,** *49* (9), 3373-3381.
73. Brassat, K.; Lindner, J. K. N., Nanoscale Block Copolymer Self-Assembly and Microscale Polymer Film Dewetting: Progress in Understanding the Role of Interfacial Energies in the Formation of Hierarchical Nanostructures. *Advanced Materials Interfaces* **2020,** *7* (5), 1901565.
74. Huang, E.; Rockford, L.; Russell, T. P.; Hawker, C. J., Nanodomain control in copolymer thin films. *Nature* **1998,** *395* (6704), 757-758.
75. Park, S.; Kim, Y.; Lee, W.; Hur, S.-M.; Ryu, D. Y., Gyroid Structures in Solvent Annealed PS-b-PMMA Films: Controlled Orientation by Substrate Interactions. *Macromolecules* **2017,** *50* (13), 5033-5041.
76. Wang, H. S.; Kim, K. H.; Bang, J., Thermal Approaches to Perpendicular Block Copolymer Microdomains in Thin Films: A Review and Appraisal. *Macromolecular Rapid Communications* **2019,** *40* (4), 1800728.
77. Evangelio, L.; Fernández-Regúlez, M.; Fraxedas, J.; Müller, M.; Pérez-Murano, F., Role of Penetrability into a Brush-Coated Surface in Directed Self-Assembly of Block Copolymers. *ACS Applied Materials & Interfaces* **2019,** *11* (3), 3571-3581.
78. Pandav, G.; Durand, W. J.; Ellison, C. J.; Willson, C. G.; Ganesan, V., Directed self assembly of block copolymers using chemical patterns with sidewall guiding lines, backfilled with random copolymer brushes. *Soft Matter* **2015,** *11* (47), 9107-9114.
79. Jin, C.; Olsen, B. C.; Luber, E. J.; Buriak, J. M., Nanopatterning via Solvent Vapor Annealing of Block Copolymer Thin Films. *Chemistry of Materials* **2017,** *29* (1), 176-188.
80. Sinturel, C.; Grosso, D.; Boudot, M.; Amenitsch, H.; Hillmyer, M. A.; Pineau, A.; Vayer, M., Structural Transitions in Asymmetric Poly(styrene)-block-Poly(lactide) Thin Films Induced by Solvent Vapor Exposure. *ACS Applied Materials & Interfaces* **2014,** *6* (15), 12146-12152.
81. Bai, W.; Hannon, A. F.; Gotrik, K. W.; Choi, H. K.; Aissou, K.; Liontos, G.; Ntetsikas, K.; Alexander-Katz, A.; Avgeropoulos, A.; Ross, C. A., Thin Film Morphologies of Bulk-Gyroid Polystyrene-block-polydimethylsiloxane under Solvent Vapor Annealing. *Macromolecules* **2014,** *47* (17), 6000-6008.
82. Zhang, J.; Posselt, D.; Sepe, A.; Shen, X.; Perlich, J.; Smilgies, D.-M.; Papadakis, C. M., Structural Evolution of Perpendicular Lamellae in Diblock Copolymer Thin Films during Solvent Vapor Treatment Investigated by Grazing-Incidence Small-Angle X-Ray Scattering. *Macromolecular Rapid Communications* **2013,** *34* (16), 1289-1295.
83. Zhang, J.; Posselt, D.; Smilgies, D.-M.; Perlich, J.; Kyriakos, K.; Jaksch, S.; Papadakis, C. M., Lamellar Diblock Copolymer Thin Films during Solvent Vapor Annealing Studied by GISAXS: Different Behavior of Parallel and Perpendicular Lamellae. *Macromolecules* **2014,** *47* (16), 5711-5718.

84. Gu, X.; Gunkel, I.; Hexemer, A.; Gu, W.; Russell, T. P., An In Situ Grazing Incidence X-Ray Scattering Study of Block Copolymer Thin Films During Solvent Vapor Annealing. *Advanced Materials* **2014,** *26* (2), 273-281.
85. Takano, K.; Nyu, T.; Maekawa, T.; Seki, T.; Nakatani, R.; Komamura, T.; Hayakawa, T.; Hayashi, T., Real-time and in situ observation of structural evolution of giant block copolymer thin film under solvent vapor annealing by atomic force microscopy. *RSC Advances* **2020,** *10* (1), 70-75.
86. Bilchak, C. R.; Govind, S.; Contreas, G.; Rasin, B.; Maguire, S. M.; Composto, R. J.; Fakhraai, Z., Kinetic Monitoring of Block Copolymer Self-Assembly Using In Situ Spectroscopic Ellipsometry. *ACS Macro Letters* **2020,** *9* (8), 1095-1101.
87. Gotrik, K. W.; Hannon, A. F.; Son, J. G.; Keller, B.; Alexander-Katz, A.; Ross, C. A., Morphology Control in Block Copolymer Films Using Mixed Solvent Vapors. *ACS Nano* **2012,** *6* (9), 8052-8059.
88. Baruth, A.; Seo, M.; Lin, C. H.; Walster, K.; Shankar, A.; Hillmyer, M. A.; Leighton, C., Optimization of Long-Range Order in Solvent Vapor Annealed Poly(styrene)-block-poly(lactide) Thin Films for Nanolithography. *ACS Applied Materials & Interfaces* **2014,** *6* (16), 13770-13781.
89. Cummins, C.; Morris, M. A., Using block copolymers as infiltration sites for development of future nanoelectronic devices: Achievements, barriers, and opportunities. *Microelectronic Engineering* **2018,** *195*, 74-85.
90. Peng, Q.; Tseng, Y.-C.; Darling, S. B.; Elam, J. W., Nanoscopic Patterned Materials with Tunable Dimensions via Atomic Layer Deposition on Block Copolymers. *Advanced Materials* **2010,** *22* (45), 5129-5133.
91. Giraud, E. C.; Mokarian-Tabari, P.; Toolan, D. T. W.; Arnold, T.; Smith, A. J.; Howse, J. R.; Topham, P. D.; Morris, M. A., Highly Ordered Titanium Dioxide Nanostructures via a Simple One-Step Vapor-Inclusion Method in Block Copolymer Films. *ACS Applied Nano Materials* **2018,** *1* (7), 3426-3434.
92. Wilson, C. A.; Grubbs, R. K.; George, S. M., Nucleation and Growth during Al2O3 Atomic Layer Deposition on Polymers. *Chemistry of Materials* **2005,** *17* (23), 5625-5634.
93. Waldman, R. Z.; Mandia, D. J.; Yanguas-Gil, A.; Martinson, A. B. F.; Elam, J. W.; Darling, S. B., The chemical physics of sequential infiltration synthesis—A thermodynamic and kinetic perspective. *The Journal of Chemical Physics* **2019,** *151* (19), 190901.
94. Subramanian, A.; Tiwale, N.; Nam, C.-Y., Review of Recent Advances in Applications of Vapor-Phase Material Infiltration Based on Atomic Layer Deposition. *JOM* **2019,** *71* (1), 185-196.
95. Peng, Q.; Tseng, Y.-C.; Darling, S. B.; Elam, J. W., A Route to Nanoscopic Materials via Sequential Infiltration Synthesis on Block Copolymer Templates. *ACS Nano* **2011,** *5* (6), 4600-4606.
96. Kamcev, J.; Germack, D. S.; Nykypanchuk, D.; Grubbs, R. B.; Nam, C.-Y.; Black, C. T., Chemically Enhancing Block Copolymers for Block-Selective Synthesis of Self-Assembled Metal Oxide Nanostructures. *ACS Nano* **2013,** *7* (1), 339-346.
97. Evangelio Araujo, L.; Fernández-Regúlez, M.; Chevalier, X.; Nicolet, C.; Cayrefourcq, I.; Navarro, C.; Fleury, G.; Pérez-Murano, F., *Use of sequential infiltration synthesis to improve the pattern transfer of PS-b-PLA DSA (Conference Presentation)*. SPIE: 2017; Vol. 10146.
98. Ishchenko, O. M.; Krishnamoorthy, S.; Valle, N.; Guillot, J.; Turek, P.; Fechete, I.; Lenoble, D., Investigating Sequential Vapor Infiltration Synthesis on Block-

Copolymer-Templated Titania Nanoarrays. *The Journal of Physical Chemistry C* **2016,** *120* (13), 7067-7076.
99. She, Y.; Goodman, E. D.; Lee, J.; Diroll, B. T.; Cargnello, M.; Shevchenko, E. V.; Berman, D., Block-Co-polymer-Assisted Synthesis of All Inorganic Highly Porous Heterostructures with Highly Accessible Thermally Stable Functional Centers. *ACS Applied Materials & Interfaces* **2019,** *11* (33), 30154-30162.
100. Zhou, C.; Segal-Peretz, T.; Oruc, M. E.; Suh, H. S.; Wu, G.; Nealey, P. F., Fabrication of Nanoporous Alumina Ultrafiltration Membrane with Tunable Pore Size Using Block Copolymer Templates. *Advanced Functional Materials* **2017,** *27* (34), 1701756.
101. Subramanian, A.; Doerk, G.; Kisslinger, K.; Yi, D. H.; Grubbs, R. B.; Nam, C.-Y., Three-dimensional electroactive ZnO nanomesh directly derived from hierarchically self-assembled block copolymer thin films. *Nanoscale* **2019,** *11* (19), 9533-9546.
102. Wang, W.; Chen, C.; Tollan, C.; Yang, F.; Beltrán, M.; Qin, Y.; Knez, M., Conductive Polymer–Inorganic Hybrid Materials through Synergistic Mutual Doping of the Constituents. *ACS Applied Materials & Interfaces* **2017,** *9* (33), 27964-27971.
103. Doerk, G. S.; Gao, H.; Wan, L.; Lille, J.; Patel, K. C.; Chapuis, Y.-A.; Ruiz, R.; Albrecht, T. R., Transfer of self-aligned spacer patterns for single-digit nanofabrication. *Nanotechnology* **2015,** *26* (8), 085304.
104. Dallorto, S.; Staaks, D.; Schwartzberg, A.; Yang, X.; Lee, K. Y.; Rangelow, I. W.; Cabrini, S.; Olynick, D. L., Atomic layer deposition for spacer defined double patterning of sub-10 nm titanium dioxide features. *Nanotechnology* **2018,** *29* (40), 405302.
105. Rahman, A.; Ashraf, A.; Xin, H.; Tong, X.; Sutter, P.; Eisaman, M. D.; Black, C. T., Sub-50-nm self-assembled nanotextures for enhanced broadband antireflection in silicon solar cells. *Nature Communications* **2015,** *6* (1), 5963.
106. Singh, A.; Knaepen, W.; Sayan, S.; el Otell, Z.; Chan, B. T.; Maes, J.; Gronheid, R., *Impact of sequential infiltration synthesis on pattern fidelity of DSA lines*. SPIE: 2015; Vol. 9425.
107. Berman, D.; Shevchenko, E., Design of functional composite and all-inorganic nanostructured materials via infiltration of polymer templates with inorganic precursors. *Journal of Materials Chemistry C* **2020,** *8* (31), 10604-10627.
108. Subramanian, A.; Tiwale, N.; Doerk, G.; Kisslinger, K.; Nam, C.-Y., Enhanced Hybridization and Nanopatterning via Heated Liquid-Phase Infiltration into Self-Assembled Block Copolymer Thin Films. *ACS Applied Materials & Interfaces* **2020,** *12* (1), 1444-1453.
109. Cummins, C.; Bell, A. P.; Morris, M. A., Creating Active Device Materials for Nanoelectronics Using Block Copolymer Lithography. *Nanomaterials (Basel)* **2017,** *7* (10), 304.
110. Cummins, C.; Gangnaik, A.; Kelly, R. A.; Borah, D.; O'Connell, J.; Petkov, N.; Georgiev, Y. M.; Holmes, J. D.; Morris, M. A., Aligned silicon nanofins via the directed self-assembly of PS-b-P4VP block copolymer and metal oxide enhanced pattern transfer. *Nanoscale* **2015,** *7* (15), 6712-6721.
111. Ghoshal, T.; Holmes, J. D.; Morris, M. A., Development of Ordered, Porous (Sub-25 nm Dimensions) Surface Membrane Structures Using a Block Copolymer Approach. *Scientific Reports* **2018,** *8* (1), 7252.
112. Cummins, C.; Borah, D.; Rasappa, S.; Chaudhari, A.; Ghoshal, T.; O'Driscoll, B. M. D.; Carolan, P.; Petkov, N.; Holmes, J. D.; Morris, M. A., Self-assembly of polystyrene-block-poly(4-vinylpyridine) block copolymer on molecularly

functionalized silicon substrates: fabrication of inorganic nanostructured etchmask for lithographic use. *Journal of Materials Chemistry C* **2013,** *1* (47), 7941-7951.
113. Ghoshal, T.; Shaw, M. T.; Bolger, C. T.; Holmes, J. D.; Morris, M. A., A general method for controlled nanopatterning of oxide dots: a microphase separated block copolymer platform. *Journal of Materials Chemistry* **2012,** *22* (24), 12083-12089.
114. Ghoshal, T.; Maity, T.; Godsell, J. F.; Roy, S.; Morris, M. A., Large Scale Monodisperse Hexagonal Arrays of Superparamagnetic Iron Oxides Nanodots: A Facile Block Copolymer Inclusion Method. *Advanced Materials* **2012,** *24* (18), 2390-2397.
115. Chai, J.; Wang, D.; Fan, X.; Buriak, J. M., Assembly of aligned linear metallic patterns on silicon. *Nature Nanotechnology* **2007,** *2* (8), 500-506.
116. Lee, W.; Lee, S.; Tang, A. S.; Kim, C.; Liu, R.; Im, K.; Jung, H.-T.; Ross, C. A., Platinum Infiltration of a Block Copolymer for Interconnected Three-Dimensional Metal Nanostructures. *ACS Applied Nano Materials* **2021,** *4* (1), 793-801.
117. Ghoshal, T.; O'Connell, J.; Sinturel, C.; Andreazza, P.; Holmes, J. D.; Morris, M. A., Solvent mediated inclusion of metal oxide into block copolymer nanopatterns: Mechanism of oxide formation under UV-Ozone treatment. *Polymer* **2019,** *173*, 197-204.
118. Aizawa, M.; Buriak, J. M., Block Copolymer Templated Chemistry for the Formation of Metallic Nanoparticle Arrays on Semiconductor Surfaces. *Chemistry of Materials* **2007,** *19* (21), 5090-5101.
119. Bas, S. Z.; Cummins, C.; Borah, D.; Ozmen, M.; Morris, M. A., Electrochemical Sensing of Hydrogen Peroxide Using Block Copolymer Templated Iron Oxide Nanopatterns. *Analytical Chemistry* **2018,** *90* (2), 1122-1128.
120. Mikkelsen, K.; Cassidy, B.; Hofstetter, N.; Bergquist, L.; Taylor, A.; Rider, D. A., Block Copolymer Templated Synthesis of Core–Shell PtAu Bimetallic Nanocatalysts for the Methanol Oxidation Reaction. *Chemistry of Materials* **2014,** *26* (24), 6928-6940.
121. Shin, D. O.; Mun, J. H.; Hwang, G.-T.; Yoon, J. M.; Kim, J. Y.; Yun, J. M.; Yang, Y.-B.; Oh, Y.; Lee, J. Y.; Shin, J.; Lee, K. J.; Park, S.; Kim, J. U.; Kim, S. O., Multicomponent Nanopatterns by Directed Block Copolymer Self-Assembly. *ACS Nano* **2013,** *7* (10), 8899-8907.
122. Alvarez-Fernandez, A.; Nallet, F.; Fontaine, P.; Cummins, C.; Hadziioannou, G.; Barois, P.; Fleury, G.; Ponsinet, V., Large area Al2O3–Au raspberry-like nanoclusters from iterative block-copolymer self-assembly. *RSC Advances* **2020,** *10* (67), 41088-41097.
123. Lee, J.; Mishra, A. K.; Choi, C.; Kim, D.; Kim, E. Y.; Yong, K.; Kim, J. K., Three-Dimensional Nanoporous Metal Structures from Poly(2-vinylpyridine)-block-Poly(4-vinylpyridine) Copolymer Thin Film. *ACS Applied Materials & Interfaces* **2020,** *12* (13), 15667-15674.
124. Cummins, C.; Gangnaik, A.; Kelly, R. A.; Hydes, A. J.; O'Connell, J.; Petkov, N.; Georgiev, Y. M.; Borah, D.; Holmes, J. D.; Morris, M. A., Parallel Arrays of Sub-10 nm Aligned Germanium Nanofins from an In Situ Metal Oxide Hardmask using Directed Self-Assembly of Block Copolymers. *Chemistry of Materials* **2015,** *27* (17), 6091-6096.

Chapter 2: Optimization and Control of Large Block Copolymer Self-Assembly via Precision Solvent Vapor Annealing

2.1. Abstract

The self-assembly of ultra-high molecular weight (UHMW) block copolymers (BCPs) remains a complex and time-consuming endeavor owing to the high kinetic penalties associated with long polymer chain entanglement. In this work, we report a unique strategy of overcoming these kinetic barriers through precision solvent annealing of an UHMW polystyrene-*block*-poly(2-vinylpyridine) BCP system (M_w: ~800 kg mol^{-1}) by fast swelling to very high levels of solvent concentration (ϕ_s). Phase separation on timescales of ~10 minutes is demonstrated once a thickness-dependent threshold ϕ_s value of ~0.80 – 0.86 is achieved, resulting in lamellar feature spacings of over 190 nm. The threshold ϕ_s value was found to be greater for films with higher dry-thickness (D_0) values. Tuneability of the domain morphology is achieved through controlled variation of both D_0 and ϕ_s, with the kinetically unstable hexagonal perforated lamellar (HPL) phase observed at ϕ_s values of ~0.67 and D_0 values of 59-110 nm. This HPL phase can be controllably induced into an order-order transition (OOT) to a lamellar morphology upon further increasing of ϕ_s to 0.80 or above. As confirmed by GISAXS, the lateral ordering of the lamellar domains is shown to improve with increasing ϕ_s up to a maximum value at which the films transition to a disordered state. Thicker films are shown to possess a higher maximum ϕ_s value before transitioning to a disordered state. The swelling rate is shown to moderately influence the lateral ordering of the phase-separated structures, while the amount of hold time at a particular value of ϕ_s does not notably enhance the phase-separation process. These large period self-assembled lamellar domains are then employed to facilitate pattern transfer using a liquid phase infiltration method followed by plasma etching, generating ordered, high aspect ratio Si nanowall structures with spacings of ~190 nm and heights of up to ~500 nm. This work underpins the feasibility of a room-temperature, solvent-based annealing approach for the reliable and scalable fabrication of sub-wavelength nanostructures via BCP lithography.

2.2. Introduction

The directed self-assembly of block copolymers (BCPs) is a well-studied technique for the controlled formation of a wide range of periodic thin-film morphologies, including spherical, cylindrical, gyroidal, and lamellar among others.[1] Structural modulation can be achieved through the manipulation of the molecular composition, while the periodicity of the domains can be adjusted through varying the molecular weight.[2, 3] From a technological standpoint, the high degree of versatility of BCP self-assembly, in addition to scalability and low process temperatures, has provided an attractive route for the cost-effective fabrication of surface nanostructures with an enormous variety of potential applications, including nanoelectronics,[4, 5] chemical sensors,[6-9] antireflective coatings,[10-13] and optically active surfaces.[14-16] In the case of optoelectronic applications such as interconnect patterning, the periodicity of the lateral domain features must generally exceed approximately 100 nm such that the structures are capable of interacting with wavelengths on the order of visible light.[17, 18] In order to facilitate the formation of such feature sizes, ultra-high molecular weight (UHMW) BCP systems in excess of 500 kg/mol are typically utilized. The self-assembly of UHMW BCP systems creates additional complexities in the annealing process, in particular the extremely slow ordering kinetics associated with increased chain entanglement.[19] The energy barrier required to induce chain mobility in highly entangled BCPs cannot always be overcome even at temperatures exceeding that of the glass transition temperature (Tg) of the BCP system, effectively eliminating the possibility of a purely thermal annealing approach in such UHMW systems.[20]

The majority of recent literature, including the work described here, instead employ solvent vapor annealing (SVA) as an alternative technique to facilitate the self-assembly of UHMW systems. SVA involves the uptake of solvent into a BCP film, resulting in increased polymer chain mobility, a lower effective value of Tg, and the avoidance of any thermal degradation of the material.[21-23] There are multiple interdependent variables that influence the SVA process, including pressure, temperature and humidity. Nonetheless, previous work has shown it can be performed with a very simple strategy known as ‘static’ SVA – this consists of a BCP sample placed inside a sealed chamber containing a reservoir of solvent, which is then left for a predetermined period of time.[24-27] Moreover, SVA can be performed at room temperatures or below, and has been proven

to effectively induce self-assembly in a number of UHMW BCP systems.[20, 28-31] Kim et al. successfully obtained phase-separation of lamellar and gyroid UHMW PS-b-PMMA BCP films with periods of ~200 nm using tetrahydrofuran (THF) as a neutral solvent for SVA, followed by a 12-hour thermal annealing step.[20, 29] Phase separation of an UHMW spherical PS-b-PMMA system was also demonstrated by Cao et al. again using THF as the annealing solvent of choice.[28] Additionally, Takano et al. developed a novel instrumentation technique to monitor the phase separation of UHMW lamellar PS-b-PMMA using in situ atomic force microscopy (AFM) under high swelling conditions during SVA.[30] Most recently, Cummins et al. achieved the phase separation of a high molecular weight PS-P2VP system ($M_n = 430\,kg/mol$) in a time of 1 hour using an uncontrolled 'static' SVA strategy.[32] Despite the relative success of these previous studies for the induction of phase-separation in UHMW systems, the required timescales often extended from several hours to days – thereby severely hindering the industrial applicability of such processes.[20, 28-30] The acceleration of the SVA process is therefore critical for the future development of this field. Here, we demonstrate a procedure for ultrafast self-assembly of UHMW block copolymer systems by controlling the swelling kinetics during SVA, reducing the required annealing time to minutes.

One notable improvement in expediting the SVA process for UHMW systems as of late was by Doerk et al., who utilized blends consisting of lamella-forming polystyrene-block-poly(methyl methacrylate) (PS-b-PMMA) ($M_n \leq 2000\,kg/mol$) combined with low molecular weight PS and PMMA homopolymer to accelerate the phase separation process.[31] This resulted in the formation of ordered lamellar domains with periodicity of up to 211 nm from a total annealing time of 1 hour (plus an additional 5 min thermal annealing step following SVA). Although this work demonstrated a major step towards accelerated SVA timeframes for UHMW BCPs, the influence of many of the kinetic components of the SVA technique – such as the swelling/de-swelling rate or swelling time – remain predominantly unexplored for such systems. Previous kinetics studies examining lower molecular weight BCPs have proven the critical importance of the aforementioned parameters in the enhancement of self-assembly timescales;[33-37] hence, it seemed desirable to determine the effects of such variables on an UHMW system.

In order to maintain precise control over BCP swelling kinetics during SVA, a variety of specialized annealing chambers have been constructed where the solvent uptake into the

BCP film can be regulated in situ during annealing.[33, 35, 38-42] The primary kinetic variable of focus for many of these setups is the swollen film thickness D_{sw}, which is dependent on the concentration of solvent inside the polymer film ϕ_s. D_{sw} is well-known to play a crucial role in the kinetics of self-assembly, with a positive observed correlation between a higher value of D_{sw} and increased lateral ordering.[35, 37, 43] Recently, Hulkkonen et al. utilized a custom-built annealing chamber to precisely control the swelling behavior of HMW PS-b-P2VP systems (($M_n = 258\,kg/mol$) via a temperature-controlled sample stage, resulting in the formation of hexagonal cylindrical domains in <15 minutes.[35] The BCP systems examined in their study, however, were not of sufficient molecular weight to fabricate domain sizes greater than 100 nm. To our knowledge, little published work exists on optimizing the self-assembly kinetics of UHMW BCP systems using controlled SVA techniques.

Accordingly, in this report we investigate the swelling kinetics of a commercially available UHMW lamellar PS-b-P2VP BCP system with a molecular weight of ~800 kg/mol (Mn: 440-353 kg/mol, $f_{PS} = 0.57$), in order to improve the reliability and speed of the microphase separation process. This particular BCP system was chosen as previous published work by our group demonstrated the potential self-assembly of this system upon exposure to both THF and chloroform using the conventional 'static' SVA method.[12] In the work shown herein, we demonstrate a greatly expedited timescale for the phase-separation of UHMW PS-b-P2VP films using a bespoke SVA chamber. We firstly examine the effects of the dry film thickness, D_0, and the solvent concentration in the polymer film, ϕ_s, on the structural evolution and lateral grain ordering of the rapidly swollen BCP films, resulting in the controlled formation of both equilibrium and non-equilibrium BCP phases. The formation of the previously demonstrated hexagonal perforated lamellar (HPL) phase along with well-ordered lamellar domains with periods of ~190 nm is achieved using total annealing times of ~10 minutes. The effect of the swelling time on the structural evolution, along with the influence of the swelling rate on the lateral grain sizes of the lamellar domains, is also examined. Finally, we also show the capability of the phase separated films to be utilized for pattern transfer, with the formation of high aspect ratio (up to 7.5) sub-wavelength Si nanostructures using a metal salt infiltration process followed by reactive ion etching. This is a critical asset for application areas.

2.3. Experimental Section:

2.3.1. Materials & Sample Preparation: Polystyrene-block-poly(2-vinylpyridine) (M_n: 440-b-353 kg/mol, PDI: 1.19) was purchased from Polymer Source Inc. and used without further purification. Anhydrous toluene, THF and ethanol were purchased from Sigma-Aldrich and used without further purification. Varying amounts of PS-*b*-P2VP were dissolved in a 4:1 (volume fraction) mixture of toluene and THF to make polymer solutions of between 0.5-3% (w/w), which were left stirring overnight to ensure complete dissolution. For SVA, chloroform and THF (both HPLC, 99.9%, Sigma-Aldrich) were used. 2×2 cm pieces of Si <100> wafers with a native oxide layer were cleaned by ultrasonication in acetone for 20 minutes, followed by drying under N_2 gas. BCP solutions were then spin-coated onto the clean Si substrates for 30 seconds at 4500 rpm.

2.3.2. Annealing Rig: The SVA rig utilized in this study is an upgraded version of the setup described by *Lundy* et al.[38] The stainless steel annealing chamber has an internal volume of 1.94 L, and possesses an access door with a quartz glass viewport located on the top of chamber (see **Figure 1**). The inlet and outlet valves for solvent/N_2 vapor flow are located on the left and right-hand side of the chamber respectively. To generate solvent vapor, nitrogen gas was passed through a flow meter and into a bubbler chamber containing the THF-chloroform mixture. In order to maintain a constant vapor pressure inside the SVA chamber over the entire annealing process, it was essential to mitigate any temperature decrease of the solvent mixture over time due to evaporative cooling. This was achieved by attaching a flexible heat pad to the solvent bubbler. The heat pad was connected to a PID controller, which maintained a constant solvent temperature of 21.0 $\pm$ 0.15°C using feedback from a resistance temperature detector (RTD) probe located inside the bubbler chamber as shown in **Figure 2.1**. The flow rate of the N_2 gas was held at ~400 sccm during annealing. The solvent chamber could be rapidly quenched to preserve the phase separated BCP morphology using an N_2 purge line. A copper stage is located inside the chamber upon which the samples were placed during annealing, allowing samples of up to 4'' to be processed. An RTD embedded inside the copper stage allowed the stage temperature to be measured and provided feedback for a PID controller to control the stage temperature ($\pm$ 0.15 °C). In order to monitor the film thickness *in-situ* during SVA, a Filmetrics F3-CS reflectometer with a UV-Vis light source (380-1050 nm) was mounted on top of the quartz viewport. To account for any variation in the light

source intensity, the reflectometer was calibrated using a Si reflectance standard prior to each sample run. The experimental reflectance data was measured over a wavelength range of 420-1050 nm and used a three-layer model consisting of the Si substrate, the PS-*b*-P2VP BCP layer, and air. Refractive index models for both the dry BCP films and the swollen films were estimated using the Lorenz-Lorentz rule of mixing, which utilized the refractive indices of the pure polymer and solvent components (PS, $n = 1.586$, P2VP: $n = 1.527$, THF: $n = 1.407$, chloroform: $n = 1.440$) to obtain a refractive index range of 1.558 (for the dry BCP film) to 1.457 as the concentration of the THF:chloroform solvent mixture increased up to a ϕ_s value of 0.87 (see **Section S2)**. The time interval used for each data point shown was 2 seconds, with an integration time of ~250 ms.

2.3.3. SVA process: The BCP samples were placed on the heated copper stage directly under the reflectometer beam, which was baselined prior to each sample measurement as per above. The initial stage temperature, which ranged between (15.9 °C and 20.9 °C) depending on the experiment, was set prior to initiating the annealing process. Once the temperature had stabilized, solvent vapor was introduced at a rate of 400 sccm during which the film thickness was recorded in real time by the reflectometer (see **section S2.7.2** for fitting details). Once the sample approached the desired swollen thickness, the temperature of the stage was gradually increased in increments of 0.1 °C using the PID controller to slow the swelling rate to zero. The film was then held at this swollen thickness value for the required annealing time. During the hold time, the stage temperature was periodically adjusted in increments of 0.1 °C to avoid any large fluctuations in the film thickness. As soon as the required hold time was reached, the temperature of the stage was instantaneously increased to 30 °C and the chamber was purged with nitrogen, which ensured a rapid deswelling regime (of approximately 5-10 seconds depending on the swollen thickness) and that all remaining solvent inside the film was purged.

2.3.4. Oxide nanostructure formation, pattern transfer: The formation of the metal oxide structure from the BCP template follows a similar process described in previous work. Samples were first immersed in ethanol for 20 minutes to facilitate surface reconstruction, and subsequently left to dry at room temperature. Iron (III) nitrate nonahydrate ($Fe_2(NO_3)_3.9H_2O$) was dissolved in ethanol at a concentration of 0.5 % w/w, and nickel (II) nitrate hexahydrate ($Ni(NO3)_2.6H_2O$) was dissolved in ethanol at a

concentration of 0.6% w/w. The salt solution was stirred for 1 hour to ensure complete dissolution and was then spin-coated onto the ethanol-reconstructed BCP samples at a speed of 3200 rpm for 30 seconds. A UV/O_3 treatment (PSD Pro Series Digital UV Ozone System; Novascan Technologies, Inc.) was then performed on the samples for 3 hours to completely remove the polymer template and oxidize the metal precursor. The patterns were etched into the substrate using an OIPT Plasma lab System100 ICP180 etch tool, utilizing a gas mixture of SF_6 (15 sccm) and CHF_3 (80 sccm), an ICP power of 1200 W and RIE power of 20 W, and a chamber pressure of 20 mTorr.

2.3.5. Sample characterization: Atomic force microscopy (AFM) was performed in non-contact mode (Park Systems, XE-7 under ambient conditions using silicon cantilevers (PPP-NCHR model) with a force constant of 42 N/m. SEM images were taken using a Carl Zeiss Ultra plus using an InLens detector with an accelerating voltage of 5 kV and a working distance of 4.5 mm. For cross-sectional SEM images, the substrate was cleaved into two and placed on a sample holder that was angled perpendicular to the electron beam. The stage was then tilted to 10-20°, depending on the image. Grazing Incidence Small Angle X-ray Scattering (GISAXS) was performed at the Soft Matter Analytical Laboratory (SMALL), Department of Chemistry, University of Sheffield using a Xeuss 2.0 (Xenocs) system with 9.243 keV X-rays from a liquid Ga MetalJet source (Excillum), with an incident beam angle of 0.16°. The sample to detector distance was 6.404m, flight tubes were held under vacuum to remove air scatter and the data was processed using Foxtrot Soleil and the GIXSGUI MATLAB Toolbox.[44]

2.3.6. Image analysis: Orientational mapping was performed on SEM images using the OrientationJ plugin for ImageJ. The correlation length, an indicator of orientational ordering in the pattern, was estimated using software described by Murphy *et al.*,[45] where the correlation function is obtained from a set of orientation angles that are calculated using a skeletonization process on the BCP domain structures of each image. 10×10 μm AFM images were used to determine the correlation length values shown in this report (example in **Figure S2.7.12**). To briefly describe the process, the contrast between the two BCP domains (in this case the PS and P2VP domains) is firstly enhanced though smoothening (to reduce random noise) and then converted into a binary image by thresholding (PS represented as black, P2VP white). The line features identified from the binary images are then skeletonized into single-pixel width, and the orientational angle

$\phi(r)$ of each pixel along the skeletonized line features is determined using a rolling average of the tangent along each line. The correlation function $C(r-r')$ can then be calculated from the set of orientation angles $\phi(r)$ for each point analyzed in the image as follows: $C(r-r') = \langle \cos[2\{\phi(r) - \phi(r')\}] \rangle$. The correlation length ξ is then related to the correlation function through an exponential fit: $C(r-r') = e^{-\frac{r}{\xi}}$. All error bars in this work represent two standard deviations (2σ) from the mean value unless stated otherwise.

2.4. Results and Discussion

A 793 kg/mol PS-b-P2VP (440 kg/mol PS, 353 kg/mol P2VP) system was utilized for this study. This system was of particular interest, as it was shown in previous work by our group to be capable of phase separation into a kinetically unstable HPL structure upon 'static' SVA in a THF and chloroform atmosphere for an hour, with feature spacing of ~180 nm.[12] This structure, with large area coverage and periodicity on the order of visible light wavelengths, proved to be highly applicable in the fabrication of antireflective nanostructures. One issue that was encountered, however, was the low reproducibility of the self-assembly method. It was found that slight fluctuations in the lab temperature, annealing solvent concentration, or even the position of the sample within the annealing chamber often led to widely different morphologies. Although the variation in results was expected due to the non-equilibrium nature of microphase separation UHMW BCPs, it was of interest from a technological point of view to examine and monitor the self-assembly kinetics in more detail in order to achieve greater repeatability.

UHMW BCP systems typically require high swelling ratios in order to initiate polymer mobility.[46] This is due to the influence of molecular weight on the level of chain entanglement – higher molecular weight systems possess longer polymer chains, and thereby a higher degree of entanglement in the dry BCP film. SVA is a well-known method that can be used to address this issue. With the addition of a relatively neutral solvent to the BCP film via SVA, the polymer-polymer interactions can be reduced as the solvent molecules produce a screening effect at the interface between the two blocks.[47] This screening effect can be quantitatively represented by an effective interaction parameter χ_{eff}:[48]

$$\chi_{eff} = \chi\phi_{BCP}^{\beta} \quad (1)$$

Where χ is the Flory-Huggins interaction parameter for the dry BCP film, ϕ_{BCP} is the polymer concentration of the swollen film, and β is an exponent factor with a value that varies between ~1 to ~2, and varies depending on the morphology of the ordered film, the selectivity of the solvent, and the solvent concentration inside the film.[49, 50] A higher swelling ratio (and consequently a lower value of ϕ_{BCP}) will therefore reduce the value of χ_{eff}, increasing chain mobility and allowing microphase separation to occur. ϕ_{BCP} is equal to (D_0/D_{sw}), the inverse of the swelling ratio, where D_0 is the initial film thickness, and D_{sw} is the swollen film thickness. This value can also be related to the solvent concentration inside the BCP film, ϕ_s, which is equal to $1 - \phi_{BCP}$.[39]

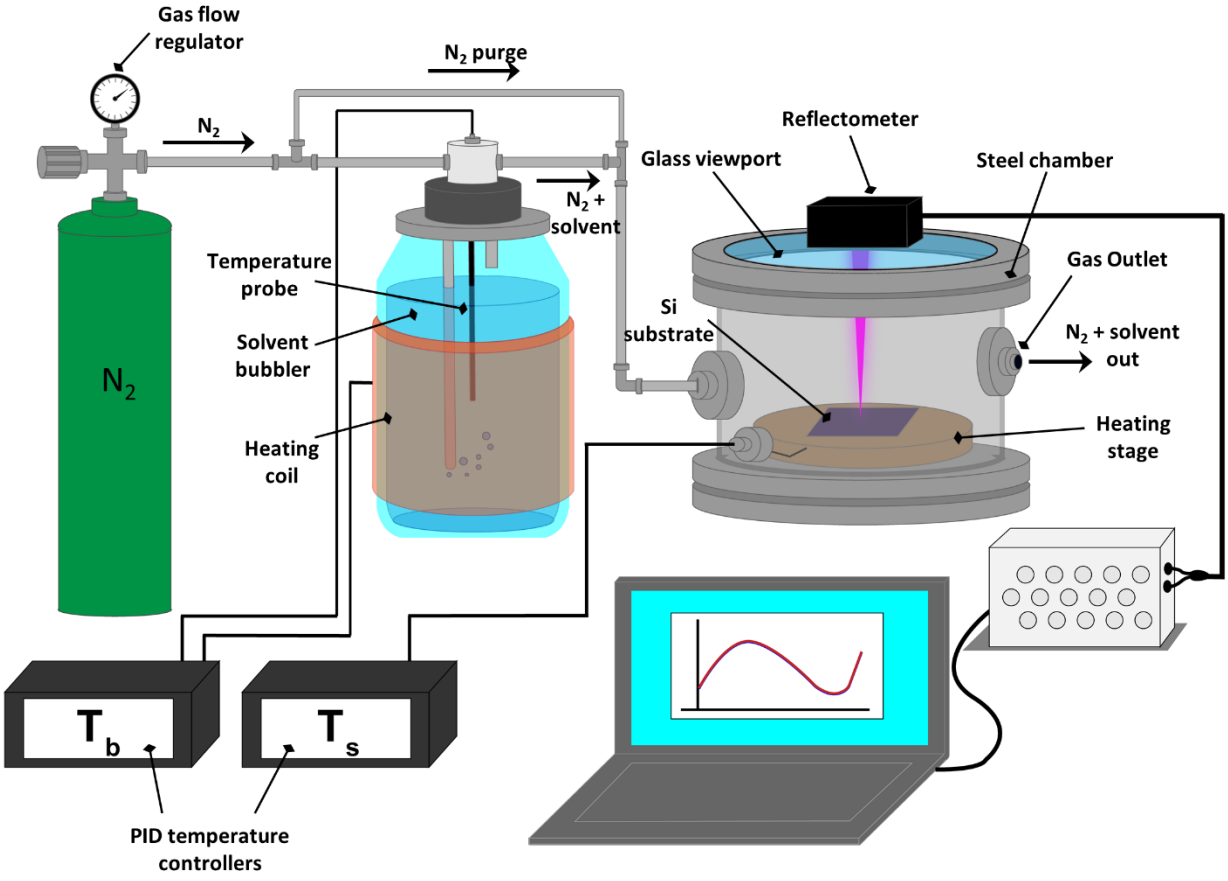

Figure 2.1. Diagram of the solvent vapor annealing setup for UHMW films. Films of PS-*b*-P2VP are spin-coated onto Si substrates, and then solvent vapor annealed inside the chamber while the film thickness is monitored *in situ* using a reflectometer.

Conventional SVA methods are often incapable of attaining the minimum swelling ratio required to initiate phase separation of UHMW systems regardless of the total annealing time, due to a lack of control over the relative saturation P/P_{sat} of the solvent vapor in the chamber (where P is the partial pressure of the annealing solvent vapor and P_{sat} is the saturated vapor pressure of the solvent at a fixed temperature).[35] Control over the relative saturation of a BCP film during SVA is crucial in order to attain high swelling ratios, as P/P_{sat} is directly related to ϕ_s through the following relationship:[51]

$$\ln\left(\frac{P}{P_{sat}}\right) = \chi(1-\phi_s)^2 + \ln(\phi_s) + (1-N^{-1})(1-\phi_s) \quad (2)$$

where N is the degree of polymerization. Consequently, in order to fully examine the swelling kinetics of the UHMW BCP system, we utilized a customized SVA rig system where P/P_{sat} of the annealing chamber (and thereby the solvent uptake ϕ_s at any given time) could be carefully monitored in-situ by varying the temperature of the sample stage ($\pm$ 0.1 °C) as shown schematically in **Figure 2.1**. By incrementally decreasing the temperature of the stage, the P/P_{sat} in the localized area of the BCP film is increased leading to a greater degree of solvent uptake. Conversely, if the stage temperature is increased, the P/P_{sat} will decrease inducing solvent expulsion from the film.[35, 38] This setup is an upgraded version of the system described by Lundy et al, with the addition of a reflectometer that allows in-situ monitoring of film swelling.[38]

Various kinetic parameters of the film swelling experiments such as the swelling ratio, swelling time, and rate of swelling, were controlled through precise variation of the stage temperature ($\pm$ 0.1 °C), while maintaining a constant solvent temperature of 21.0 $\pm$ 0.1 °C in the bubbler. The noted degree of accuracy for the stage temperature is essential for the controlled swelling of BCP films to high values of ϕ_s, as even small fluctuations (>0.25°C) in sample temperature at high swelling regimes can result in dramatic variations in the swollen film thickness.[35] The setup was contained in a fume hood that was maintained at a lab temperature of ~21 $\pm$ 1 °C. By decreasing the temperature of the stage, the relative saturation of the solvent vapor was increased, thus increasing the swelling ratio of the film.[23]

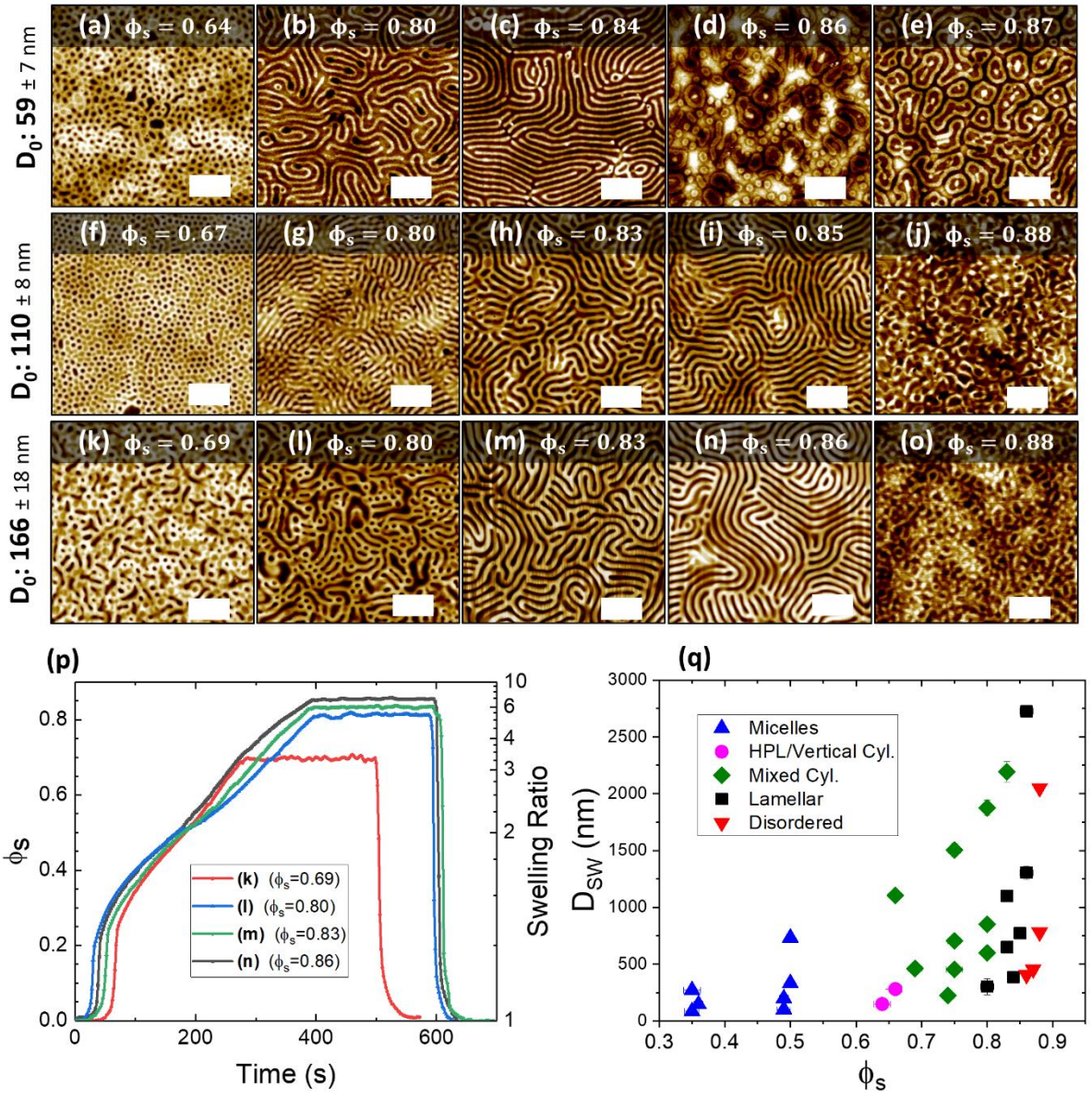

Figure 2.2. AFM images (a)-(o) show PS-*b*-P2VP films of varying thicknesses annealed in 2:1 chloroform:THF vapor up to a range of solvent concentration (ϕ_s) values. All scale bars are 1 μm. Once the targeted value of ϕ_s was reached, the films were held at this value for approximately 200s before being rapidly quenched in order to preserve the phase-separated structure. (p) Examples solvent uptake plots for (k) – (n) during SVA, with the corresponding ϕ_s value shown inset that the film was held at for 200s. (q) is an orientation diagram of the swollen film thickness D_{sw} as a function of ϕ_s, with the colour of each data point conveying the resulting morphology of the film post-SVA.

The annealing solvent of choice for this study was a blend of THF and chloroform, both of which are relatively non-selective to both PS and P2VP segments (slight selectivity of

THF to PS, and chloroform to P2VP).[37, 51] A range of solvent blend ratios were trialed in order to optimize the phase separation of the BCP system (See **Section S1**), of which a 2:1 molar ratio of chloroform to THF was chosen as the optimal blend ratio for the kinetic studies described below. This was calculated to give a ratio of approximately 82:18 of chloroform to THF in the vapor phase, due to the non-ideality of the solvent mixture.[52] Both THF and chloroform have high vapor pressures with values that are relatively close at 21 ℃ (136 mmHg and 165 mmHg respectively, see **Section S3.7.1.**), therefore it was assumed that the mole fractions of both solvents within the bubbler did not vary significantly over the annealing timescales analyzed in this work. A full description of the solvent variation experiments, including AFM images of samples along with a calculation of the resulting vapor phase mole fractions accounting for the nonideality of the mixture, is contained in the **Section S3.7.1**. A detailed analysis of the effect of solvent mixtures will be the subject of a future study.

As a starting point for this kinetic study, we decided to examine the effects of varying both D_0 and ϕ_S on the resulting phase-separated morphologies of the BCP system. **Figure 2.2(a-o)** shows a set of AFM images of the PS-b-P2VP BCP film annealed as a function of both D_0 and ϕ_s. The value of D_0 was varied by adjusting the concentration of the BCP dissolved in solution prior to spin-coating (from 1 to 3% w/w), giving an initial thickness range of ~ 59 to 371 nm. The films were swollen to a range of ϕ_S values, calculated from in situ monitoring of film thickness during SVA, and held at the set value for approximately 200s before rapid deswelling through N_2 purging of the chamber. Rapid quenching of the solvent is essential to 'kinetically trap' the film morphology in the swollen state upon drying.[35, 45, 53] The temperature conditions for the films were kept as constant as possible to ensure the swelling rate remained similar for all films, with an initial stage temperature of 19.9 ℃ and a bubbler temperature of 21.0 ℃. Some slight variation in swelling profiles between samples is noted (**Figure 2.2p**), which we attribute to minor daily temperature fluctuations in the lab environment. To avoid any excessive fluctuation in ϕ_s during the 200s hold time, the stage temperature was manually varied in increments of $\pm$0.1 ℃. The total annealing times were between ~ 8 – 11 minutes, with samples held at higher ϕ_s values requiring slightly longer swelling times as shown in the example set of in-situ swelling plots for the 166 nm films (**Figure 2.2p**).

A significant evolution of the film morphology was observed as the value of ϕ_s (that the films were held at) was increased. Below a ϕ_s value of ~ 0.64, no structural change was observed for any value of D_0, with the films remaining in an apparent vitrified micellar state as seen in previous studies.[39, 43] At ϕ_s values of between ~ 0.64 to 0.67, as can be seen in **Figures 2.2(a**, **e)**, a perpendicular cylindrical surface structure emerged for D_0 values of ~ 59 and 118 nm. We suggest that this is a hexagonally perforated lamellar (HPL) structure, as we previously observed through static SVA of this system.[12] The formation of the HPL phase is attributed to confinement effects as the film thickness decreases below the domain period L_0, and the limited maneuverability of the polymer chains at low values of ϕ_s.[27, 54] As the thickness of the unswollen dry BCP film moves toward commensurability ($D_0 \geq$ ~ 166 nm), as was the case in **Figure 2.2k**, the HPL phase was not observed at the same ϕ_s values and a poorly ordered mixed cylindrical structure was instead noted. As ϕ_s was further increased to between ~ 0.80 and 0.87, well-developed lamellar structures were observed to emerge at all D_0 values. The domain period L_0 of these structures was determined to be 193 nm from power spectrum density (PSD) plots of AFM images (See **Figure S3.7.7**). Interestingly, we observed a slight correlation between the critical ϕ_s value at which the onset of phase separation occurred ($\phi_{s,c}$) and D_0, with the onset shifting toward lower ϕ_s values for thinner films. This is likely due to a reduction in the amount of entangled material required to rearrange at lower D_0 values, which has been shown in previous work to result in faster ordering kinetics.[55] We attribute the high observed value of $\phi_{s,c}$ to the larger chain lengths and subsequent high level of entanglement associated with this UHMW system.

In the case of the films with $D_0 = 59 - 118$ nm, the HPL phase (**Figure 2.2(a, e)**) was observed to undergo an order-order transition (OOT) to a lamellar structure (**Figure 2.2(b, h)**) upon increasing ϕ_s, in agreement with previous work.[56] The ordering of the lamellar domains improved with increasing ϕ_s up to a D_0-dependent value of ~ 0.84 to 0.87. Upon further swelling above these values, the films appeared to undergo an order-disorder transition (ODT) with the loss of any observable surface ordering. Additionally, maintaining regular ϕ_s values above 0.87 was found to be difficult for all film thicknesses due to the intermittent breakdown of the reflectometer model, which we attribute to partial dewetting of the films during SVA. A slight thickness dependence

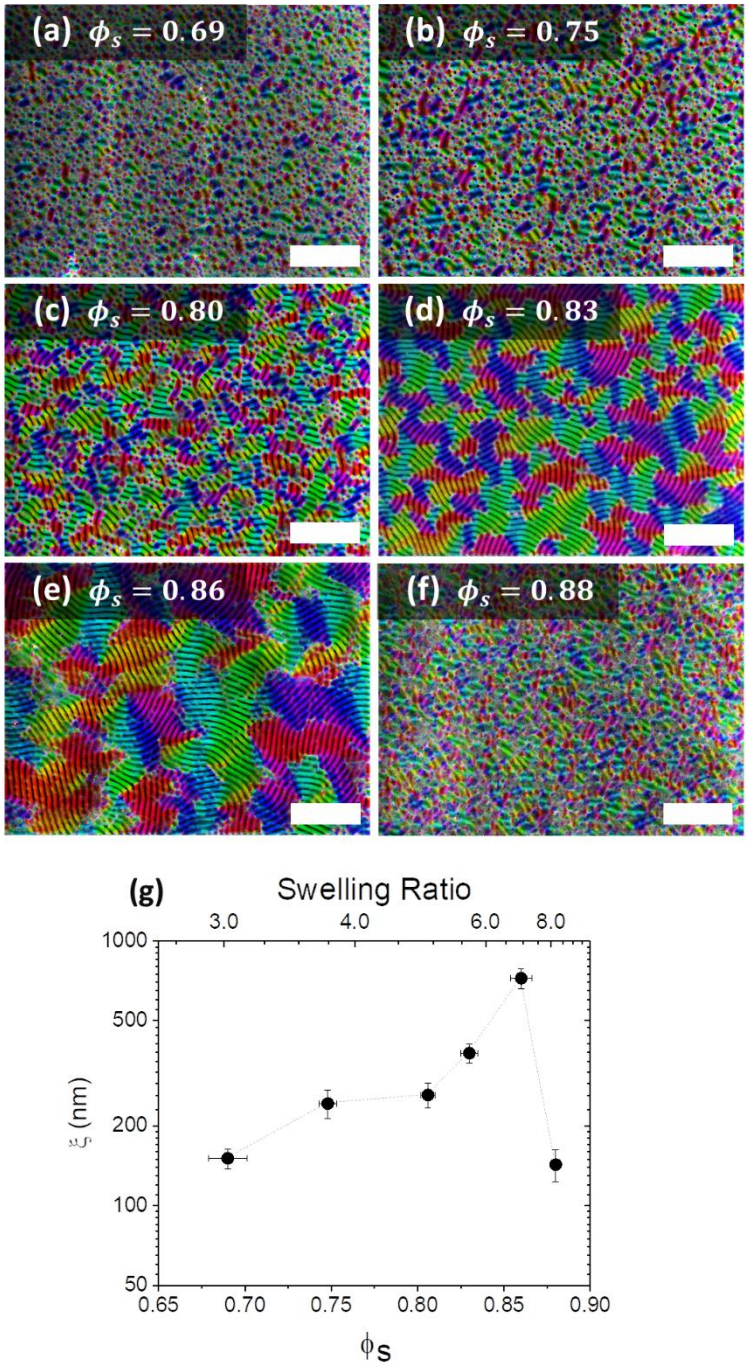

Figure 2.3. (a)-(d): Orientational mapping of SEM images showing grains parallel to the surface after swelling to different values of solvent concentration (ϕ_s): (a) $\phi_s = 0.69$, (b) $\phi_s = 0.75$, (c) $\phi_s = 0.80$, (d) $\phi_s = 0.83$, (e) $\phi_s = 0.86$ (f) $\phi_s = 0.88$, (g) correlation length ξ as a function of ϕ_s and the swelling ratio. Scale bars are 2 μm.

was observed for the value of ϕ_s at the ODT (henceforth referred to as $\phi_{s,ODT}$), with lower D_0 resulting in a slightly lower $\phi_{s,ODT}$. A likely explanation for this dependency is the reduction in polymeric material resulting in less required molecular rearrangement,

as mentioned previously. The complete range of ϕ_s values and their resulting morphologies are summarized in the orientation diagram shown in **Figure 2.2n**, with their corresponding AFM images available in **Figure S3.7.8**.The effect of ϕ_s on the lateral ordering is more closely examined in **Figure 2.3**.

In order to quantify the effect of ϕ_s on the lateral ordering of the lamellar features, we used image analysis software to generate orientation maps of the BCP films after SVA. **Figure 2.3(a-f)** shows colorized SEM images of the PS-b-P2VP films with $D_0 = \sim 166$ nm swollen to and held at various values of ϕ_s $(0.69 - 0.88)$ for 200s followed by rapid deswelling (same annealing conditions as **Figure 2.2**), with the coloring representing the orientation of the lamellar microdomains. The orientational ordering of the films increases with the ϕ_s value reached during swelling, with significant microdomain orientation only observed at $\phi_s = \sim 0.83$ or higher. The maximum grain size was achieved at $\phi_s = \sim 0.86$, with complete disordering of the phase-separated lamellar structure observed at $\phi_s = \sim 0.88$. The ODT value of ϕ_s can therefore be cautiously estimated to lie close to the value of $\phi_s = \sim 0.87$. The grain size was further quantitatively characterized by determining the microdomain correlation length ξ for the lateral ordering of the lamellar structures for each sample, shown in **Figure 2.3g**.[55, 57] At low levels of ϕ_s, the value of ξ remains at a value close to the domain period of ~190 nm. The highest value of $\xi = 723 \pm 62$ nm was obtained through annealing at the closest possible ϕ_s value (0.86) to our estimated ODT concentration of $\phi_s = \sim 0.87$. Once the swelling surpassed this point, as was the case with **Figure 2.3f** where $\phi_s = 0.88$, long range ordering was lost and the value of ξ returned to the order of roughly a single domain period.

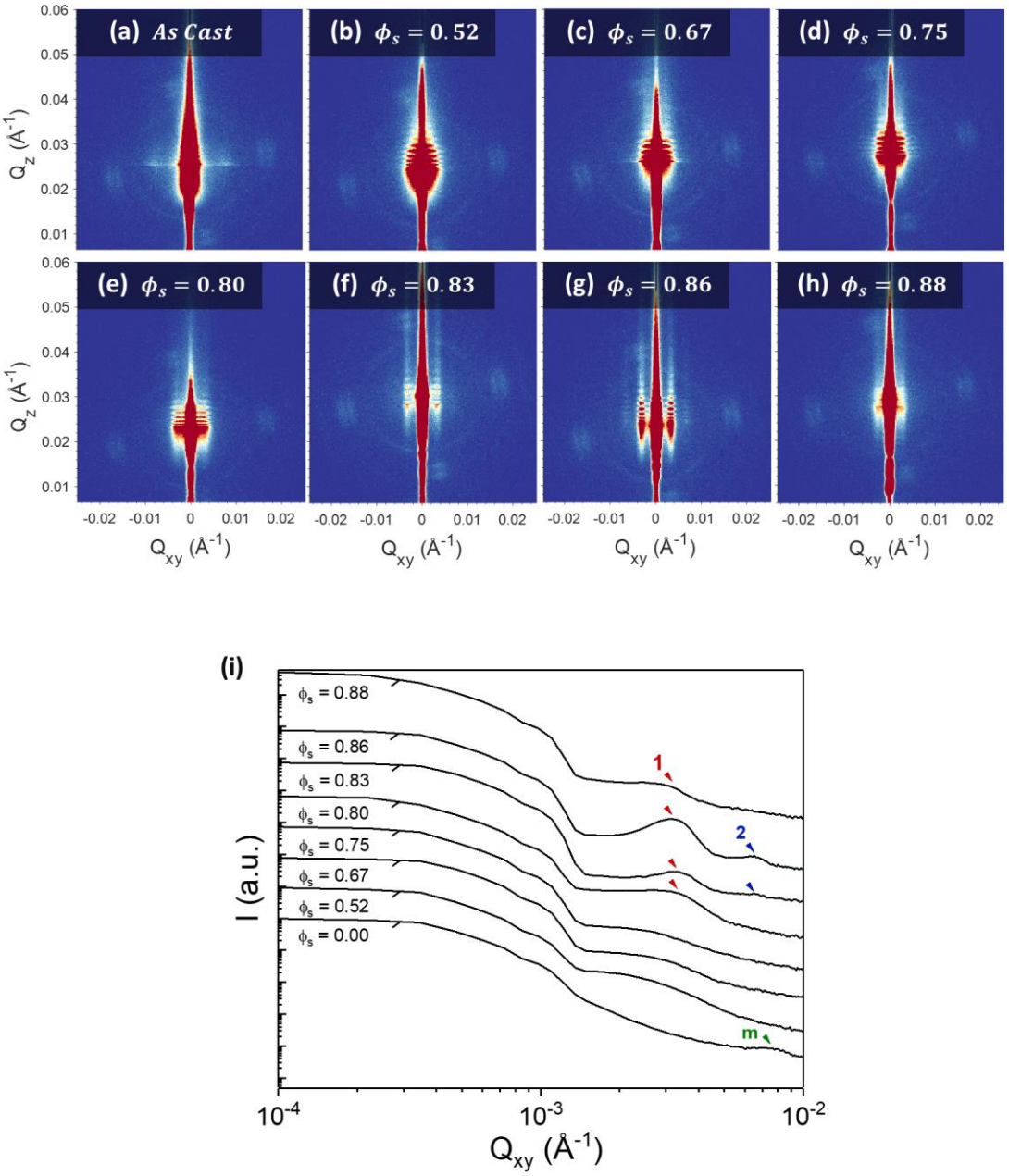

Figure 2.4: (a)-(h): 2-dimensional GISAXS scattering patterns showing the morphological evolution of the 166 nm PS-*b*-P2VP films swollen to different values of ϕ_S. Films were held at the noted value of ϕ_s for ~ 200 s before rapid deswelling. (i) 1-D Intensity profiles extracted from the GISAXS images at the determined Yoneda position for each sample. First order, second order scattering peaks are marked as 1 and 2, and scattering peak for as-cast micelle film as *m*.

GISAXS was then used to examine the effect of ϕ_s on the internal structure of the 166 nm BCP films over macroscopic areas. Measurements were taken of the films after rapid deswelling with no subsequent processing, as shown in the GISAXS images in **Figures**

2.4(a-h) along with the 1D in-plane intensity profiles in **Figure 2.4i**. The 1D intensity profiles were extracted from the GISAXS images at the determined Yoneda position for each sample. A clear evolution of morphology can be observed as ϕ_s increases. For the as-cast film, a very weak scattering pattern is evident in **Figure 2.4a** – this indicates a mainly disordered film, which can be attributed to the kinetically-trapped state after rapid solvent evaporation during spin-coating.[58] A weak scattering peak is evident in **Figure 2.4i** (marked as *m* in green) at a Qxy value of ~ 7.98×10^{-3} $Å^{-1}$, which corresponds to a domain spacing d of ~79 nm (using $d = \frac{2\pi}{Q_{xy}}$); this likely originates from the micellar structures evident in AFM images of the as-cast film surface (shown in **Figure S2.7.7**). For films swollen to a ϕ_s value of between 0.52 to 0.75 (**Figure 2.4(b-d)**) no notable scattering peaks are observed, which suggests that the BCP chains are still too entangled at this level of swelling to self-assemble into well-defined microdomains. Upon reaching a ϕ_s value of 0.80 (**Figure 2.4e**), a first-order scattering peak (marked as 1 in red) begins to emerge at a Qxy value of approximately 3.33×10^{-3} $Å^{-1}$. This peak sharpens and intensifies in strength along Qz as ϕ_s is increased to 0.83 and then to 0.86 (**Figure 2.4(f, g))** indicating a structural transition to a perpendicular lamellar morphology once the films exceed the threshold ϕ_s value of ~ 0.8. The extension of the perpendicular lamellar morphology throughout the entire thickness of the film is further proven by cross-sectional FIB/SEM analysis (see **Figure S2.7.10**). The in-plane domain spacing d at $\phi_s = 0.83$ is calculated to be approximately ~184 nm ($Q_{xy} = 3.41 \times 10^{-3}$ $Å^{-1}$), while at $\phi_s = 0.86$ this increases to 191 nm ($Q_{xy} = 3.29 \times 10^{-3}$ $Å^{-1}$). These values are in close agreement with lamellar spacing values calculated from AFM (see **Figure S2.7.8**). A weak second order peak is also visible at 2Qxy* (marked as 2 in blue in **Figure 2.4i**), which again is indicative of the development of well-ordered perpendicular lamellar domains in the film.[59] Once the value of ϕ_s is increased to 0.88 (**Figure 2.4h**), the first order peak is observed to diminish and the second order peak vanishes. This infers a loss of structural ordering throughout the BCP film as it undergoes an ODT, which is in agreement with the surface transition shown in AFM images (see **Figure 2.2(n, o)**). Oscillations in Qz can be observed for all ϕ_S values between 0.52 to 0.86, which we suggest arise from surface roughness correlation effects between the polymer film and the substrate.[60]

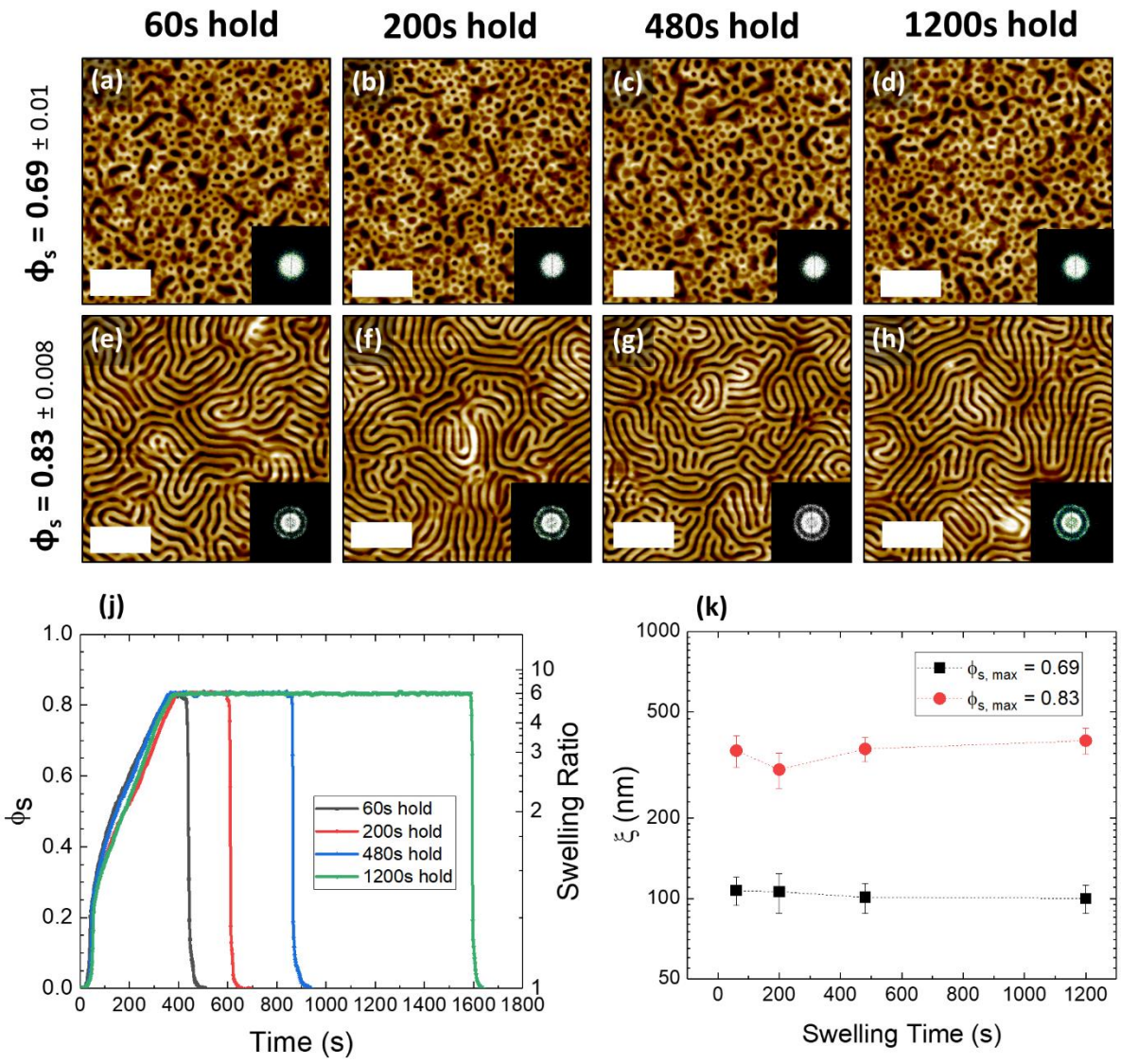

Figure 2.5: AFM images (a)-(d) show PS-*b*-P2VP films annealed to a solvent concentration (ϕ_s) value of 0.69 and held at this value for different amounts of time (ST = 60, 200, 480 and 1200 seconds). (e)-(h) are annealed to $\phi_s = 0.83$ and held for the same timescales. Corresponding Fourier transforms are shown inset. (j) shows the swelling profiles for (e)-(h), as a function of ϕ_s and swelling ratio. (k) shows the variation of the correlation length ξ with swelling time. All scale bars are 1 µm.

In order to fully optimize and understand the annealing process, it was critical to determine the effect of the annealing time on the relative ordering and morphologies of the BCP films. A series of BCP films with a D_0 value of ~166 nm were swollen to either ~ $3D_0$ ($\phi_s = 0.69$) or ~ $6D_0$ ($\phi_S = 0.83$), and held at that swelling ratio for varying amounts of time between 60-1200 seconds, as shown in **Figure 2.5j** for the $\phi_S = 0.83$

samples ($\phi_s = 0.69$ profiles shown in **Figure S2.7.4**). The rate of swelling was maintained by controlling the stage and bubbler temperatures. For both values of ϕ_s, it was observed that the amount of time the BCP was held at a particular solvent concentration did not significantly affect the morphology or ordering of the resulting structure. In the case of **Figures 2.5(a-d)**, where the films were swollen to $3D_0$, the increased swelling time did not result in a more ordered or developed structure. This is furthermore confirmed by the low level of variation in the value of ξ in **Figure 2.5k**. In the case of the films swollen to $6D_0$, phase separation was induced but again, the increase in swelling time did not result in any observed increase in lateral ordering, and the value of ξ remained with the range of approximately 300-400 nm. These results reinforce the existence of a minimum ϕ_s value, below which the BCP films will remain in a vitrified state regardless of the annealing time.[53] This observation is also in agreement with previous work on lower molecular weight cylinder-forming PS-b-P2VP systems that showed minimal change in the ξ with longer annealing times.[43]

The influence of the swelling kinetics was further examined through varying the rate of swelling as solvent was uptaken into the films. This was achieved by setting different values of the stage temperature (between 15.9 – 20.9 °C, see **Figure S2.7.6**) during the initial solvent uptake component of the annealing, with a constant bubbler temperature and N_2 flow as before. **Figure 2.6** shows AFM images of the BCP film with the same D_0 value of ~166 nm annealed to approximately ~$5D_0$ ($\phi_s = 0.80$) or ~$7D_0$ ($\phi_s = 0.86$). The rate of solvent uptake was measured as the change in solvent concentration inside the BCP film over time, $\frac{d\phi_s}{dt}$, and was calculated by fitting a linear regression model to the metered solvent uptake regime of the plots (example plots shown in **Figure 2.6g**), ignoring the initial solvent uptake regime between ϕ_s values of $0 - 0.25$.[39] Once the desired film thickness was reached, minor adjustments were made to the stage temperature in order to maintain a constant thickness value for ~200 seconds, before rapid deswelling.

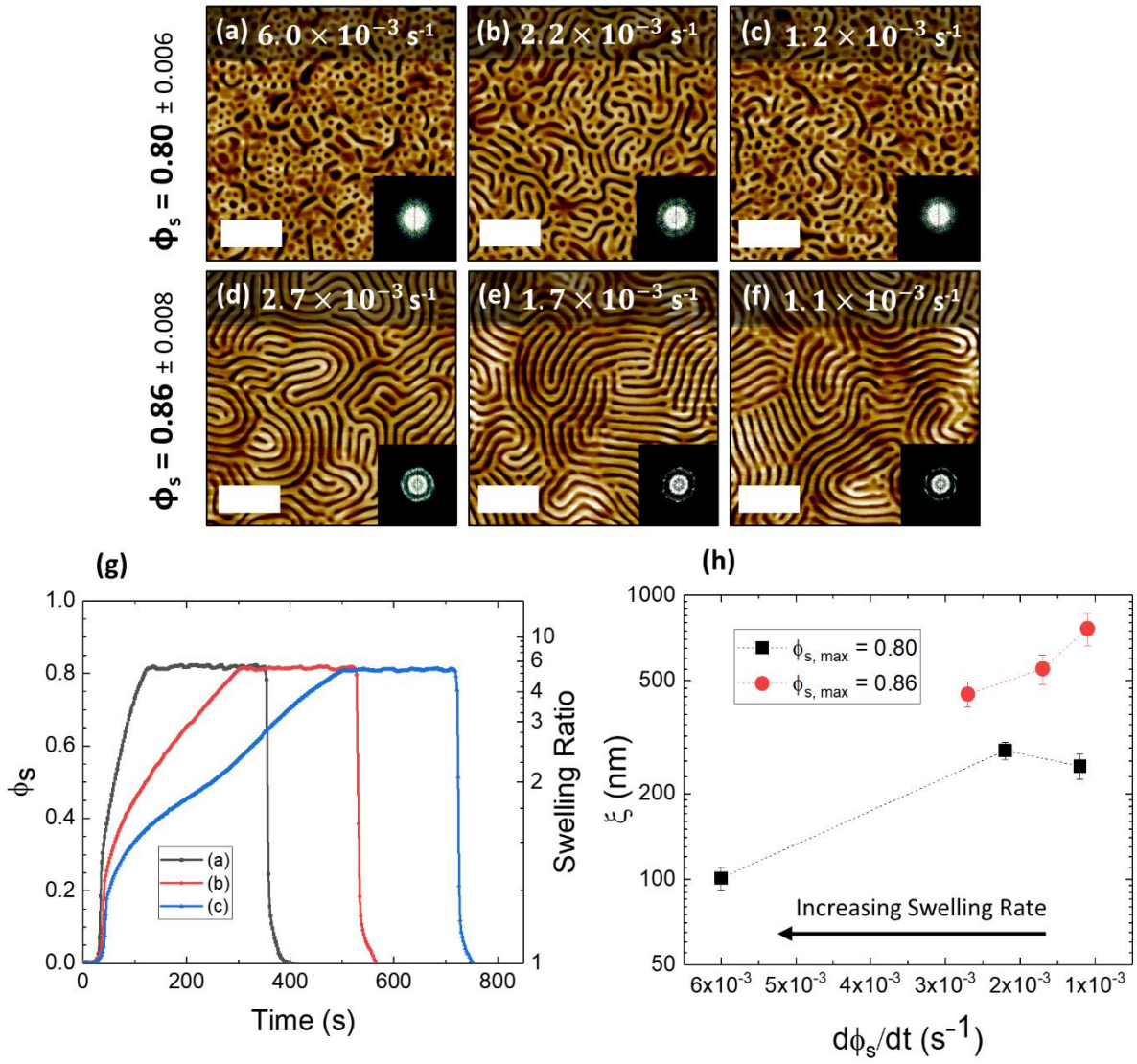

Figure 2.6: The effect of the rate of solvent uptake $\left(\frac{d\phi}{dt}\right)$ on lateral ordering for two different values of ϕ_s**.** AFM images of films with different swelling rates for film reaching maximum $\phi_s = 0.8$ **(a)-(c)**, and maximum $\phi_s = 0.86$ (d)-(f). Fourier transforms are shown in the insert. (g) solvent annealing profile for (a)-(c) as a function of ϕ_s and swelling ratio at different swelling rate. (h) correlation length ξ at different swelling rate, indicating the slower swelling rate improves the micro-domain correlation length. All scale bars are 1 μm.

In the case of **Figure 2.6(a-c)**, where the films were swollen to a ϕ_s value of 0.8, the rate of swelling was varied from 1.2×10^{-3} s^{-1} to 6×10^{-3} s^{-1}(black square data points in Figure 6h). No significant structural change was observed as the value of $\frac{d\phi_s}{dt}$

was varied, and the BCP films remained in the region of the partially self-assembled state. A slight improvement in the calculated value of ξ is observed for films with $\phi_s = 0.8$ in **Figure 2.6h. Figures 2.6(d-f)** show improvement in ordering as the swelling rate decreased from $2.7 \times 10^{-3} s^{-1}$ to $1.1 \times 10^{-3}\ s^{-1}$ (red circle data points in **Figure 2.6h**), with the value of ξ increasing from 449 nm up to 724 nm.

A definitive explanation for this observation is difficult to ascertain, as little previous studies have investigated the influence of swelling rate on the ordering of BCP films. One possibility is that a slower swelling rate may result in less trapping of structural defects, thus resulting in larger ξ values. Nonetheless, a previous study has noted that the swelling rate did not noticeably influence their results for a smaller BCP system.[40] Hence, we believe that future, more detailed kinetic studies are required to fully interpret these experimental results. It should be noted that the range of swelling rates examined for the $\phi_s = 0.86$ sample set is smaller than for $\phi_s = 0.8$. This is because it was found that our reflectometer model began to fail at swelling rates that exceeded approximately $3 \times 10^{-3}\ s^{-1}$ for the films swollen to $\phi_s = 0.86$. We suggest that this may be the result of increased macro-scale film roughness caused by the rapid and non-uniform absorption of solvent into the film during a fast initial swelling regime, which is likely exacerbated at higher ϕ_s values. This established an experimental limit for the highest possible swelling rate shown in this work. It may be feasible to further accelerate the self-assembly process with a more uniform solvent distribution system in the chamber, or different instrumentation to account for a large roughness factor during the in-situ measurement of film thickness.

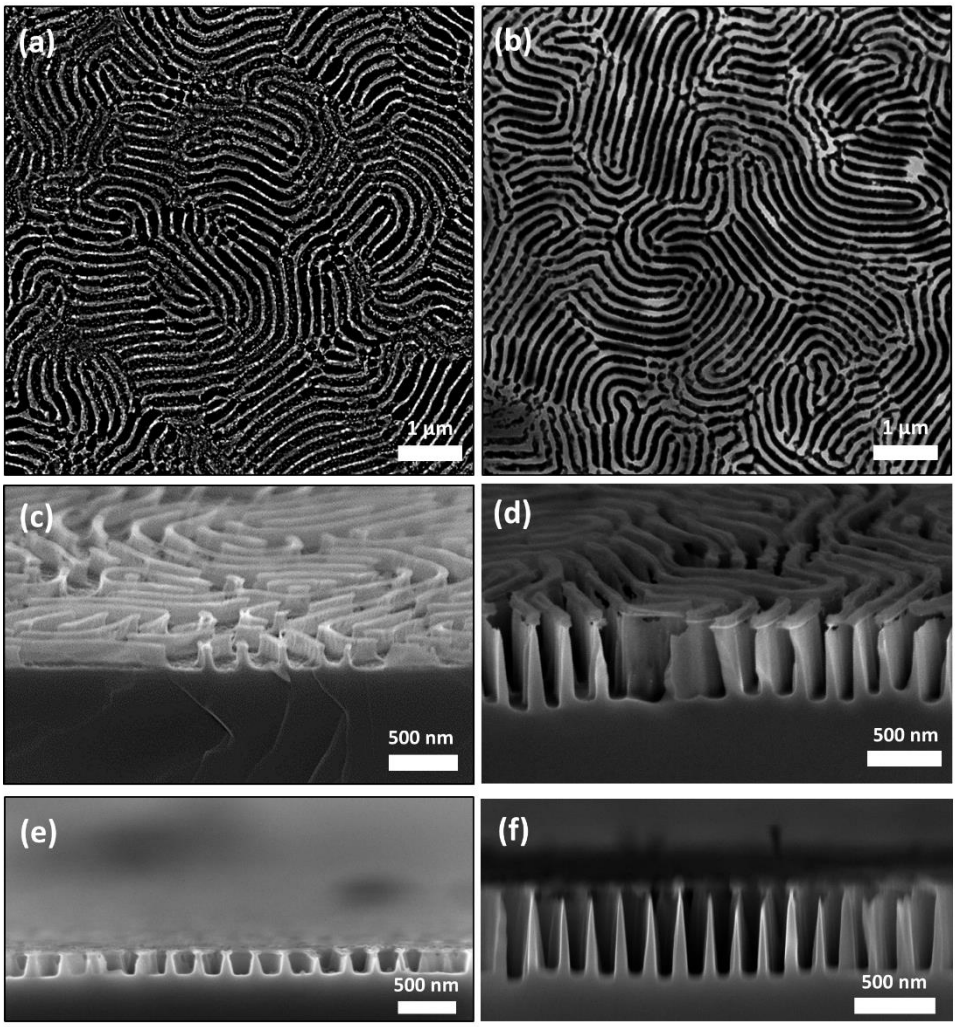

Figure 2.7: SEM images of Si nanowall after pattern transfer. Top-down SEM images of Si nanowall structures following an ICP etch of the iron oxide hardmask for (a) 1 minute, and (b) 3 minutes etch, with tilted images (70°) shown in (c) and (d) respectively. (e), (f) show cross-sectional SEM image of Si nanowalls for samples (a) and (b).

In order to demonstrate the pattern transfer capability of the self-assembled films, a liquid phase metal salt infiltration process followed by UV/O3 treatment (to remove the polymer matrix) was performed to convert the BCP film into template for the formation of metal oxide nanostructures. This type of hard mask fabrication process has proven highly successful in previous work for manufacturing a variety of Si nanostructures.[12, 61, 62] The metal oxide templates were then used as a etch mask, and the samples were etched for a range of times via an ICP-RIE plasma etching technique using CHF3 and SF6 process gases. In the case of samples with etch times of up to 1 minute, an iron oxide hardmask was employed via infiltration of iron nitrate (Fe(NO3)2), while for etch times

of up to 3 minutes a nickel oxide mask (from a nickel nitrate precursor) was instead used. This is because it was found that the nickel oxide mask was more durable over the longer etch times and resulted in less structural degradation and higher etch contrast. **Figure 2.7(a-f)** show SEM images of the resulting Si nanowall structures after 1 minute and 3 minutes, demonstrating a high degree of homogeneity over the sample surfaces. **Figures 2.7(e, f)** show cross-sectional SEM images of the Si nanowall features, again showing uniform nanowall structures with feature spacings of ~ 190 nm and heights of ~ 145 and ~ 493 nm respectively. The aspect ratio of the features shown in the 3 minute etched sample (**Figure 2.7f**) was measured to be approximately 7.5. The successful pattern transfer of the BCP film and generation of vertical sidewalls furthermore confirms the efficacy of the optimized SVA process. A summary table of the variation of feature heights with etch time is displayed in **Figure S2.7.13**, along with high-resolution cross-sectional SEM images of the nanowall structures.

2.5. Conclusion

In order for BCP lithography to become a viable candidate for the fabrication of large period (>100 nm) nanostructures, it is critical that the self-assembly of UHMW systems be enhanced for maximal structural control and minimal annealing time. We studied the swelling kinetics of an UHMW BCP system through the use of a temperature-controlled solvent annealing rig, allowing for precise control over the pattern structure, ordering, over a very short period of annealing time. We show that at very high levels of solvent uptake ($\phi_s \geq 0.8$), where the polymer concentration is close to the experimentally estimated ODT point, it is possible for an UHMW BCP system to undergo rapid phase separation into lamellar domains of 190 nm spacing on timescales of 10 minutes. The closer the value of ϕ_s becomes to the observed $\phi_{s,ODT}$ value, the higher the lateral ordering of the film. The thickness of the dry BCP film was found to positively correlate with both the minimum ϕ_s value required to initiate self-assembly, along with the observed ODT value of ϕ_s. Furthermore, when D_0 was modulated in conjunction with ϕ_s, the domain morphology could be induced to obtain the kinetically unstable HPL phase at a thickness close to half that of the domain period.[12] The amount of time a polymer film is held at a particular value of ϕ_S is shown not to appreciably impact the ordering or domain structure. The rate of solvent uptake, on the other hand, exhibits a moderate influence on the domain ordering for ϕ_s values that are sufficiently high to

induce phase separation, with slower swelling rates resulting in improved lateral ordering. It should be noted that the optimization of lateral ordering was somewhat limited by the temperature sensitivity of our annealing setup; we anticipate that future studies may achieve even higher degrees of ordering through controllably approaching the ODT point with greater accuracy. The domain structures obtained from these self-assembled BCP films were easily utilized for pattern transfer through metal salt inclusion, with the formation of metal oxide hard masks that were etched to create uniform and regular arrays of high aspect ratio Si nanowall features.

In conclusion, the results of this study demonstrate that a considerable reduction in the annealing time of UHMW BCP systems is possible using a carefully regulated SVA-based approach, improving upon previous work that typically required high temperature annealing and/or timescales on the order of hours or days.[20, 28-30] The speed and reliability of this technique represents a major step towards a cost-effective and scalable strategy for the fabrication of optical nanostructures such as 2D photonic crystal structures[63, 64] using BCP lithography, with feature spacings on the order of visible light.

2.6. References

1. Bates, F. S.; Fredrickson, G. H., Block Copolymer Thermodynamics: Theory and Experiment. *Annual Review of Physical Chemistry* **1990,** *41* (1), 525-557.
2. Matsen, M. W.; Bates, F. S., Origins of Complex Self-Assembly in Block Copolymers. *Macromolecules* **1996,** *29* (23), 7641-7644.
3. Park, C.; Yoon, J.; Thomas, E. L., Enabling nanotechnology with self assembled block copolymer patterns. *Polymer* **2003,** *44* (22), 6725-6760.
4. Cummins, C.; Ghoshal, T.; Holmes, J. D.; Morris, M. A., Strategies for Inorganic Incorporation using Neat Block Copolymer Thin Films for Etch Mask Function and Nanotechnological Application. *Advanced Materials* **2016,** *28* (27), 5586-5618.
5. Cummins, C.; Lundy, R.; Walsh, J. J.; Ponsinet, V.; Fleury, G.; Morris, M. A., Enabling future nanomanufacturing through block copolymer self-assembly: A review. *Nano Today* **2020,** *35*, 100936.
6. Subramanian, A.; Doerk, G.; Kisslinger, K.; Yi, D. H.; Grubbs, R. B.; Nam, C.-Y., Three-dimensional electroactive ZnO nanomesh directly derived from hierarchically self-assembled block copolymer thin films. *Nanoscale* **2019,** *11* (19), 9533-9546.
7. Bas, S. Z.; Cummins, C.; Selkirk, A.; Borah, D.; Ozmen, M.; Morris, M. A., A Novel Electrochemical Sensor Based on Metal Ion Infiltrated Block Copolymer Thin Films for Sensitive and Selective Determination of Dopamine. *ACS Applied Nano Materials* **2019,** *2* (11), 7311-7318.
8. Harandizadeh, Z.; Ito, T., Block Copolymer-Derived Recessed Nanodisk-Array Electrodes as Platforms for Folding-Based Electrochemical DNA Sensors. *ChemElectroChem* **2019,** *6* (22), 5627-5632.
9. Jung, Y. S.; Jung, W.; Tuller, H. L.; Ross, C. A., Nanowire Conductive Polymer Gas Sensor Patterned Using Self-Assembled Block Copolymer Lithography. *Nano Letters* **2008,** *8* (11), 3776-3780.
10. Li, X.; Xue, L.; Han, Y., Broadband antireflection of block copolymer/homopolymer blend films with gradient refractive index structures. *Journal of Materials Chemistry* **2011,** *21* (15), 5817-5826.
11. Mir, S. H.; Rydzek, G.; Nagahara, L. A.; Khosla, A.; Mokarian-Tabari, P., Review—Recent Advances in Block-Copolymer Nanostructured Subwavelength Antireflective Surfaces. *Journal of The Electrochemical Society* **2019,** *167* (3), 037502.
12. Mokarian-Tabari, P.; Senthamaraikannan, R.; Glynn, C.; Collins, T. W.; Cummins, C.; Nugent, D.; O'Dwyer, C.; Morris, M. A., Large Block Copolymer Self-Assembly for Fabrication of Subwavelength Nanostructures for Applications in Optics. *Nano Letters* **2017,** *17* (5), 2973-2978.
13. Rahman, A.; Ashraf, A.; Xin, H.; Tong, X.; Sutter, P.; Eisaman, M. D.; Black, C. T., Sub-50-nm self-assembled nanotextures for enhanced broadband antireflection in silicon solar cells. *Nature Communications* **2015,** *6* (1), 5963.
14. Park, T. H.; Yu, S.; Cho, S. H.; Kang, H. S.; Kim, Y.; Kim, M. J.; Eoh, H.; Park, C.; Jeong, B.; Lee, S. W.; Ryu, D. Y.; Huh, J.; Park, C., Block copolymer structural color strain sensor. *NPG Asia Materials* **2018,** *10* (4), 328-339.

15. Song, D.-P.; Jacucci, G.; Dundar, F.; Naik, A.; Fei, H.-F.; Vignolini, S.; Watkins, J. J., Photonic Resins: Designing Optical Appearance via Block Copolymer Self-Assembly. *Macromolecules* **2018,** *51* (6), 2395-2400.
16. Heo, M.; Cho, H.; Jung, J.-W.; Jeong, J.-R.; Park, S.; Kim, J. Y., High-Performance Organic Optoelectronic Devices Enhanced by Surface Plasmon Resonance. *Advanced Materials* **2011,** *23* (47), 5689-5693.
17. Kang, Y.; Walish, J. J.; Gorishnyy, T.; Thomas, E. L., Broad-wavelength-range chemically tunable block-copolymer photonic gels. *Nature Materials* **2007,** *6* (12), 957-960.
18. Lee, J.-H.; Koh, C. Y.; Singer, J. P.; Jeon, S.-J.; Maldovan, M.; Stein, O.; Thomas, E. L., 25th Anniversary Article: Ordered Polymer Structures for the Engineering of Photons and Phonons. *Advanced Materials* **2014,** *26* (4), 532-569.
19. Mapas, J. K. D.; Thomay, T.; Cartwright, A. N.; Ilavsky, J.; Rzayev, J., Ultrahigh Molecular Weight Linear Block Copolymers: Rapid Access by Reversible-Deactivation Radical Polymerization and Self-Assembly into Large Domain Nanostructures. *Macromolecules* **2016,** *49* (10), 3733-3738.
20. Kim, E.; Ahn, H.; Park, S.; Lee, H.; Lee, M.; Lee, S.; Kim, T.; Kwak, E.-A.; Lee, J. H.; Lei, X.; Huh, J.; Bang, J.; Lee, B.; Ryu, D. Y., Directed Assembly of High Molecular Weight Block Copolymers: Highly Ordered Line Patterns of Perpendicularly Oriented Lamellae with Large Periods. *ACS Nano* **2013,** *7* (3), 1952-1960.
21. Jung, Y. S.; Ross, C. A., Solvent-Vapor-Induced Tunability of Self-Assembled Block Copolymer Patterns. *Advanced Materials* **2009,** *21* (24), 2540-2545.
22. Sinturel, C.; Vayer, M.; Morris, M.; Hillmyer, M. A., Solvent Vapor Annealing of Block Polymer Thin Films. *Macromolecules* **2013,** *46* (14), 5399-5415.
23. Gotrik, K. W.; Hannon, A. F.; Son, J. G.; Keller, B.; Alexander-Katz, A.; Ross, C. A., Morphology Control in Block Copolymer Films Using Mixed Solvent Vapors. *ACS Nano* **2012,** *6* (9), 8052-8059.
24. Kim, S. H.; Misner, M. J.; Russell, T. P., Controlling Orientation and Order in Block Copolymer Thin Films. *Advanced Materials* **2008,** *20* (24), 4851-4856.
25. Jung, Y. S.; Ross, C. A., Orientation-Controlled Self-Assembled Nanolithography Using a Polystyrene−Polydimethylsiloxane Block Copolymer. *Nano Letters* **2007,** *7* (7), 2046-2050.
26. Wan, L.; Ji, S.; Liu, C.-C.; Craig, G. S. W.; Nealey, P. F., Directed self-assembly of solvent-vapor-induced non-bulk block copolymer morphologies on nanopatterned substrates. *Soft Matter* **2016,** *12* (11), 2914-2922.
27. Bai, W.; Hannon, A. F.; Gotrik, K. W.; Choi, H. K.; Aissou, K.; Liontos, G.; Ntetsikas, K.; Alexander-Katz, A.; Avgeropoulos, A.; Ross, C. A., Thin Film Morphologies of Bulk-Gyroid Polystyrene-block-polydimethylsiloxane under Solvent Vapor Annealing. *Macromolecules* **2014,** *47* (17), 6000-6008.
28. Cao, W.; Xia, S.; Appold, M.; Saxena, N.; Bießmann, L.; Grott, S.; Li, N.; Gallei, M.; Bernstorff, S.; Müller-Buschbaum, P., Self-Assembly in ultrahigh molecular weight sphere-forming diblock copolymer thin films under strong confinement. *Scientific Reports* **2019,** *9* (1), 18269.
29. Park, S.; Kim, Y.; Ahn, H.; Kim, J. H.; Yoo, P. J.; Ryu, D. Y., Giant Gyroid and Templates from High-Molecular-Weight Block Copolymer Self-assembly. *Scientific Reports* **2016,** *6* (1), 36326.
30. Takano, K.; Nyu, T.; Maekawa, T.; Seki, T.; Nakatani, R.; Komamura, T.; Hayakawa, T.; Hayashi, T., Real-time and in situ observation of structural evolution of giant block copolymer thin film under solvent vapor annealing by atomic force microscopy. *RSC Advances* **2020,** *10* (1), 70-75.

31. Doerk, G. S.; Li, R.; Fukuto, M.; Yager, K. G., Wet Brush Homopolymers as "Smart Solvents" for Rapid, Large Period Block Copolymer Thin Film Self-Assembly. *Macromolecules* **2020,** *53* (3), 1098-1113.
32. Cummins, C.; Alvarez-Fernandez, A.; Bentaleb, A.; Hadziioannou, G.; Ponsinet, V.; Fleury, G., Strategy for Enhancing Ultrahigh-Molecular-Weight Block Copolymer Chain Mobility to Access Large Period Sizes (>100 nm). *Langmuir* **2020,** *36* (46), 13872-13880.
33. Jin, C.; Olsen, B. C.; Luber, E. J.; Buriak, J. M., Nanopatterning via Solvent Vapor Annealing of Block Copolymer Thin Films. *Chemistry of Materials* **2017,** *29* (1), 176-188.
34. Mokarian-Tabari, P.; Cummins, C.; Rasappa, S.; Simao, C.; Sotomayor Torres, C. M.; Holmes, J. D.; Morris, M. A., Study of the Kinetics and Mechanism of Rapid Self-Assembly in Block Copolymer Thin Films during Solvo-Microwave Annealing. *Langmuir* **2014,** *30* (35), 10728-10739.
35. Hulkkonen, H.; Salminen, T.; Niemi, T., Automated solvent vapor annealing with nanometer scale control of film swelling for block copolymer thin films. *Soft Matter* **2019,** *15* (39), 7909-7917.
36. Knoll, A.; Magerle, R.; Krausch, G., Phase behavior in thin films of cylinder-forming ABA block copolymers: Experiments. *The Journal of Chemical Physics* **2004,** *120* (2), 1105-1116.
37. Gu, X.; Gunkel, I.; Hexemer, A.; Gu, W.; Russell, T. P., An In Situ Grazing Incidence X-Ray Scattering Study of Block Copolymer Thin Films During Solvent Vapor Annealing. *Advanced Materials* **2014,** *26* (2), 273-281.
38. Lundy, R.; Flynn, S. P.; Cummins, C.; Kelleher, S. M.; Collins, M. N.; Dalton, E.; Daniels, S.; Morris, M. A.; Enright, R., Controlled solvent vapor annealing of a high χ block copolymer thin film. *Physical Chemistry Chemical Physics* **2017,** *19* (4), 2805-2815.
39. Nelson, G.; Drapes, C. S.; Grant, M. A.; Gnabasik, R.; Wong, J.; Baruth, A., High-Precision Solvent Vapor Annealing for Block Copolymer Thin Films. *Micromachines* **2018,** *9* (6).
40. Baruth, A.; Seo, M.; Lin, C. H.; Walster, K.; Shankar, A.; Hillmyer, M. A.; Leighton, C., Optimization of Long-Range Order in Solvent Vapor Annealed Poly(styrene)-block-poly(lactide) Thin Films for Nanolithography. *ACS Applied Materials & Interfaces* **2014,** *6* (16), 13770-13781.
41. Cheng, X.; Böker, A.; Tsarkova, L., Temperature-Controlled Solvent Vapor Annealing of Thin Block Copolymer Films. *Polymers* **2019,** *11* (8), 1312.
42. Tsarkova, L.; Sevink, G. J. A.; Krausch, G., Nanopattern Evolution in Block Copolymer Films: Experiment, Simulations and Challenges. In *Complex Macromolecular Systems I*, Müller, A. H. E.; Schmidt, H.-W., Eds. Springer Berlin Heidelberg: Berlin, Heidelberg, 2010; pp 33-73.
43. Gu, X.; Gunkel, I.; Hexemer, A.; Russell, T. P., Controlling Domain Spacing and Grain Size in Cylindrical Block Copolymer Thin Films by Means of Thermal and Solvent Vapor Annealing. *Macromolecules* **2016,** *49* (9), 3373-3381.
44. Jiang, Z., GIXSGUI: a MATLAB toolbox for grazing-incidence X-ray scattering data visualization and reduction, and indexing of buried three-dimensional periodic nanostructured films. *Journal of Applied Crystallography* **2015,** *48* (3), 917-926.
45. Murphy, J. N.; Harris, K. D.; Buriak, J. M., Automated Defect and Correlation Length Analysis of Block Copolymer Thin Film Nanopatterns. *PLOS ONE* **2015,** *10* (7), e0133088.

46. Gu, X. Self-assembly of block copolymers by solvent vapor annealing, mechanism and lithographic applications. Doctoral Thesis, University of Massachusetts Amherst, 2014.
47. Koo, K.; Ahn, H.; Kim, S.-W.; Ryu, D. Y.; Russell, T. P., Directed self-assembly of block copolymers in the extreme: guiding microdomains from the small to the large. *Soft Matter* **2013,** *9* (38), 9059-9071.
48. Lodge, T. P.; Pan, C.; Jin, X.; Liu, Z.; Zhao, J.; Maurer, W. W.; Bates, F. S., Failure of the dilution approximation in block copolymer solutions. *Journal of Polymer Science Part B: Polymer Physics* **1995,** *33* (16), 2289-2293.
49. Lodge, T. P.; Hanley, K. J.; Pudil, B.; Alahapperuma, V., Phase Behavior of Block Copolymers in a Neutral Solvent. *Macromolecules* **2003,** *36* (3), 816-822.
50. Zhang, J.; Posselt, D.; Smilgies, D.-M.; Perlich, J.; Kyriakos, K.; Jaksch, S.; Papadakis, C. M., Lamellar Diblock Copolymer Thin Films during Solvent Vapor Annealing Studied by GISAXS: Different Behavior of Parallel and Perpendicular Lamellae. *Macromolecules* **2014,** *47* (16), 5711-5718.
51. Elbs, H.; Krausch, G., Ellipsometric determination of Flory-Huggins interaction parameters in solution. *Polymer* **2004,** *45* (23), 7935-7942.
52. Sólimo, H. N.; Gomez Marigliano, A. C., Excess properties and vapor-liquid equilibrium data for the chloroform + tetrahydrofuran binary system at 30°C. *Journal of Solution Chemistry* **1993,** *22* (10), 951-962.
53. Paik, M. Y.; Bosworth, J. K.; Smilges, D.-M.; Schwartz, E. L.; Andre, X.; Ober, C. K., Reversible Morphology Control in Block Copolymer Films via Solvent Vapor Processing: An in Situ GISAXS Study. *Macromolecules* **2010,** *43* (9), 4253-4260.
54. Zucchi, I. A.; Poliani, E.; Perego, M., Microdomain orientation dependence on thickness in thin films of cylinder-forming PS-b-PMMA. *Nanotechnology* **2010,** *21* (18), 185304.
55. Black, C. T.; Forrey, C.; Yager, K. G., Thickness-dependence of block copolymer coarsening kinetics. *Soft Matter* **2017,** *13* (18), 3275-3283.
56. Pester, C. W.; Schmidt, K.; Ruppel, M.; Schoberth, H. G.; Böker, A., Electric-Field-Induced Order–Order Transition from Hexagonally Perforated Lamellae to Lamellae. *Macromolecules* **2015,** *48* (17), 6206-6213.
57. Jin, H. M.; Lee, S. H.; Kim, J. Y.; Son, S.-W.; Kim, B. H.; Lee, H. K.; Mun, J. H.; Cha, S. K.; Kim, J. S.; Nealey, P. F.; Lee, K. J.; Kim, S. O., Laser Writing Block Copolymer Self-Assembly on Graphene Light-Absorbing Layer. *ACS Nano* **2016,** *10* (3), 3435-3442.
58. Samant, S.; Strzalka, J.; Yager, K. G.; Kisslinger, K.; Grolman, D.; Basutkar, M.; Salunke, N.; Singh, G.; Berry, B.; Karim, A., Ordering Pathway of Block Copolymers under Dynamic Thermal Gradients Studied by in Situ GISAXS. *Macromolecules* **2016,** *49* (22), 8633-8642.
59. Shi, L.-Y.; Lan, J.; Lee, S.; Cheng, L.-C.; Yager, K. G.; Ross, C. A., Vertical Lamellae Formed by Two-Step Annealing of a Rod–Coil Liquid Crystalline Block Copolymer Thin Film. *ACS Nano* **2020,** *14* (4), 4289-4297.
60. Müller-Buschbaum, P., A Basic Introduction to Grazing Incidence Small-Angle X-Ray Scattering. In *Applications of Synchrotron Light to Scattering and Diffraction in Materials and Life Sciences*, Gomez, M.; Nogales, A.; Garcia-Gutierrez, M. C.; Ezquerra, T. A., Eds. Springer Berlin Heidelberg: Berlin, Heidelberg, 2009; pp 61-89.
61. Cummins, C.; Gangnaik, A.; Kelly, R. A.; Borah, D.; O'Connell, J.; Petkov, N.; Georgiev, Y. M.; Holmes, J. D.; Morris, M. A., Aligned silicon nanofins via the

directed self-assembly of PS-b-P4VP block copolymer and metal oxide enhanced pattern transfer. *Nanoscale* **2015,** *7* (15), 6712-6721.
62. Cummins, C.; Gangnaik, A.; Kelly, R. A.; Hydes, A. J.; O'Connell, J.; Petkov, N.; Georgiev, Y. M.; Borah, D.; Holmes, J. D.; Morris, M. A., Parallel Arrays of Sub-10 nm Aligned Germanium Nanofins from an In Situ Metal Oxide Hardmask using Directed Self-Assembly of Block Copolymers. *Chemistry of Materials* **2015,** *27* (17), 6091-6096.
63. Khorasaninejad, M.; Abedzadeh, N.; Walia, J.; Patchett, S.; Saini, S. S., Color Matrix Refractive Index Sensors Using Coupled Vertical Silicon Nanowire Arrays. *Nano Letters* **2012,** *12* (8), 4228-4234.
64. Walia, J.; Dhindsa, N.; Khorasaninejad, M.; Saini, S. S., Color Generation and Refractive Index Sensing Using Diffraction from 2D Silicon Nanowire Arrays. *Small* **2014,** *10* (1), 144-151.

2.7. Chapter 2 Appendix

S2.7.1. Estimation of the partial pressures of THF:chloroform mixtures inside the SVA chamber:

In order to fully optimize the SVA process of our UHMW system, it was essential to deduce the optimal choice of solvent to obtain phase separation into lamellar domains. The primary solvents investigated were chloroform and THF, due to their relative neutrality towards both PS and P2VP domains. In an ideal solvent mixture, the vapour pressures of each solvent would exactly match the concentration of the solvent in the liquid mixture as per Raoult's law. Chloroform/THF mixtures are non-ideal, however, and therefore the activity coefficient (γ) of a solvent in a binary mixture must be considered in order to calculate the partial pressure:

$$p_i = \gamma_i \, x_i \, p_{i,sat} \tag{1}$$

Where x_i is the molar fraction of solvent i in the liquid phase, and $p_{i,sat}$ is the saturated vapour pressure of the pure solvent i. $p_{i,sat}$ can be estimated from the Antoine equation:

$$\log(p_{i,sat}) = A_i - \frac{B_i}{C_i + T} \tag{2}$$

Where A_i, B_i and C_i are the component-specific constants, and T is the temperature. The values of these constants for chloroform at 21°C are $A = 6.995, B = 1202.29, C = 226.25$, and for chloroform are $A = 6.955, B = 1170.97, C = 226.232$ [2, 3]. The molar ratio of both solvents in the gas form (y) can be calculated using the following expression:

$$y_i = \frac{p_i}{p_{total}} \tag{3}$$

Where p_{total} is the total pressure of the solvent mixture. The behaviour of chloroform and THF in a binary mixture has been studied in past work. At temperatures of between 20-30°C it has been found that the mixture displays a negative deviation from ideality, meaning that the total pressure of the mixture passes through a minimum value as the composition of the mixture is changed [4, 5].

To analyse the effect of x_i on the phase separation, the values of γ_i for each molar ratio of solvent examined were required. Previous experimental work on chloroform/THF

binary mixtures determined that an athermal model based on Flory-Huggins theory can accurately predict the values of γ_i obtained from experimental results.[1, 6] The values of γ_i from this model for both chloroform and THF were used to determine the partial pressures of both solvents in the vapour phase during annealing (see **Figure S2.7.1**). Various ratios of both solvents were added to the solvent bubbler and used to swell the block copolymer films to a constant ϕ_s value of ~0.83. All other parameters, including swelling rate, initial stage temperature, and swelling time, were held constant.

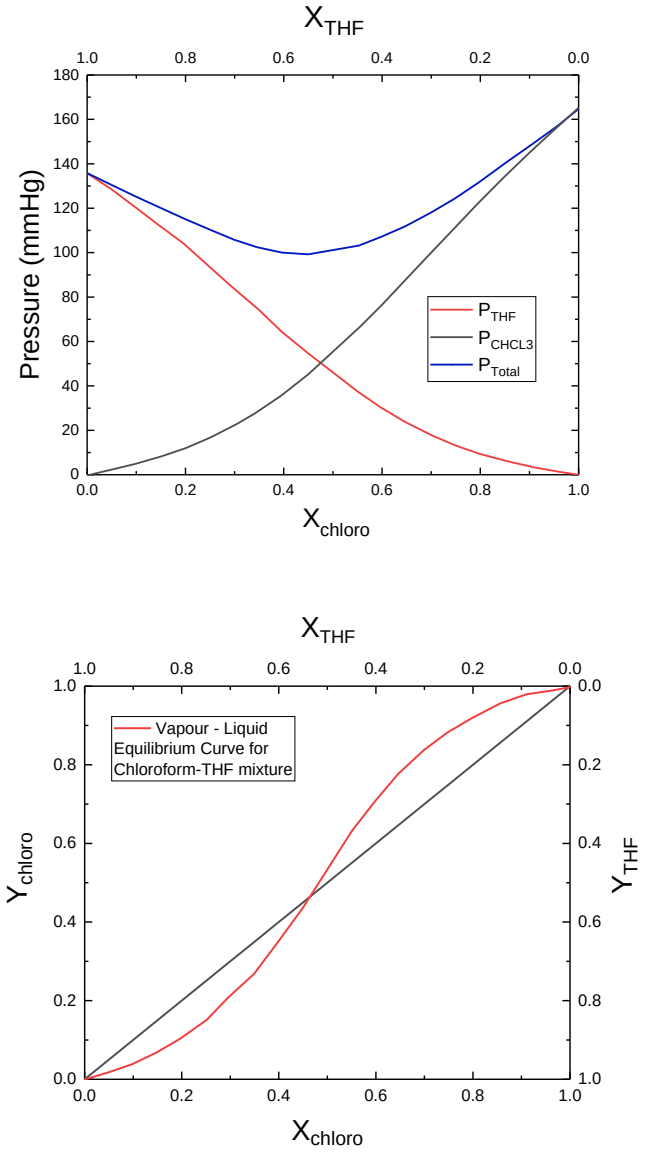

Figure S2.7.1: (a) Graph of the vapour pressures of chloroform (P_{CHCl_3}), THF (P_{THF}), and the total equilibrium vapour pressure P_{total} vs. the concentration of chloroform in solution (x_{CHCl_3}) at 294.15K. Data for the values of the activity coefficients γ_i were obtained from *Dohnal* et al.[1]
(b) Vapour liquid equilibrium curve of the THF-chloroform mixture.

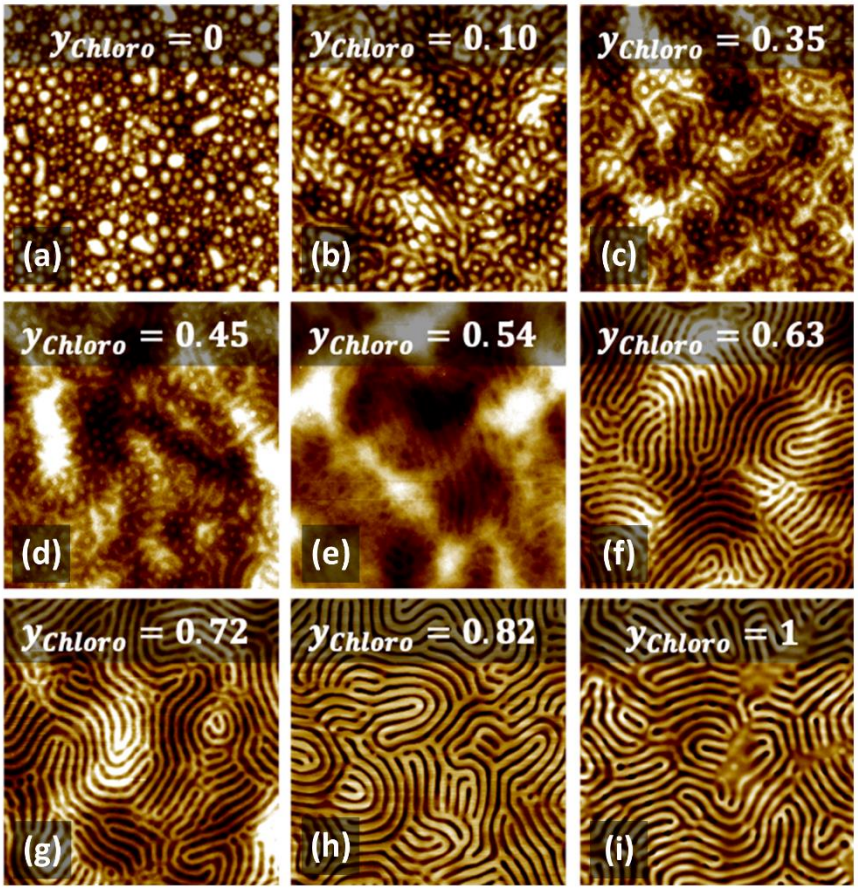

Figure S2.7.2: AFM images (5 × 5 μm) of PS-b-P2VP films annealed in the rig for 200s to a ϕ_s value of ~0.83 using a variety of chloroform/THF ratios. The calculated molar fraction of chloroform y_{CHCl_3} in the vapour phase is shown inset for each image.

Figure S2.7.2 shows AFM images of the BCP films after 200s of swelling to a ϕ_s value of ~0.83, with bubbler temperature of 21C. In the case of pure THF, the film appeared to remain in the original 'as cast' micellar form after SVA. A similar structure is observed when $y_{CHCl_3} = 0.1$, which progresses to a partially phase-separated structure at $y_{CHCl_3} = 0.54$, and eventually to the expected lamellar structure as the chloroform becomes the majority component.

Although the lamellar form was observed using pure chloroform, the solvent mixture that gives $y_{CHCl_3} = 0.82$ was utilised for the kinetic studies outlined in the main text. This is because despite multiple attempts of swelling to high ϕ_s values using pure chloroform, the resulting lamellar structure was observed to contain nano-scale regions of non-uniformity where the ordering was lost, as can be seen in (g). We suggest that this may

be the result of increased difficulty in maintaining a constant swelling profile across the film due to the ~20% higher overall equilibrium vapour pressure of pure chloroform vs. the solvent mixture with $y_{CHCl_3} = 0.82$ at 21°C (calculated from figure 2 values). This is an interesting observation in itself, as it suggests that negative azeotropic solvent mixtures may be better suited for maintaining thickness control at high degrees of swelling where the swollen film thickness becomes increasingly sensitive to temperature changes. A more in-depth examination of the effect of solvent mixtures on film swelling kinetics will be the subject of a future study.

S3.7.2. Calculation of Refractive Index of Swollen Film:

The refractive index values of the solvent mixture, pure BCP film, and swollen BCP film were estimated from their known pure component values (see table 1) using the Lorenz-Lorentz rule of mixing[7].

$$\frac{n_{12}^2 - 1}{n_{12}^2 + 2} = \phi_1 \frac{n_1^2 - 1}{n_1^2 + 2} + \phi_2 \frac{n_2^2 - 1}{n_2^2 + 2} \tag{4}$$

Where ϕ_1, ϕ_2 and n_1, n_2 are the volume fractions and refractive indices of pure components 1 and 2, and n_{12} is the refractive index of the resulting mixture.

Component	Refractive index value:
Tetrahydrofuran[8]	1.405 ± 0.001
Chloroform[9]	1.446 ± 0.001
Polystyrene[10]	1.587 ± 0.001
2-vinylpyridine[11]	1.550 ± 0.001

For the molecular weight of PS-*b*-P2VP used in this work, a refractive index value of 1.570 was obtained using the respective volume fractions of each block. For the chloroform/THF mixture, an approximation was made that the ratio of each solvent absorbed into the film during swelling is equal to the solvent ratio in the vapour phase. This yields a value of 1.438 using eq. (4) for $y_{CHCl_3} = 0.82$. For the swollen film, refractive index values of between 1.503 and 1.453 were obtained for ϕ_s values between

0.5 to 0.88 respectively via incorporating the refractive indices of the both the solvent mixture and block copolymer film.

During a swelling experiment, the refractive index was initially set at a precalculated profile corresponding to the dry film (n=1.438, **figure S2.7.3a**). Once swelling was induced, the precalculated refractive index profile was switched (within the Filmetrics software) to the corresponding index profile of the desired solvent concentration of the swollen film for that experiment (examples in **figure S2.7.3(b, c)**). Upon initiation of deswelling, the refractive index profile was immediately reverted back to that of the dry film. This ensured that our reflectometer model aligned with the measured BCP film during the experiment. We intend to automate such refractive index changes in our future studies via a feedback loop system in order to further enhance the scalability and precision of the technique

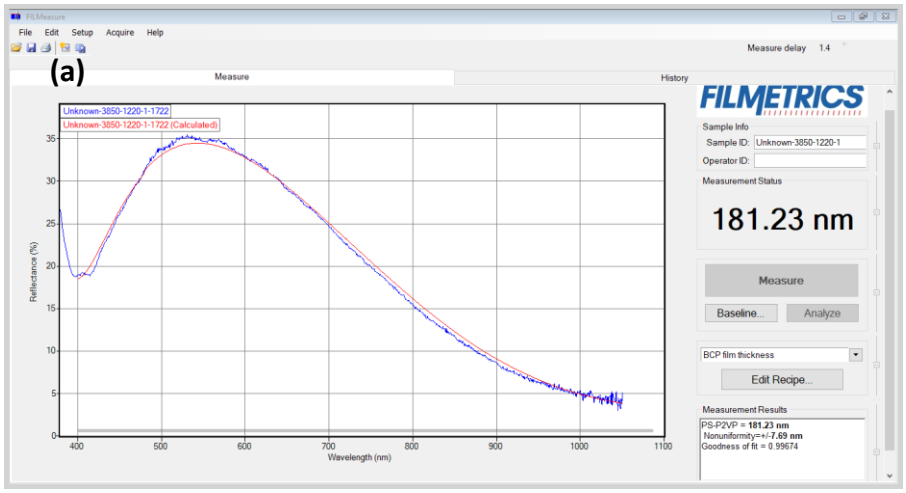

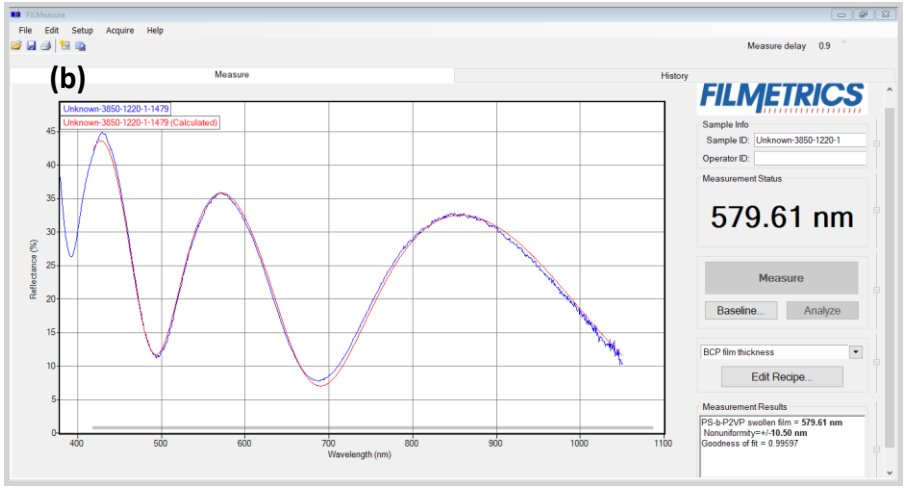

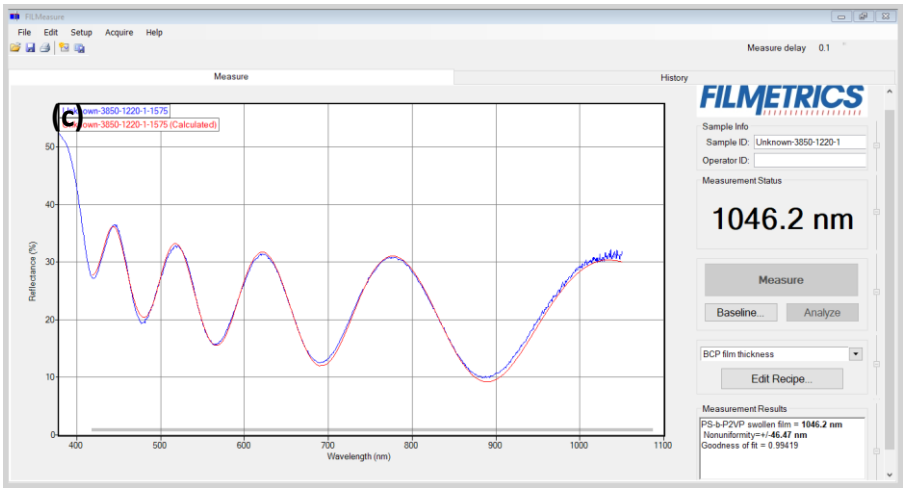

Figure S2.7.3. Spectral reflectance of the unswollen neat BCP film (a), the film swollen to a ϕ_s value of ~0.69 (b), and swollen to a ϕ_s value of ~0.83 (c).

S2.7.3. Additional Swelling Plots

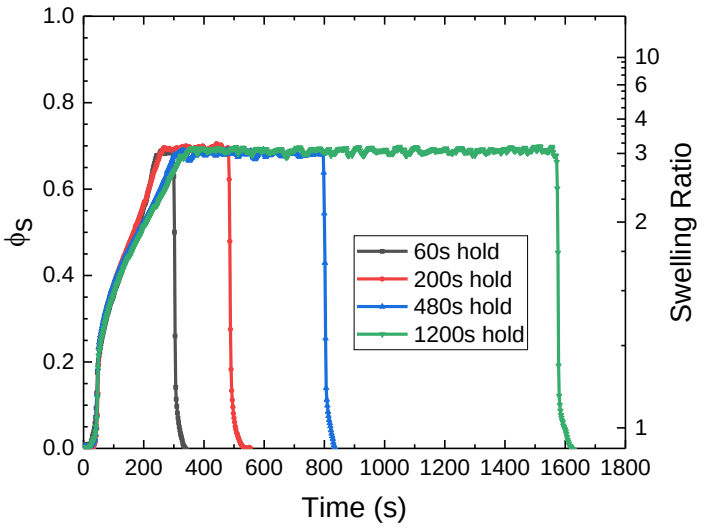

Figure S2.7.4. Swelling plot of the films shown in figure 5 (a) to (e) of the main text.

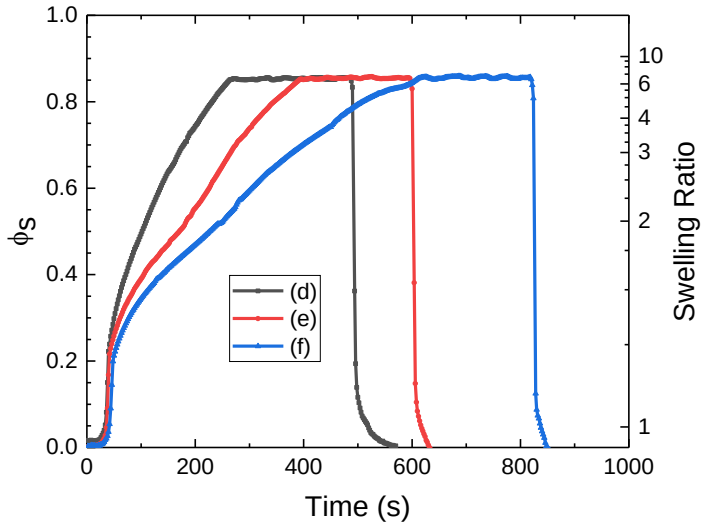

Figure S2.7.5. Swelling plot of the films shown in figure 6 (d) to (f) of the main text.

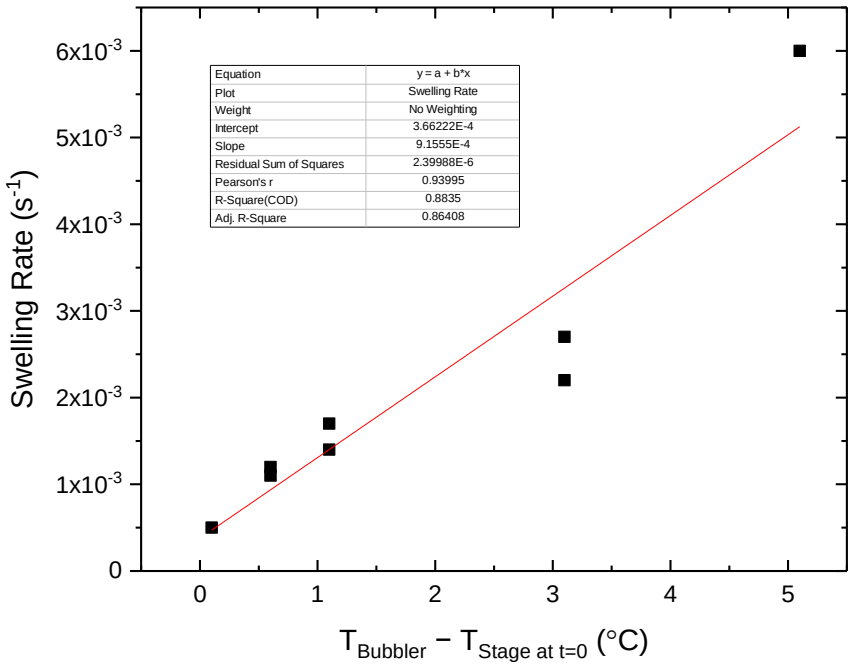

Figure S2.7.6. Plot of the calculated swelling rate vs. the difference between the initial stage temperature (varied between $15.9°C$ to $20.9°C$) and bubbler temperature (21°C for all samples).

Section S2.7.4. Additional AFM, SEM data:

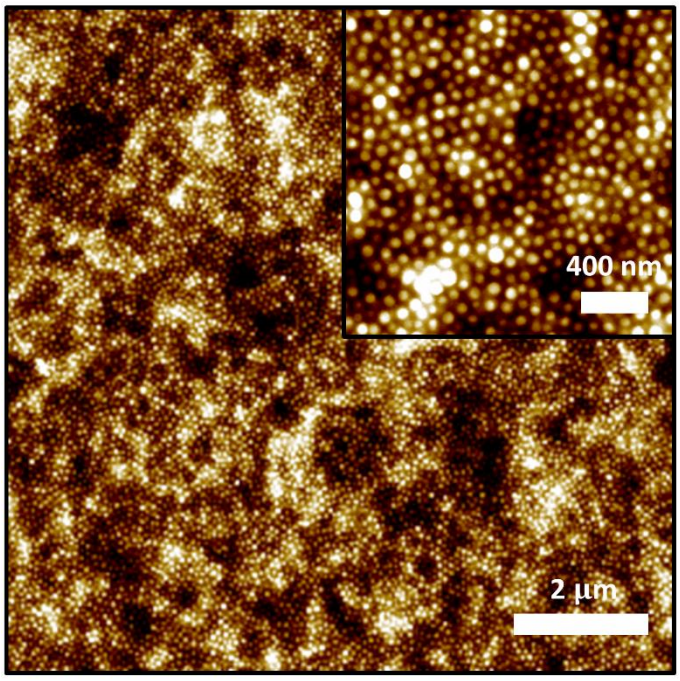

Figure S2.7.7. AFM image of the as cast PS-*b*-P2VP film.

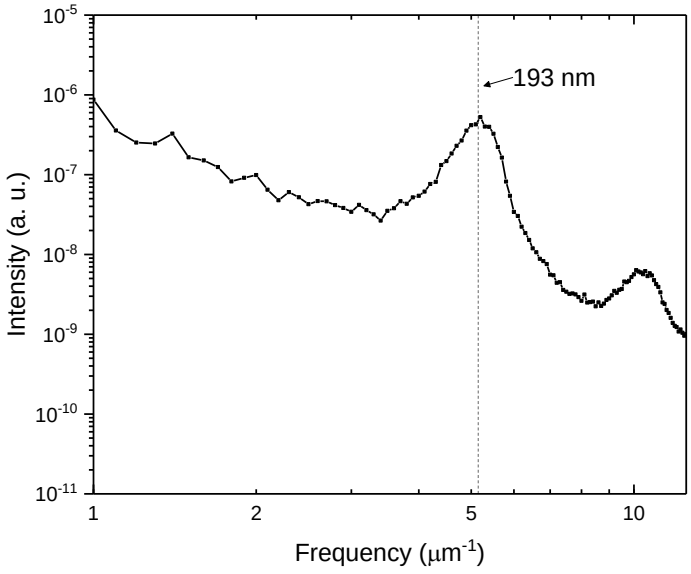

Fig. S2.7.8. 2-dimensional power spectral density (PSD) plot of an AFM image of the BCP film shown in sample 2 (n). The peak corresponding to the feature spacing of 193 nm is marked, and was determined using a Gaussian fit.

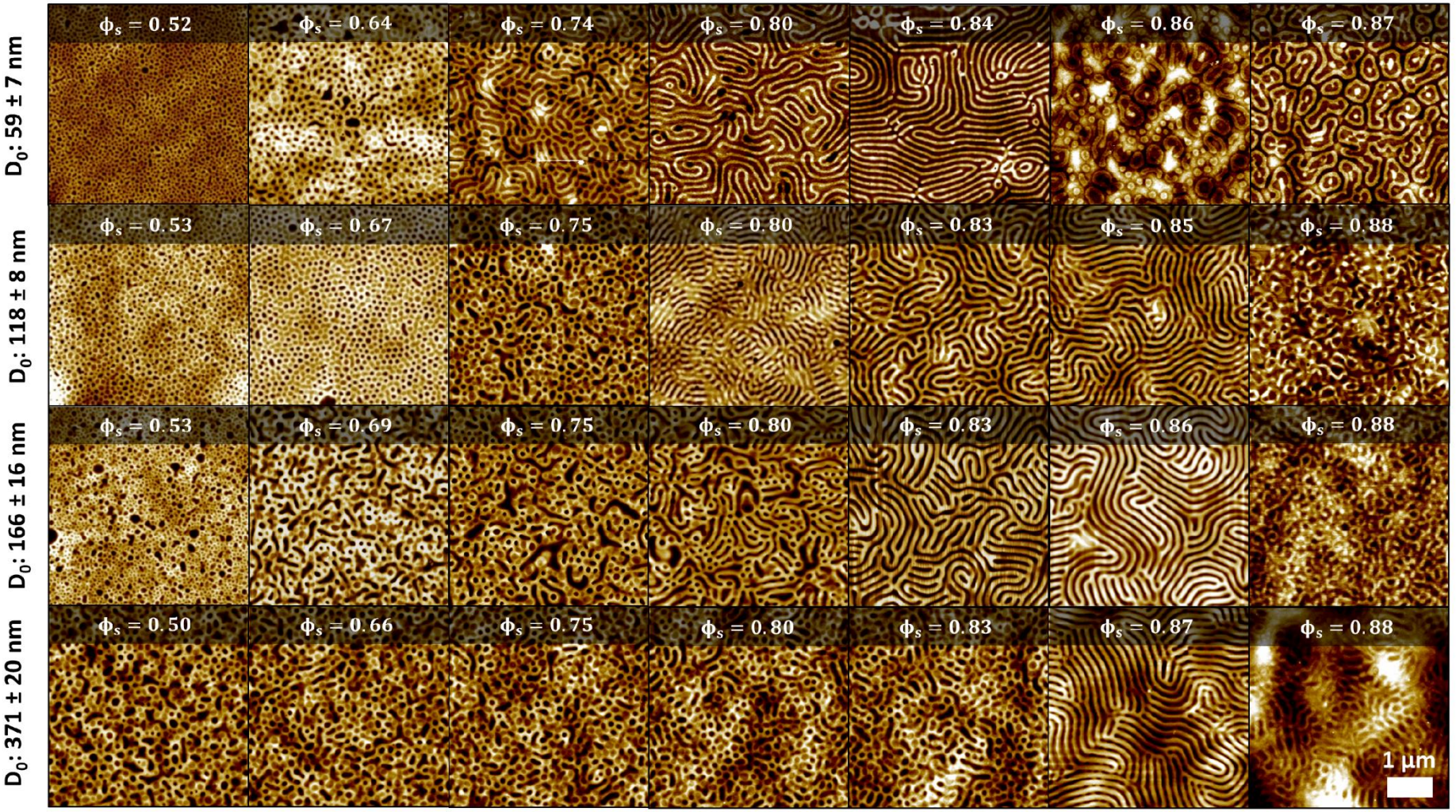

Figure S2.7.9.: AFM images of the PS-*b*-P2VP films as a function of the solvent concentration in swollen film ϕ_s, and initial film thickness D_0. These images were used to construct the orientation diagram shown in fig. 2 in the main text.

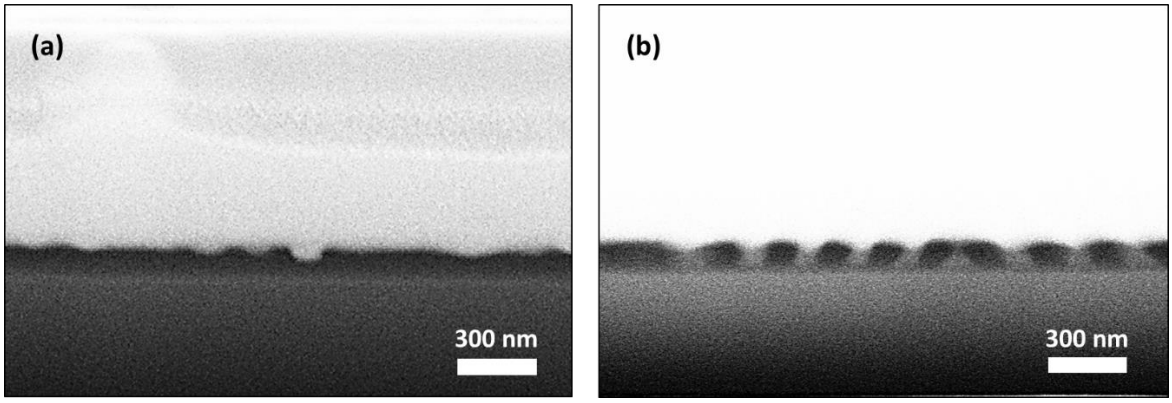

Figure S2.7.10.: FIB/SEM images of 166 nm thick PS-*b*-P2VP films after a total annealing time of 10 mins at a ϕ_s value of (a) 0.67 and (b) 0.86.

S2.7.5. Optical Micrographs of BCP films Post SVA

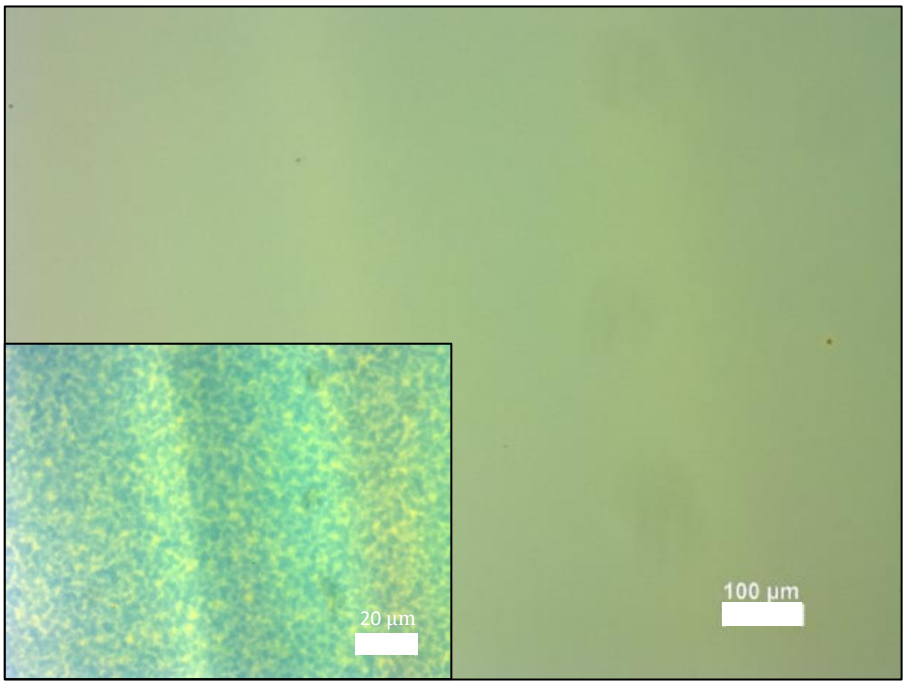

Figure S2.7.11. Optical microscopy images of the PS-*b*-P2VP film after a total annealing time of 10 mins at a ϕ_s value of 0.86 (giving lamellar orientation). Image is taken after SVA with no surface reconstruction.

S2.7.6: Correlation Length example:

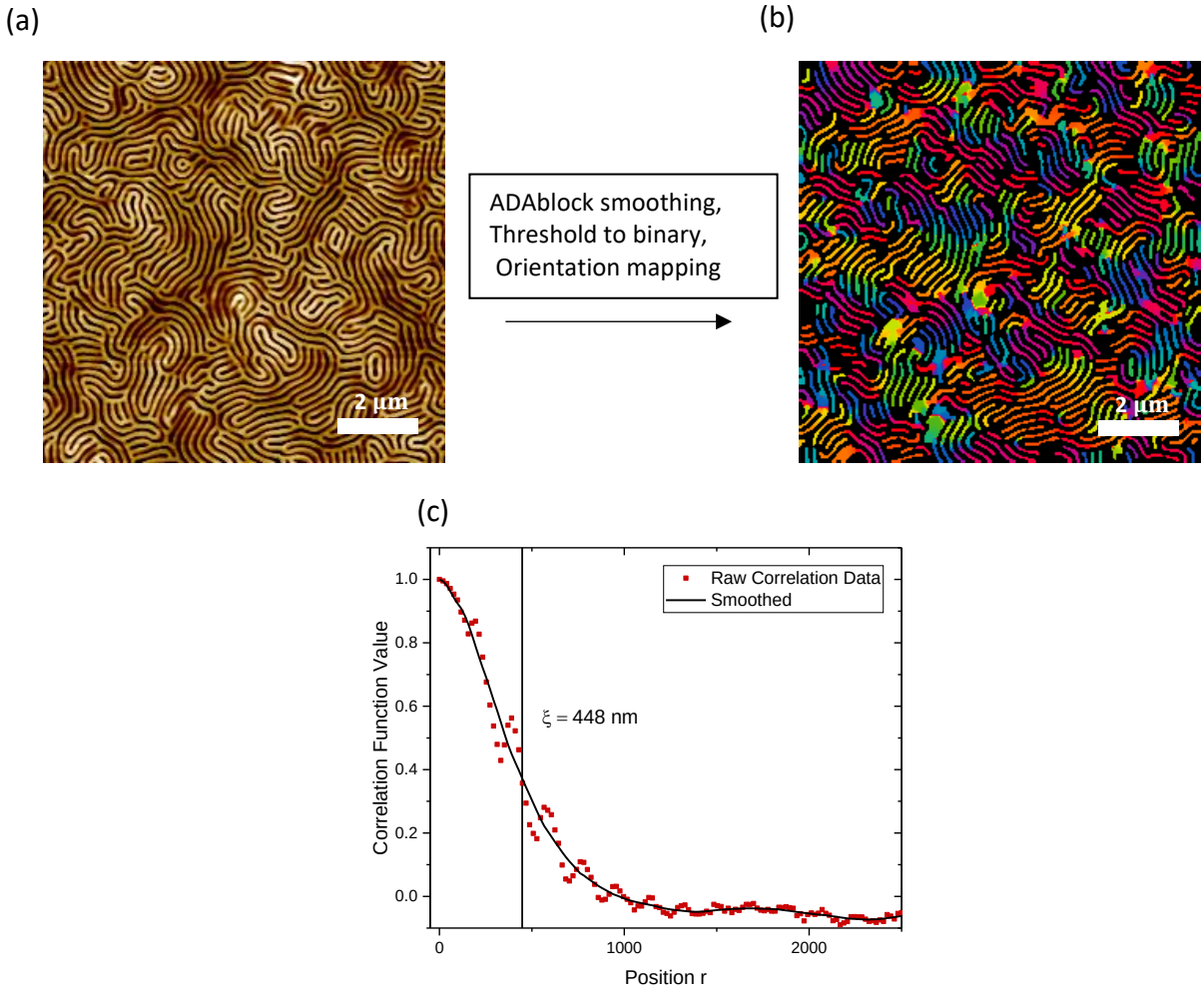

Figure S2.7.12. (a) Example $10 \times 10\ \mu m$ AFM image (from film shown in figure 6 (d) of main text). (b) Generated orientational map of skeletonized AFM image as generated from the ADAblock application.[12] (c) Calculation of correlation function from AFM image. Raw data is shown in red with smoothed data in black. Correlation length is marked at the r value where the correlation function is equal to $1/e$

S2.7.7. Feature height variation with etch time:

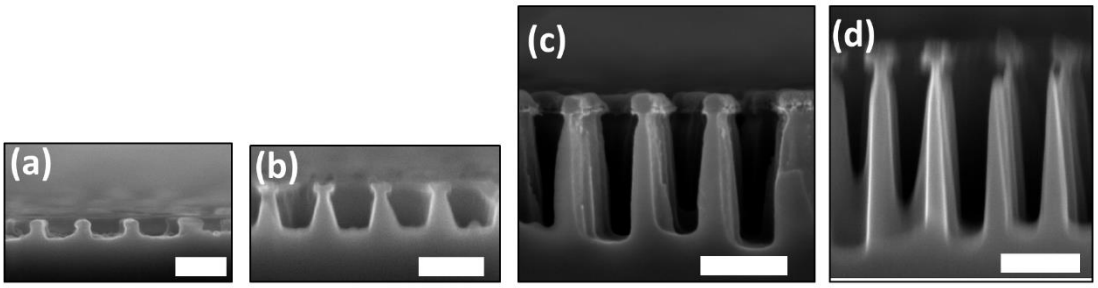

Etch time (s)	30	60	120	180
Height (nm)	78	145	373	493

Figure S2.7.13. High resolution cross-sectional SEM images of Si nanowalls, after (a) 30 seconds, (b) 60 seconds, (c) 120 seconds, and (c) 180 seconds of etch time. The table shows the variation of feature heights with etching time. All scale bars are 200 nm.

S2.7.8. Appendix Bibliography:

1. Dohnal, V.; Costas, M., Thermodynamics of complex formation in chloroform-oxygenated solvent mixtures. *Journal of Solution Chemistry* **1996,** *25* (7), 635-656.
2. Smallwood, I., *Handbook of Organic Solvent Properties*. Elsevier: Oxford, 1996.
3. Stull, D. R., Vapor Pressure of Pure Substances. Organic and Inorganic Compounds. *Industrial & Engineering Chemistry* **1947,** *39* (4), 517-540.
4. Oswal S.L., D., D. D, Excess Free Energies & Excess Volumes for Chloroform + Tetrahydrofuran Systems. *Indian Journal of Chemistry -Section A* **1978,** *16*, 798-800.
5. Byer, S. M.; Gibbs, R. E.; Van Ness, H. C., Vapor-liquid equilibrium: Part II. Correlations from P-x data for 15 systems. *AIChE Journal* **1973,** *19* (2), 245-251.
6. Dohnal, V.; Fenclová, D.; Bureš, M.; Costas, M., Thermodynamic study of complex formation by hydrogen bonding in halogenoalkane–oxygenated solvent mixtures: halothane with acetone, methyl acetate, tetrahydrofuran and methyl tert-butyl ether. *Journal of the Chemical Society, Faraday Transactions* **1993,** *89* (7), 1025-1033.
7. Heller, W., Remarks on Refractive Index Mixture Rules. *The Journal of Physical Chemistry* **1965,** *69* (4), 1123-1129.
8. Lide, D. R., *CRC Handbook of Chemistry and Physics, 88th Edition.* CRC Press Inc.: Boca Raton, Florida, 2008.
9. Haynes, W. M., *CRC Handbook of Chemistry and Physics, 95th Edition*. CRC Press Inc.: Hoboken, 2014.
10. Sultanova, N. G.; Kasarova, S. N.; Nikolov, I. D., Dispersion Properties of Optical Polymers. *ACTA PHYSICA POLONICA A* **2009,** *116*, 585-587.
11. Weast, R. C., *CRC Handbook of Chemistry and Physics, 60th Edition.* CRC Press Inc.: Boca Raton, Florida, 1979.
12. Murphy, J. N.; Harris, K. D.; Buriak, J. M., Automated Defect and Correlation Length Analysis of Block Copolymer Thin Film Nanopatterns. *PLOS ONE* **2015,** *10* (7), e0133088.

Chapter 3: Large Period 3-Dimensional Metallic Lamellae with Tailored Thickness via Liquid Phase Infiltration of a Block Copolymer Film

3.1. Abstract

In this work, we describe a scalable, facile strategy for the fabrication of freestanding, 3D metal lamellae via liquid phase infiltration (LPI) of an ultrahigh molecular weight block copolymer (BCP) system (PS-*b*-P2VP). Microphase separation is achieved using solvent vapour annealing (SVA), yielding large period lamellar structures with a range of film thicknesses. LPI is performed by immersing the BCP films in heated solutions of Au or Pt precursors, which were subsequently reduced to metal structures using oxygen plasma treatment followed by thermal annealing. The thickness of the BCP film was found to strongly correlate with the height of the metal features. The Au samples were found to consist of an array of different particle sizes, whereas the Pt features showed a greater degree of structural uniformity. The Au structures were employed as photocatalysts for the degradation of methyl orange (MO), demonstrating an association between the photocatalytic performance and the height of the metal features. Furthermore, the structures were shown to be reusable over multiple degradation runs.

3.2. Introduction:

The fabrication of nanostructures via block copolymer (BCP) self-assembly is a well-studied technique, with many potential applications owing to the low cost, scalability, and high degree of dimensional control.[1, 2] The morphology of the micro-phase separated structure depends on a number of factors, which include the degree of polymerization, the volume fraction of each block, and the Flory-Huggins interaction parameter.[3] Many of the applications of BCP systems are dependent on their ability to coordinate with metal precursors; this enables the polymeric material to act as a scaffold for the formation of a wide range of periodic metal or metal oxide structures. Such applications include photonics,[4, 5] catalytic materials,[6, 7] metal nanopatterning,[8-11] antimicrobial surfaces,[12]

among others.[13-15] The coordination ability of a particular species of BCP depends on the specific block chemistry, with some commonly utilised systems including polystyrene-block-poly(methyl methacrylate) (PS-b-PMMA),[16-18] polystyrene-block-poly(ethylene oxide) (PS-b-PEO),[19, 20] and polystyrene-block-poly(x-vinylpyridine) (PS-b-PxVP, where x = 2 or 4). [21-24]

There are a variety of techniques that can be used to incorporate the metal species into the polymer domains – these include both vapour phase infiltration (VPI) and liquid phase infiltration (LPI) strategies. The relative success of these strategies is dependent on two primary factors: firstly, the diffusion of the precursor throughout the polymer matrix, and secondly, the coordination strength between the precursor and the reactive site within the polymer.[25, 26] For VPI processes (also commonly referred to as sequential infiltration synthesis (SIS)), recent studies have ascertained a number of crucial variables that must be optimised in order to achieve maximum precursor absorption; these include the process temperature and pressure, the number of exposure cycles, and the chemical behaviour of the precursor.[25, 27-29] In spite of these recent increases in understanding, there exists a number of limitations to the continued adoption of VPI processes. Firstly, the range of gaseous precursors remains small, owing to the general weakness of the binding between the precursors and the reactive sites in the polymer. This often necessitates the use of pre-treating steps to encourage greater uptake and metal ion coordination.[18] Secondly, in addition to their high cost, the processing of vapour phase precursors often requires highly controlled conditions with complex setups due to safety and toxicity concerns.[30]

LPI processes, in contrast, can often be conducted using a much wider range of precursor materials and under more simplistic conditions. They involve the dissolution of a metal salt in a solvent (ethanol and water are most common), which is then either spin-coated onto the polymer film or used as an immersion medium.[22, 24, 31] The LPI of inorganic precursors into BCP films depends on a two main factors – firstly, the diffusion of the precursor species into the polymer domains, and secondly, the binding interaction between the precursor and the reactive sites within the polymer. In the case of BCP systems containing PxVP blocks, the nitrogen located on the pyridine group enables the formation of coordinate bonds with ionic precursors. In the case of LPI involving anionic metal precursors (such as $AuCL_4^-$ from chloroauric acid ($HAuCL_4$) for Au infiltration),

the mechanism behind the ionic coordination is theorised to be due to the protonation of the pyridine groups in the presence of an acidic metal salt solution – the pyridine groups act as Lewis bases and bind with H^+ ions to form pyridinium ions. The negatively charged metal species present in the solution can then electrostatically bind to the pyridinium ions through the donation of a lone pair to the metal species, hence enabling the selective metal uptake into the PVP domains.[32] The pioneering studies that utilised this strategy were by Buriak et al., which reported the formation of a range of metal nanostructures (Au, Pt, Fe, Cu, Ni, Co) via immersion of a self-assembled PS-b-P2VP film in aqueous solutions of metal salts.[11, 32] Subsequent work has focused on expanding the range of LPI precursors, along with optimising the immersion conditions to achieve maximum precursor uptake.[22, 31]

While the majority of BCP-based infiltration studies have focused on the fabrication of 2-dimensional surface arrangements of metal/metal oxide structures, a number of recent publications have given attention to expanding the growth of these structures in the vertical direction.[33, 34] Owing to their increased surface area, these 3-dimensional structures have unique potential applications, including catalytic structures, plasmonics, multi-layered metallised structures for transistors, and membranes.[34-36] 3D structures can be synthesized via multiple stacking of BCP layers using 2D assembly, however this method can prove time-consuming and requires a high degree of accuracy and control to achieve multiple layer alignment.[37, 38] Alternatively, a thick BCP film (with a thickness exceeding that of the domain period) may be deposited, which, when immersed in a suitable metal salt solution, can yield thick 3D metal nanostructures. For example, Lee et al. successfully synthesized and examined the chemical nature of 3D Pt structures fabricated via LPI of self-assembled PS-b-P2VP BCP films (with thicknesses exceeding 100 nm).[39] Lee et al. used a P2VP-b-P4VP BCP system for creating 3D metallic structures, where they propose that the increased steric hindrance of the P2VP vs the P4VP chains results in greater precursor uptake into the P4VP domains – hence enabling the creation of nanoporous Au, Pt, and bimetallic PtCo films.[34]

Despite these recent advances, there is still a lack of understanding of how to effectively optimise the formation of 3D structures via LPI. For example, the synthesis of ‘standalone’ 3D lamellar structures via LPI has not been extensively explored, most likely due to the height limitations that small period features would incur. Moreover, the

photocatalytic properties of BCP templated 3D metallic structures remain largely unexamined. Hence in this work, we demonstrate the fabrication of large period, 3D Au and Pt nanowalls via LPI of an UHMW PS-b-P2VP BCP system. The BCP films are self-assembled into lamellar domains using a single-layer process, enabling the formation of standalone metallic structures with thicknesses exceeding 200 nm on Si substrates. The relationship between the height of the metallic structures and the film thickness is examined, as well as the resulting influence of feature height on the photocatalytic properties of the material.

3.3. Experimental Method:

3.2.1. Materials: Polystyrene-b-poly(2-vinylpyrridine) with a molecular weight of 440-b-353 kg mol^{-1} was purchased from Polymer Source^{TM} and used as received. Toluene (99.8%, anhydrous), tetrahydrofuran (99.8%, anhydrous), and chloroform (99.8%, anhydrous), all HPLC grade, were purchased from Sigma-Aldrich. Gold (III) tetrahydrate ($HAuCl_4$) and sodium tetrachloroplatinate (II) were purchased from Sigma-Aldrich and used as received. Methyl orange dye (MO) was purchased from Fluorochem (Lot:FCB006592) and used as received.

3.2.2. Au, Pt 3D nanostructure preparation: PS-b-P2VP was dissolved in varying amounts in a 4:1 mixture of toluene and THF to give 1%, 1.5%, 2% and 3% w/w solutions. These solutions were left to stir overnight to ensure complete dissolution of the polymer material. 2×2 cm^2 pieces of p-type Si <100> wafers with a native oxide layer were cleaned via ultrasonication in acetone for 20 minutes, followed by drying under N_2 stream. The BCP solutions were then spin-coated onto the Si substrates at a speed of 4500 rpm for 30 seconds. The BCP films were annealed using a 2:1 mixture of chloroform and THF in a custom-built chamber, which controllably swelled the BCP films to a solvent concentration of 0.84-0.86 forming lamellar patterns. Details of the SVA process, including the chamber design, are described extensively in **chapter 2**. The micro-phase separated films were then immersed in 20 mM aqueous solutions of the desired metal precursor at a temperature of 60 °C for 30 minutes. The films were then briefly washed with deionised water to remove excess metal salt and dried under N_2. In order to synthesize the metal structures, the metal infiltrated BCP films were etched using an O_2 plasma to remove the polymeric material and reduce the metal species to Au and Pt.

Finally, in order to further densify the inorganic material and remove excess carbon impurities, the films were placed on a hot plate at a temperature of 270 C for 30 minutes in air.

3.2.3. MO Photocatalytic degradation: An aqueous solution of MO at a concentration of 0.25 mmol mL^{-1} was prepared with deionised water, which was allowed to stir for approx. 30 minutes prior to use. There was no agglomeration or particulate formation in the solution, exhibiting good homogeneity in the solution. 1×1 cm cuts of the nanostructured Au samples were then immersed in 3 mL volumes of the MO solution for various times. The samples were irradiated under UV lamp (15 W, 353 nm) for different time durations (0-15 h). The degradation of the dye was examined by measuring the decrease in MO absorption.

3.2.4. Sample characterisation: Atomic force microscopy (AFM) measurements were performed using a Park Systems XE7 system in non-contact mode with silicon cantilevers (PPP-NCHR, Nanosensors, USA) possessing a force constant of 42 N m^{-1}. Scanning electron microscopy (SEM) measurements were performed using a Carl Zeiss Ultra plus with an InLens detector. For cross-sectional images, the samples were mounted on 90 degree sample holders with the stage tilted to the preferred angle of 20°. X-ray photoelectron spectroscopy (XPS) was performed on a VG Scientific ECSAlab Mk II system using Al Kα X-rays (1486.6 eV). The analyser pass energy was set to 20 eV for the high-resolution core scans. Photoemission peak positions were corrected with respect to C 1s (284.8 eV). The absorption measurements of the MO solutions were conducted using a PerkinElmer LAMBDA 1050 UV–Vis–NIR spectrophotometer and a Cary 50 scan spectrophotometer. Absorption data was measured over a wavelength range of 250-700 nm, using steps of 3 nm and an integration time of 0.7 s. A reference measurement of DI water was also taken to subtract from the MO data. Reflectivity measurements were taken with a Filmetrics F20 reflectometer system and the LAMBDA 1050 fitted with an integrating sphere, for specular and total reflectivity, respectively.

3.4. Results:

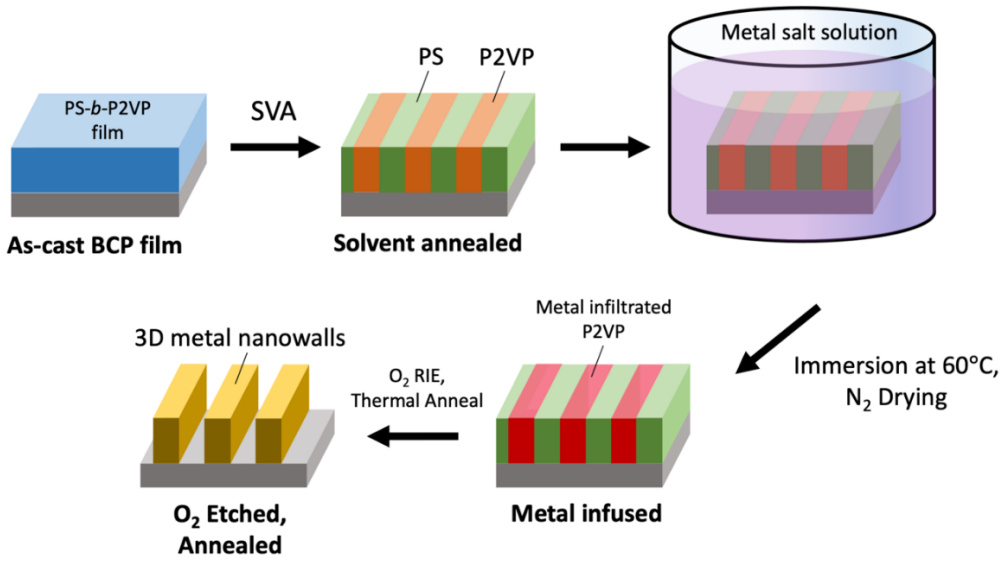

Fig. 3.1: Schematic representation of the 3D metal nanostructure fabrication process.

A PS-*b*-P2VP BCP system with a molecular weight of 440-b-353 kg mol^{-1} was utilised for this study, as this system was previously shown to produce vertical lamellar structures upon SVA. The microphase separated BCP films were produced by spin-coating different weight percentages of a BCP solution onto Si substrates, followed by a SVA treatment for approximately 10 minutes in chloroform + THF vapour. A schematic of the complete fabrication process is shown in **figure 3.1**. In order to initiate microphase separation, it was necessary to swell these films to a solvent concentration value of between 0.84-0.87 due to the extremely long chain lengths associated with this BCP system. The thickness of the resulting films varied from ~60 nm for the 1% solution, up to ~370 nm for the 3% solution.

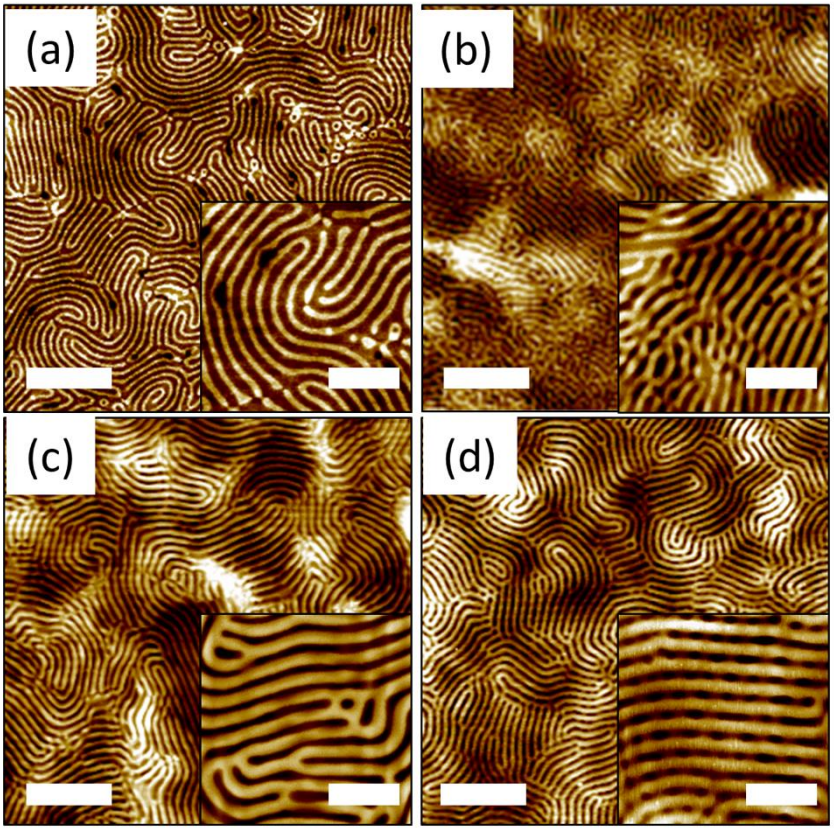

Fig. 3.2: AFM images of the microphase separated BCP films after SVA. (a) to (d) show the films cast from 1, 1.5, 2 and 3 % solutions respectively. Scale bars for the larger images are 2 μm, whereas the inset scale bars are 400 nm.

AFM images of the films are shown in **figure 3.2**. Although all 4 thicknesses resulted in vertical lamellar films, it can be seen that the 1.5% solution is somewhat less ordered in comparison to the others. This may be due to commensurability effects that occur when the film thickness drops below the domain spacing, which can lead to deviations from the expected bulk morphology.[40] The films were then immersed in solutions of either $HAuCl_4$ or Na_2PtCl_4, which were held at a temperature of 60 °C. The solution was heated as previous studies have noted that this can significantly improve precursor uptake, in comparison to immersions conducted at room temperature.[24] Following the immersion step, the polymer matrix was removed using O_2 plasma and the samples were heated in air to 270 °C on a hot plate. The heating step was essential in order to remove any excess carbon impurities and to densify the metal structures.

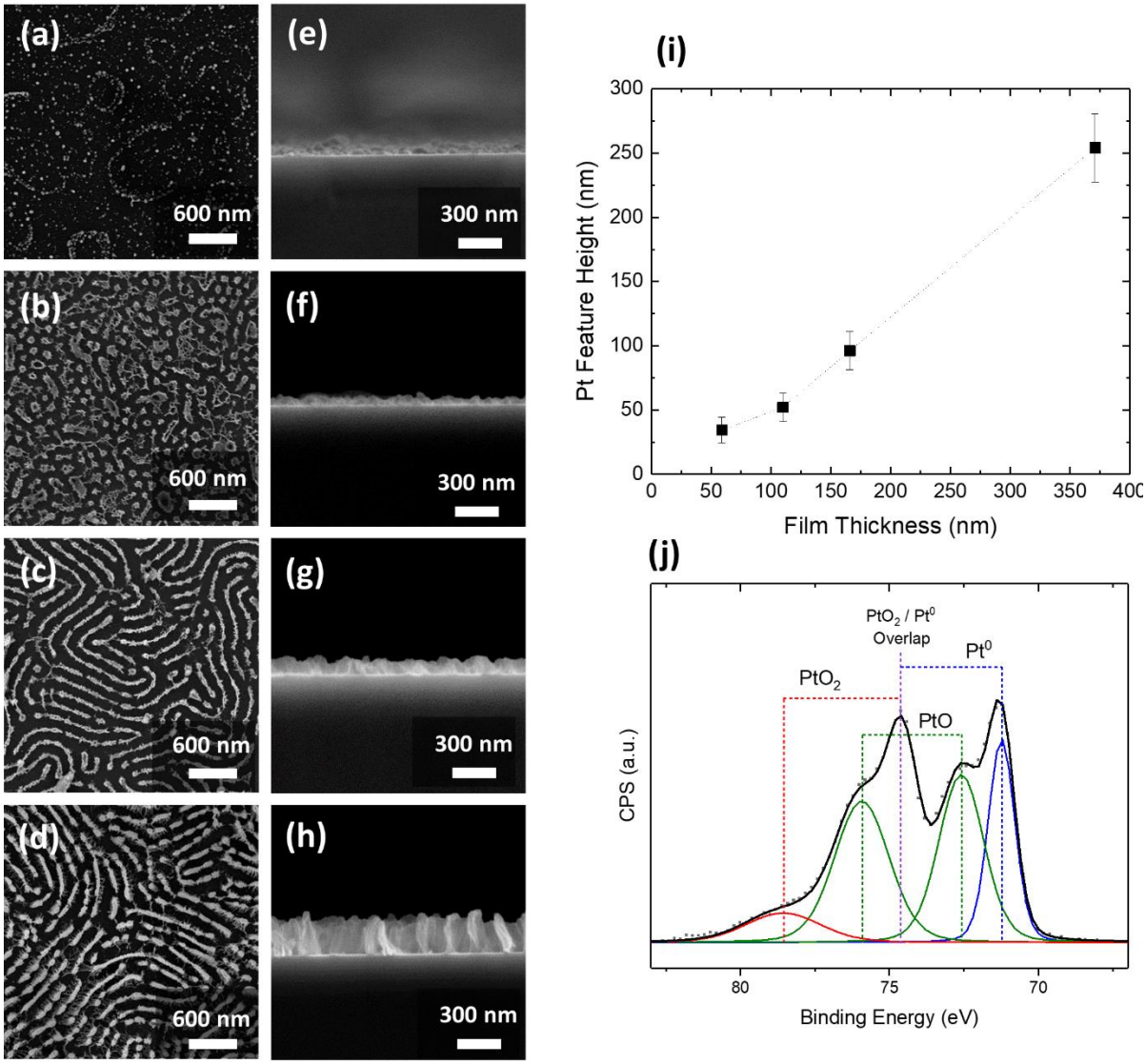

Fig. 3.3: (a) – (d) Top down SEM images of the Pt nanostructures after plasma etching and thermal annealing, templated from 1, 1.5, 2 and 3 % BCP solutions respectively. (e) – (f) Corresponding cross-sectional SEM images. (i) Plot of the Pt nanostructure height vs the thickness of the BCP template. (j) High-resolution XPS spectrum of the Pt 4f region.

Top-down SEM images of the resulting Pt features are shown in **figure 3.3(a-d)**. It can be seen that at lower BCP film thicknesses (for 1, 1.5 % solution samples) there is a mostly weak, disordered metal structure, whereas at thicknesses exceeding 150 nm (2, 3 % solution samples) the Pt structures retain the morphology of the original BCP surface structure. The samples exhibited excellent substrate coverage as shown by large area SEM images in figure **S3.1.** The cross-

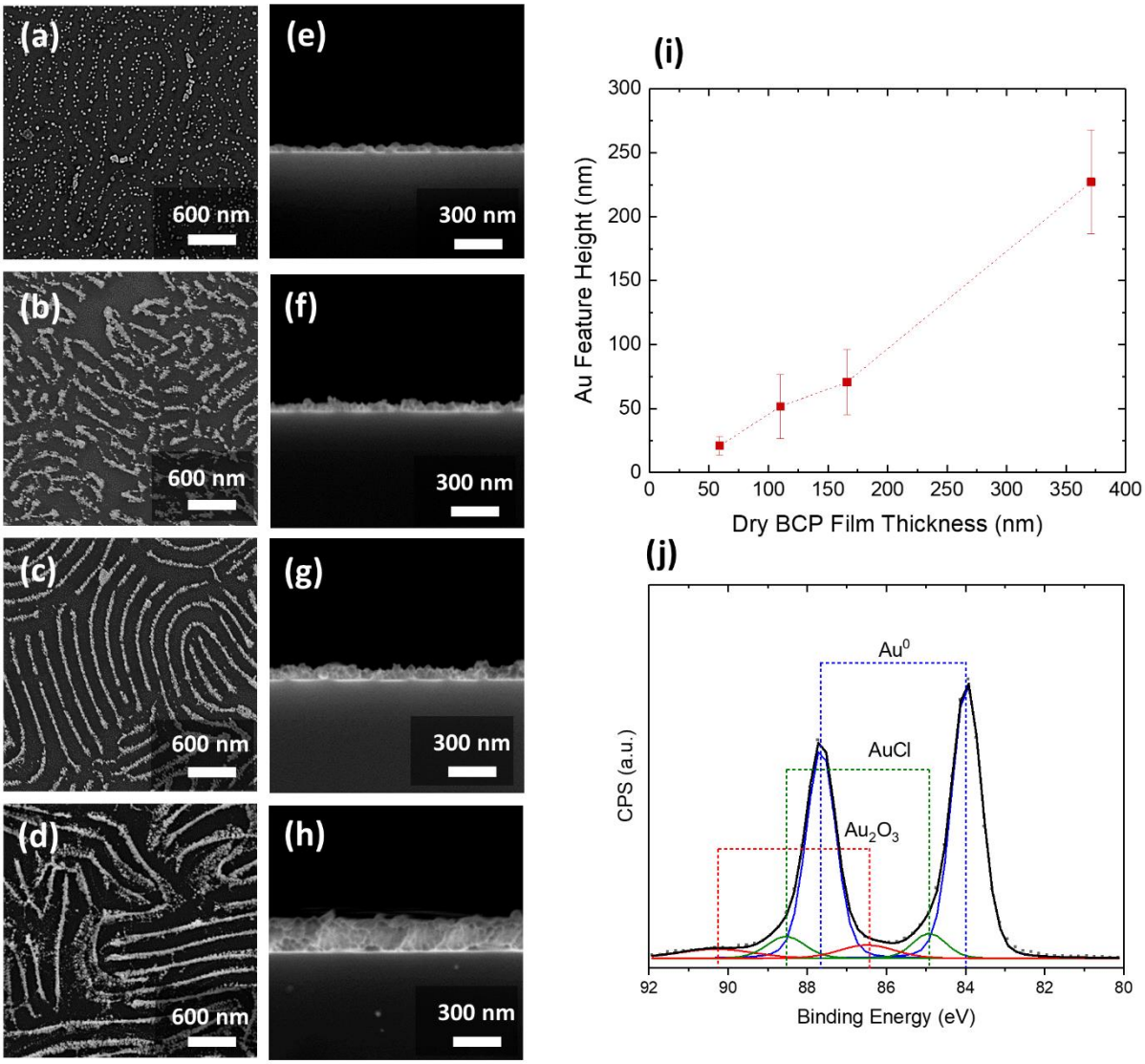

Fig. 3.4: (a) – (d) Top down SEM images of the Au nanostructures after plasma assisted polymer removal and thermal annealing, templated from 1, 1.5, 2 and 3 % BCP solutions respectively. (e) – (f) Corresponding cross-sectional SEM images. (i) Plot of the Au nanostructure height versus the thickness of the BCP template. (j) High-resolution XPS spectrum of the Au 4f region.

sectional SEM mages shown in **figure 3.3(e-f)** demonstrate a visible increase in Pt feature height with increasing BCP film thickness, with feature heights of over 250 nm obtained for the thickest BCP film sample. A quantitative comparison between the original BCP film thicknesses and the resulting feature heights is displayed in **figure 3.3(i)**, showing a linear correlation between the BCP film thickness and Pt feature height. High resolution

XPS analysis of the Pt feature (**figure 3.3(j)**) indicates the presence of platinum metal along with 2+ and 4+ oxidation states that likely correlate with PtO and PtO_2. This is in agreement with recently published work that elucidated the presence of surface oxides surrounding Pt features fabricated from salt infiltration of a BCP.[39]

Figure 3.4(a-d) show top down SEM images of the resulting Au features after O_2 plasma and thermal treatment. Similar to Pt, the Au structures arising from BCP films with thicknesses less than 150 nm (templated from the 1 %, 1.5 % w/w BCP solutions) show weak particulate features with poor connectivity. For the thicker films (templated from 2 %, 3 % BCP solutions), however, the Au features again retain the original morphology of the BCP matrix, leaving nanowall structures with heights in excess of 220 nm for the highest BCP thickness.

In comparison to the relatively homogeneous Pt structures, there appears to be a more agglomerative nature to the larger Au features, with a range of particle sizes visible within the nanowall structures for all thicknesses. **Figure 3.4(i)** shows a plot of BCP film thickness vs the resulting Au feature heights. A high resolution XPS scan of the Au features is shown in **figure 3.4(j)**, indicating the presence of almost exclusively Au metal after O_2 plasma and thermal treatment. A trace amount of Au^{1+} and Au^{3+} were also detected, the former of which we attribute to some residual Au salt that did not fully oxidise. The Au^{3+} is attributed here to some residual oxide, however, a more in-depth analysis such as cross-sectional TEM/EDX is likely required to fully resolve the origin of this species. This analysis is planned in our future work. Large area tilted SEM images are shown in **figure 3.5** for the thicker Pt (**a-d**) and Au (**e-h**) structures (templated from 2% and 3% BCP solutions), demonstrating excellent surface coverage over tens of microns across the Si substrate.

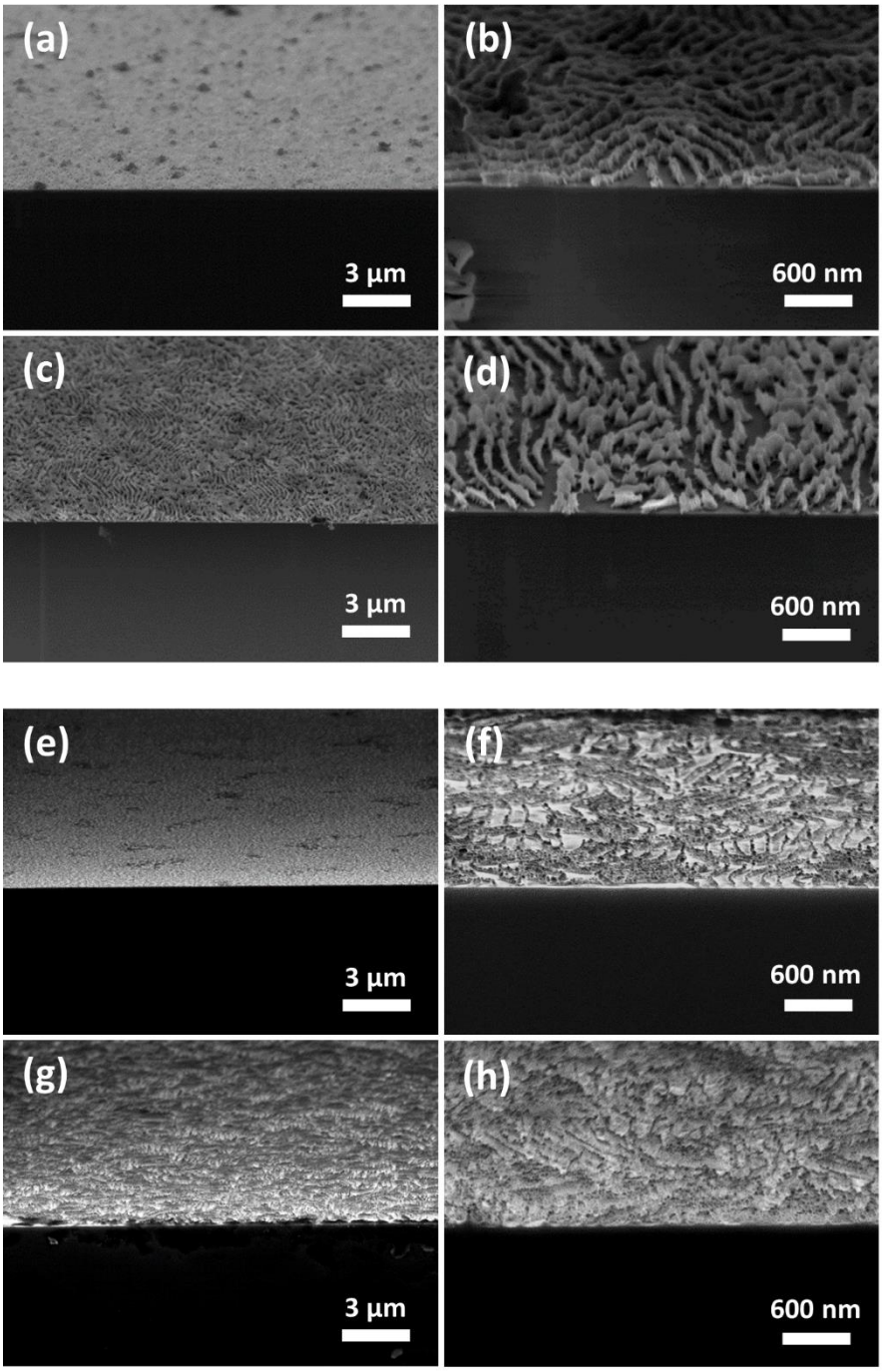

Fig. 3.5: (a) – (d) Tilted SEM images (70° tilt) of the Pt nanostructures after plasma assisted polymer removal and thermal annealing; (a, b) 2 % sample, (c, d) 3% sample. (e) – (h) Tilted SEM images (20° tilt) of the Au nanostructures after plasma etching and thermal annealing; (e, f) 2 % sample, (g, h) 3% sample. Note that the contrast for the Au images above is increased in comparison to the Pt images due to imaging difficulties arising from charging effects.

The thickness differences between the various nanostructured Au samples are also responsible for the variation in spectral behaviour shown in **figure 3.6**, which shows a plot of the total and direct reflectance. The total reflectance measurements—taken with an integrating sphere—collect all of the light reflected from the sample, while the direct measurements collect only the specular reflection. In this wavelength range, silicon is opaque so the total reflectance can be used to calculate the absorption of the sample; the direct or specular reflectance can then be used to find the scattering of the sample. For the purposes of comparison, the reflectance of a plain Si substrate is also shown in each plot. It can be observed that the reflectance decreases with increasing Au feature thickness, with the sample prepared from the 3% BCP solution exhibiting reflectance of less than 15% in the visible range (400-700 nm) vs over 30% reflectance for the 1% sample. The 3% sample also has a strong dip in direct compared to total reflectance around a wavelength of 650 nm, implying significant scattering by the substrate near this wavelength. The other samples show mainly absorption with scattering playing less of a role. It is well-known that larger Au structures have a greater ratio of scattering to absorption. As described in previous work, the decrease in reflectance for nanostructured Au films is primarily assumed to be caused by a combination of localised surface plasmon resonances (LSPRs) and the trapping of light arising from scattering throughout the nonuniform Au structures.[41] In the case where the gold nanostructure is irregular with varied uniformity and periodicity, this can facilitate multiple scattering processes that result in a broad dip in reflectance - as can be observed for the BCP-templated Au samples.[42]

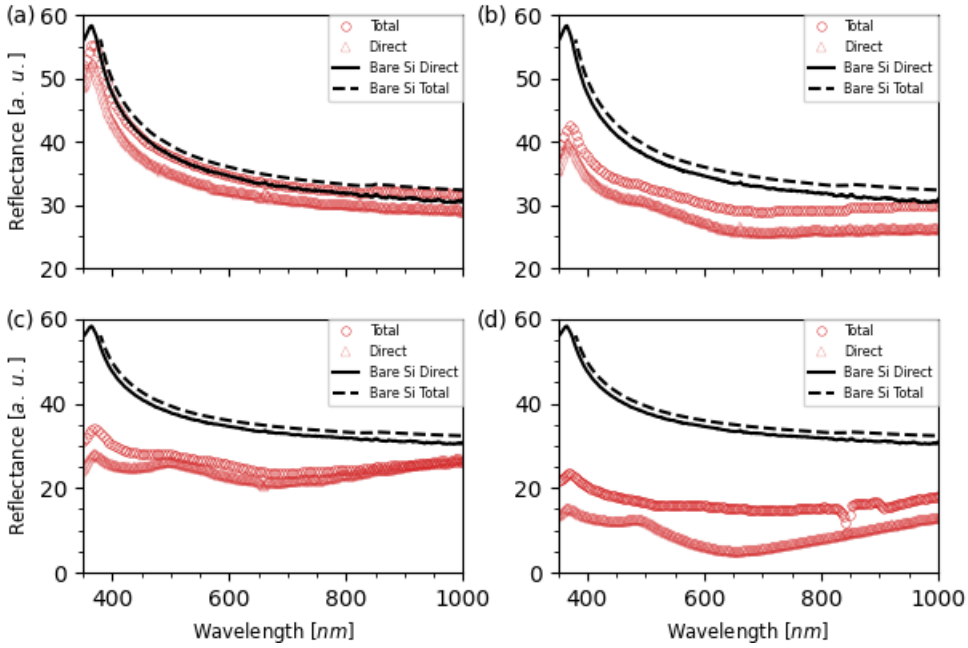

Fig. 3.6: Reflectance spectra of the Au nanostructures fabricated using a (a) 1%, (b) 1.5%, (c) 2%, and (d) 3% BCP solution. Bare Si is shown for comparative purposes in black.

In order to explore the potential catalytic application of the Au nanowall structures, the samples were utilised as photocatalysts for the degradation of methyl orange (MO). The photocatalytic activity was examined for the 1%, 2% and 3% thicknesses of Au nanowalls. As shown in **figure 3.7(a)**, the thicker Au nanostructures on the 3% sample exhibited the greatest degree of MO degradation over longer timescales of 15 hours, followed by the 2% sample. At shorter timescales up to 5 hours, however, there was little difference in degradation between the samples. **Figure 3.7(b)** shows the effects of repeated cycles of MO exposure on the Au nanowall samples. It can be observed that for all thicknesses, the Au nanowalls maintained roughly the same absorbance value over multiple uses; this indicates that the Au structures are stable on the Si substrate during multiple washes and reuse, and hence are suitable for being reused many times.

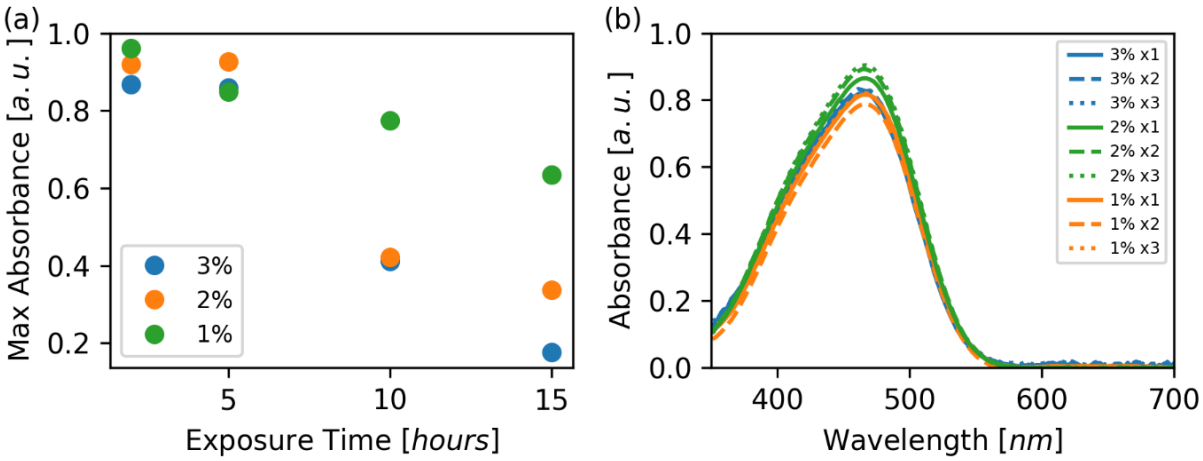

Fig. 3.7: (a) Peak UV-vis absorbance values of MO degradation for the Au nanostructured samples templated from 1%, 2% and 3% BCP solutions as a function of MO exposure time. Peak values taken from the absorption band maximum (λ_{max}). (b) UV-vis spectra of MO degradation for the Au nanostructured samples (again fabricated from 1, 2, 3% BCP solutions) over repeated exposures for 5 hours.

Overall, these results imply that the catalytic potential of the Au nanowall structures is dependent on the thickness of the metal structures. This is in agreement with previous work that found a positive correlation between the catalyst surface area and the resulting catalytic activity.[43] In comparison to MO degradation times for other substances such as Au nanoparticle solutions described in previous work,[15] however, the times required for these Au nanowall structures are comparatively slow. We suggest that one possible reason for the lower performance is related to the overall surface area of the structures - although the Au structures possess relatively high surface areas owing to their nanowall shape, their overall surface area in comparison to Au nanoparticles in solution is likely much lower. Nonetheless, there are a number of ways that the catalytic performance of BCP templated Au structures may be improved from the results described here. Firstly, if the height of the Au structures were increased this would consequently increase the available surface area and hence the catalytic performance. As was proven in **figure 3.4(i)**, this could be achieved by immersing even thicker BCP films in the metal precursor solution. Secondly, exerting precise control over the BCP morphology and/or domain spacings may be a viable alternative strategy to increase the available surface area – this will likely be examined in future work.

3.5. Conclusion:

In this study, we demonstrated the successful fabrication of large period, self-supporting, 3D metallic nanowall structures with tuneable heights via LPI of a BCP film. An UHMW PS-b-P2VP BCP system was used, which upon SVA self-assembled into lamellar structures. The BCP films were immersed in heated aqueous solutions of Au and Pt precursors in order to coordinate the metal ions to the P2VP domains. O_2 plasma etching of the polymer template followed by thermal treatment yielded both Au and Pt nanostructures. The Pt films were found to contain a mixture of both metal and oxide states, whereas the Au films primarily contained only the metallic species. A strong correlation between the BCP film thickness and the resulting metal feature heights was proven, with both Au and Pt nanowall features with maximum heights in excess of 225 nm fabricated from ~370 nm thick BCP films.

The low reflectance values for the Au nanostructures across a large wavelength range indicated the presence of a wide distribution of particle sizes, as was further confirmed by SEM imaging. The Au nanowall structures were utilised as photocatalysts for MO degradation, showing a positive association between the surface area of the Au features and the strength of the catalytic activity. Although the overall catalytic performance of the Au samples was lower than previous work,[15] we anticipate that future optimisation of our LPI technique may improve upon the results described here. We suggest a number of possible research directions that warrant further study: firstly, the expansion of Au structures to much greater heights (ideally micron scale using bulk BCP films); secondly, a performance comparison of different BCP morphologies (gyroid, cylindrical, etc.); and thirdly, an examination of the effect of the domain spacing on catalytic performance (via lower molecular weight BCP templates).Overall, we anticipate that the results of this work will contribute towards the development of novel 3D materials via BCP patterning, with applications in areas such as catalysis, filtration, sensing and optics.

3.7 References:

1. Cummins, C.; Lundy, R.; Walsh, J. J.; Ponsinet, V.; Fleury, G.; Morris, M. A., Enabling future nanomanufacturing through block copolymer self-assembly: A review. *Nano Today* **2020,** *35*, 100936.
2. Cummins, C.; Bell, A. P.; Morris, M. A., Creating Active Device Materials for Nanoelectronics Using Block Copolymer Lithography. *Nanomaterials (Basel)* **2017,** *7* (10), 304.
3. Leibler, L., Theory of Microphase Separation in Block Copolymers. *Macromolecules* **1980,** *13* (6), 1602-1617.
4. Mistark, P. A.; Park, S.; Yalcin, S. E.; Lee, D. H.; Yavuzcetin, O.; Tuominen, M. T.; Russell, T. P.; Achermann, M., Block-Copolymer-Based Plasmonic Nanostructures. *ACS Nano* **2009,** *3* (12), 3987-3992.
5. Mokarian-Tabari, P.; Senthamaraikannan, R.; Glynn, C.; Collins, T. W.; Cummins, C.; Nugent, D.; O'Dwyer, C.; Morris, M. A., Large Block Copolymer Self-Assembly for Fabrication of Subwavelength Nanostructures for Applications in Optics. *Nano Letters* **2017,** *17* (5), 2973-2978.
6. Hsueh, H.-Y.; Ho, R.-M., Bicontinuous Ceramics with High Surface Area from Block Copolymer Templates. *Langmuir* **2012,** *28* (22), 8518-8529.
7. Vukovic, I.; Punzhin, S.; Vukovic, Z.; Onck, P.; De Hosson, J. T. M.; ten Brinke, G.; Loos, K., Supramolecular Route to Well-Ordered Metal Nanofoams. *ACS Nano* **2011,** *5* (8), 6339-6348.
8. Aizawa, M.; Buriak, J. M., Block Copolymer Templated Chemistry for the Formation of Metallic Nanoparticle Arrays on Semiconductor Surfaces. *Chemistry of Materials* **2007,** *19* (21), 5090-5101.
9. Dehmel, R.; Dolan, J. A.; Gu, Y.; Wiesner, U.; Wilkinson, T. D.; Baumberg, J. J.; Steiner, U.; Wilts, B. D.; Gunkel, I., Optical Imaging of Large Gyroid Grains in Block Copolymer Templates by Confined Crystallization. *Macromolecules* **2017,** *50* (16), 6255-6262.
10. Shin, D. O.; Mun, J. H.; Hwang, G.-T.; Yoon, J. M.; Kim, J. Y.; Yun, J. M.; Yang, Y.-B.; Oh, Y.; Lee, J. Y.; Shin, J.; Lee, K. J.; Park, S.; Kim, J. U.; Kim, S. O., Multicomponent Nanopatterns by Directed Block Copolymer Self-Assembly. *ACS Nano* **2013,** *7* (10), 8899-8907.
11. Chai, J.; Buriak, J. M., Using Cylindrical Domains of Block Copolymers To Self-Assemble and Align Metallic Nanowires. *ACS Nano* **2008,** *2* (3), 489-501.
12. Ghoshal, T.; Cruz-Romero, M. C.; Kerry, J. P.; Morris, M. A., Nanosize and Shape Effects on Antimicrobial Activity of Silver Using Morphology-Controlled Nanopatterns by Block Copolymer Fabrication. *ACS Applied Nano Materials* **2019,** *2* (10), 6325-6333.
13. Zou, Y.; Zhou, X.; Ma, J.; Yang, X.; Deng, Y., Recent advances in amphiphilic block copolymer templated mesoporous metal-based materials: assembly engineering and applications. *Chemical Society Reviews* **2020,** *49* (4), 1173-1208.
14. Vukovic, I.; Brinke, G. t.; Loos, K., Block copolymer template-directed synthesis of well-ordered metallic nanostructures. *Polymer* **2013,** *54* (11), 2591-2605.
15. Mir, S. H.; Jennings, B. D.; Akinoglu, G. E.; Selkirk, A.; Gatensby, R.; Mokarian-Tabari, P., Enhanced Dye Degradation through Multi-Particle Confinement in a Porous Silicon Substrate: A Highly Efficient, Low Band Gap Photocatalyst. *Advanced Optical Materials* **2021,** *9* (11), 2002238.
16. Cianci, E.; Nazzari, D.; Seguini, G.; Perego, M., Trimethylaluminum Diffusion in PMMA Thin Films during Sequential Infiltration Synthesis: In Situ Dynamic

Spectroscopic Ellipsometric Investigation. *Advanced Materials Interfaces* **2018,** *5* (20), 1801016.
17. Peng, Q.; Tseng, Y.-C.; Long, Y.; Mane, A. U.; DiDona, S.; Darling, S. B.; Elam, J. W., Effect of Nanostructured Domains in Self-Assembled Block Copolymer Films on Sequential Infiltration Synthesis. *Langmuir* **2017,** *33* (46), 13214-13223.
18. Kamcev, J.; Germack, D. S.; Nykypanchuk, D.; Grubbs, R. B.; Nam, C.-Y.; Black, C. T., Chemically Enhancing Block Copolymers for Block-Selective Synthesis of Self-Assembled Metal Oxide Nanostructures. *ACS Nano* **2013,** *7* (1), 339-346.
19. Ghoshal, T.; Holmes, J. D.; Morris, M. A., Development of Ordered, Porous (Sub-25 nm Dimensions) Surface Membrane Structures Using a Block Copolymer Approach. *Scientific Reports* **2018,** *8* (1), 7252.
20. Ghoshal, T.; Shaw, M. T.; Bolger, C. T.; Holmes, J. D.; Morris, M. A., A general method for controlled nanopatterning of oxide dots: a microphase separated block copolymer platform. *Journal of Materials Chemistry* **2012,** *22* (24), 12083-12089.
21. Alvarez-Fernandez, A.; Nallet, F.; Fontaine, P.; Cummins, C.; Hadziioannou, G.; Barois, P.; Fleury, G.; Ponsinet, V., Large area Al2O3–Au raspberry-like nanoclusters from iterative block-copolymer self-assembly. *RSC Advances* **2020,** *10* (67), 41088-41097.
22. Cummins, C.; Morris, M. A., Using block copolymers as infiltration sites for development of future nanoelectronic devices: Achievements, barriers, and opportunities. *Microelectronic Engineering* **2018,** *195*, 74-85.
23. Cummins, C.; Gangnaik, A.; Kelly, R. A.; Borah, D.; O'Connell, J.; Petkov, N.; Georgiev, Y. M.; Holmes, J. D.; Morris, M. A., Aligned silicon nanofins via the directed self-assembly of PS-b-P4VP block copolymer and metal oxide enhanced pattern transfer. *Nanoscale* **2015,** *7* (15), 6712-6721.
24. Subramanian, A.; Tiwale, N.; Doerk, G.; Kisslinger, K.; Nam, C.-Y., Enhanced Hybridization and Nanopatterning via Heated Liquid-Phase Infiltration into Self-Assembled Block Copolymer Thin Films. *ACS Applied Materials & Interfaces* **2020,** *12* (1), 1444-1453.
25. Padbury, R. P.; Jur, J. S., Temperature-Dependent Infiltration of Polymers during Sequential Exposures to Trimethylaluminum. *Langmuir* **2014,** *30* (30), 9228-9238.
26. Waldman, R. Z.; Jeon, N.; Mandia, D. J.; Heinonen, O.; Darling, S. B.; Martinson, A. B. F., Sequential Infiltration Synthesis of Electronic Materials: Group 13 Oxides via Metal Alkyl Precursors. *Chemistry of Materials* **2019,** *31* (14), 5274-5285.
27. Peng, Q.; Tseng, Y.-C.; Darling, S. B.; Elam, J. W., A Route to Nanoscopic Materials via Sequential Infiltration Synthesis on Block Copolymer Templates. *ACS Nano* **2011,** *5* (6), 4600-4606.
28. Akyildiz, H. I.; Padbury, R. P.; Parsons, G. N.; Jur, J. S., Temperature and Exposure Dependence of Hybrid Organic–Inorganic Layer Formation by Sequential Vapor Infiltration into Polymer Fibers. *Langmuir* **2012,** *28* (44), 15697-15704.
29. Snelgrove, M.; McFeely, C.; Shiel, K.; Hughes, G.; Yadav, P.; Weiland, C.; Woicik, J. C.; Mani-Gonzalez, P. G.; Lundy, R.; Morris, M. A.; McGlynn, E.; O'Connor, R., Analysing trimethylaluminum infiltration into polymer brushes using a scalable area selective vapor phase process. *Materials Advances* **2021,** *2* (2), 769-781.
30. Mullen, E.; Morris, M. A., Green Nanofabrication Opportunities in the Semiconductor Industry: A Life Cycle Perspective. *Nanomaterials* **2021,** *11* (5).
31. Cummins, C.; Ghoshal, T.; Holmes, J. D.; Morris, M. A., Strategies for Inorganic Incorporation using Neat Block Copolymer Thin Films for Etch Mask

Function and Nanotechnological Application. *Advanced Materials* **2016,** *28* (27), 5586-5618.
32. Chai, J.; Wang, D.; Fan, X.; Buriak, J. M., Assembly of aligned linear metallic patterns on silicon. *Nature Nanotechnology* **2007,** *2* (8), 500-506.
33. Subramanian, A.; Doerk, G.; Kisslinger, K.; Yi, D. H.; Grubbs, R. B.; Nam, C.-Y., Three-dimensional electroactive ZnO nanomesh directly derived from hierarchically self-assembled block copolymer thin films. *Nanoscale* **2019,** *11* (19), 9533-9546.
34. Lee, J.; Mishra, A. K.; Choi, C.; Kim, D.; Kim, E. Y.; Yong, K.; Kim, J. K., Three-Dimensional Nanoporous Metal Structures from Poly(2-vinylpyridine)-block-Poly(4-vinylpyridine) Copolymer Thin Film. *ACS Applied Materials & Interfaces* **2020,** *12* (13), 15667-15674.
35. Stefik, M.; Guldin, S.; Vignolini, S.; Wiesner, U.; Steiner, U., Block copolymer self-assembly for nanophotonics. *Chemical Society Reviews* **2015,** *44* (15), 5076-5091.
36. Banbury, C.; Rickard, J. J. S.; Mahajan, S.; Goldberg Oppenheimer, P., Tuneable Metamaterial-like Platforms for Surface-Enhanced Raman Scattering via Three-Dimensional Block Co-polymer-Based Nanoarchitectures. *ACS Applied Materials & Interfaces* **2019,** *11* (15), 14437-14444.
37. Onses, M. S.; Song, C.; Williamson, L.; Sutanto, E.; Ferreira, P. M.; Alleyne, A. G.; Nealey, P. F.; Ahn, H.; Rogers, J. A., Hierarchical patterns of three-dimensional block-copolymer films formed by electrohydrodynamic jet printing and self-assembly. *Nature Nanotechnology* **2013,** *8* (9), 667-675.
38. Chang, T.; Huang, H.; He, T., Directed Self-Assembly of Diblock Copolymer Thin Films on Prepatterned Metal Nanoarrays. *Macromolecular Rapid Communications* **2016,** *37* (2), 161-167.
39. Lee, W.; Lee, S.; Tang, A. S.; Kim, C.; Liu, R.; Im, K.; Jung, H.-T.; Ross, C. A., Platinum Infiltration of a Block Copolymer for Interconnected Three-Dimensional Metal Nanostructures. *ACS Applied Nano Materials* **2021,** *4* (1), 793-801.
40. Brassat, K.; Lindner, J. K. N., Nanoscale Block Copolymer Self-Assembly and Microscale Polymer Film Dewetting: Progress in Understanding the Role of Interfacial Energies in the Formation of Hierarchical Nanostructures. *Advanced Materials Interfaces* **2020,** *7* (5), 1901565.
41. Xu, Z.; Chen, Y.; Gartia, M. R.; Jiang, J.; Liu, G. L., Surface plasmon enhanced broadband spectrophotometry on black silver substrates. *Applied Physics Letters* **2011,** *98* (24), 241904.
42. Vitrey, A.; Alvarez, R.; Palmero, A.; González, M. U.; García-Martín, J. M., Fabrication of black-gold coatings by glancing angle deposition with sputtering. *Beilstein Journal of Nanotechnology* **2017,** *8*, 434-439.
43. Kgatle, M.; Sikhwivhilu, K.; Ndlovu, G.; Moloto, N., Degradation Kinetics of Methyl Orange Dye in Water Using Trimetallic Fe/Cu/Ag Nanoparticles. *Catalysts* **2021,** *11* (4).

3.7. – Chapter 3 Appendix

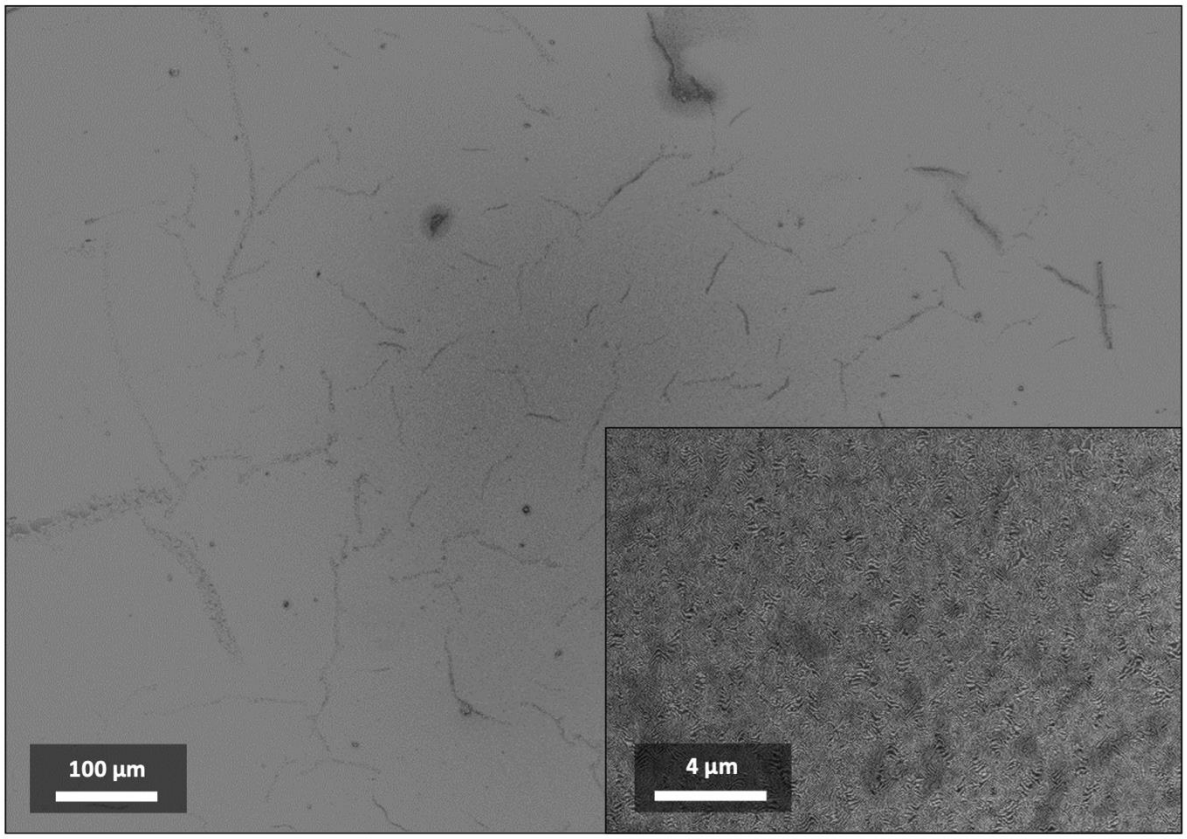

Figure S3.1. Large area SEM images of the Au nanostructures on the sample fabricated from a 2% BCP solution. DeMoivre patterns are visible on the inset, which indicates large area ordering.

Chapter 4: Block Copolymer Templated WO_3 Surface Nanowires as Catalysts for Enhanced Epinephrine Sensing and the Oxygen Evolution Reaction.

4.1. Abstract

Herein, we report the development of a novel, multifunctional WO_3 catalytic device using a facile and ambient-temperature block copolymer (BCP) templating process. Firstly, a BCP film was deposited and self-assembled atop an indium tin oxide substrate. A tungsten precursor was then uptaken into the film via a liquid phase infiltration technique, which upon UV-ozone treatment yielded WO_3 surface nanowires (NWs) with excellent substrate coverage. The resulting WO_3NWs-ITO device was firstly investigated as a photoanode for the oxygen evolution reaction (OER). The onset overpotential of the WO_3NWs-ITO electrode was determined to be 240 mV and 390 mV, with and without light illumination respectively. Secondly, the applicability of WO_3NWs-ITO device for electrochemical sensing of epinephrine (EP) was explored using cyclic voltammetry and amperometry, exhibiting a linear response in a wide working range of 0.5 – 250 μM with a sensitivity of 0.0491 μA μM^{-1} and a detection limit of 0.086 μM. The device demonstrated high durability over multiple EP measurements, as well as strong anti-interference abilities versus well-known interfering compounds. Additionally, the device was successfully applied to determine the EP concentration in commercial drug samples. This study broadens the potential of BCP templating for developing low-cost, high-performance electrocatalytic devices.

4.2. Introduction

Semiconducting metal oxide (SMO) materials are the subject of intense research interest from a diverse range of fields, including water splitting,[1] photovoltaic cells,[2, 3] electrochemical sensing,[4] to name a few. Among the numerous SMO materials, tungsten oxide (WO_3), an n-type SMO, has attracted extensive attention owing to its unique electronic and optical properties, high abundance, and stability.[5] The location of the WO_3

bandgap at ~2.6-3.0 eV has drawn particular attention to its potential as an oxygen evolution catalyst (OEC), as theoretically this allows the material to absorb up to 12% of the solar spectrum.[6-8] The strong catalytic behaviour of WO_3 has also been employed for electrochemical sensing of a wide range of species, including gases such as NH_3, SO_2, H_2, along with a number of biomolecules including ammonia, carbon monoxide, methanol among others[9-14]

Nanostructured SMO materials, in comparison to their bulk counterparts, offer improved catalytic performance due to increased surface area along with enhanced charge migration.[15-17] Consequently, many recent studies have focused on enhancing the unique catalytic properties of WO_3 through synthesizing a wide variety of nanostructured morphologies. Various synthesis methods have been explored, including sputtering,[13] chemical vapour deposition,[18] sol-gel,[19] hydrothermal/solvothermal methods,[15, 20, 21] and nanoparticle functionalisation.[22-25] These methods have successfully resulted in well-performing WO_3 nanostructured catalytic devices but many are restricted by the cost of production and limited scalability - thereby hindering future commercialization.[22, 26] Hence, it is essential that novel cost-effective and scalable techniques are developed for WO_3 catalytic applications.

In this regard, our report demonstrates the synthesis and surface characterisation of a unique nanostructured WO_3 catalytic device via a room-temperature block copolymer (BCP) strategy. The use of BCP self-assembly as a cheap, competitive bottom-up fabrication approach for surface nanostructures is well-documented.[27, 28] By varying a number of key parameters such as the molecular weight, volume fraction, or annealing conditions, a diverse range of morphologies may be produced using BCP films, which are typically sub-100 nm in thickness.[29] Depending on the chemical nature of the constituent blocks, BCP films can then act as templates for the creation of metal or metal oxide structures. For instance, BCP films containing domains capable of metal ion coordination (such as poly(-2 or -4vinylpyride), PVP or poly(ethylene oxide) PEO) may be infiltrated with metal ions via solution or vapor-based methods.[30, 31] Owing to their high scalability and low cost, BCP-templated nanomaterials have found applications in many emerging technologies including nanoporous membranes, antireflective surfaces, chemical sensing, and photocatalysis, as described in the following reviews.[30, 32, 33] In relation to electrochemical applications, our previous reports document how a BCP-based

approach can be exploited to create enhanced sensing devices using templated CuO and Fe_2O_3 nanosurfaces.[34, 35] On account of the success of these studies, it seemed critical to further explore the capability of BCP-templated structures as catalytic devices.

Accordingly in this work, we demonstrate the synthesis and characterisation of a unique catalytic device consisting of large-area (25×25 mm), densely packed arrays of WO_3 surface nanowires atop an ITO substrate (hereafter referred to as WO_3NWs-ITO). The device is fabricated using an entirely ambient-temperature strategy, which involves infiltrating a poly(styrene)-*block*-poly(4-vinylpyridine) (PS-*b*-P4VP) BCP film with tungsten chloride, followed by UV-ozone treatment to oxidise the precursor. We investigate the diverse electrocatalytic applications of the WO_3NWs-ITO material; firstly, by examining its use as an oxygen evolution reaction (OER) anode using linear sweep voltammetry (LSV), electrochemical impedance spectroscopy (EIS) and cyclic voltammetry (CV) methods. The electrolysis of water is pivotal for various renewable energy sources, with great demand for the development of stable, low cost oxygen evolution reaction (OER) catalytic materials.[36] Secondly, we investigate the sensing performance of WO_3NWs-ITO towards the electrochemical oxidation of epinephrine (EP) - demonstrating a wide working range, a low detection limit, and high sensitivity in the presence of a range of interfering compounds. The crucial role that EP plays as a neurotransmitter as well as a medicine signifies the need for highly sensitive sensing to further our knowledge. Overall, the results disclosed in this article illustrate the multifunctional applicability of WO_3 nanowires derived by BCP lithography, further reinforcing the outstanding potential of BCP-templated metal oxide structures for the fabrication of diverse catalytic materials.

4.3 Experimental Method:

4.3.1. Reagents:

Potassium hydroxide (KOH, 99%) was supplied from Merck for the water oxidation application. Adenine (A, from Sigma-Aldrich), guanine (G, from Sigma-Aldrich), phenylalanine (Phe, from Sigma-Aldrich), uric acid (UA, from Alfa Aesar), ascorbic acid (AA, from J. T. Baker), glucose (Glu, from Sigma-Aldrich), dopamine hydrochloride (DA, from Sigma-Aldrich) and epinephrine hydrochloride (Ep, from Sigma-Aldrich) were procured for the electrochemical sensing application. Tungsten (IV) chloride

(WCl_4), toluene (99.8%, anhydrous), tetrahydrofuran (99.8%, anhydrous), chloroform (99.8%, anhydrous), and ethanol (99.5%, HPLC grade) were purchased from Sigma-Aldrich. Indium tin oxide (ITO)-coated glass slides with a surface resistivity of 8−12 Ω/sq were supplied from Sigma-Aldrich. Poly(styrene)-*block*-poly(4-vinylpyridine) (M_n: 25-*b*-10 kg/mol, PDI: 1.15) was obtained from Polymer Source Inc. and was used without any further purification steps.

4.3.2. Fabrication of WO_3NWs-ITO electrode:

The ITO substrates were firstly cleaned through ultrasonication in ethanol for 20 minutes, followed by drying under nitrogen (N_2) gas. The PS-*b*-P4VP BCP was dissolved at a concentration of 0.75% w/w in an 80:20 solution of toluene and THF, which was stirred for 12 hrs to ensure complete dissolution. The resulting solution was then spin-coated directly onto the ITO substrates at a speed of 3200 rpm for 30 seconds. Solvent vapor annealing (SVA) was carried out in a saturated chloroform environment for approximately 1 hr following the method outlined in our previous work.[37, 38] Surface reconstruction was performed by immersing the BCP films in ethanol under ambient conditions for 20 minutes, followed by drying under N_2 gas. A 1% w/w WCl_4 solution was prepared in ethanol and spin-coated at 3200 rpm onto the reconstructed BCP films, which were then converted to WO_3 nanowires via a 3 hr UV/ozone treatment (PSD Pro Series Digital UV Ozone System; Novascan Technologies, Inc., USA).

4.3.3. Apparatus and Instrumentation:

Atomic Force Microscopy (AFM) (Park XE7, Park Systems, Korea) was performed in non-contact mode under ambient conditions using silicon cantilevers (PPP-NCHR, Nanosensors, USA) with a force constant of 42 N m^{-1}. Scanning Electron Microscopy (SEM) images were taken using a Carl Zeiss Ultra plus with an InLens detector. X-ray photoelectron spectroscopy (XPS) was performed using an Omicron MultiProbe XPS with a monochromated Al Kα source (XM 1000, 1486.7 eV). The instrument base pressure was 5×10^{-11} mbar, with an instrumental resolution of 0.6 eV. All energetic positions were corrected with respect to C1s (284.8 eV) and were fitted using Casa XPS software with Gaussian/Lorentzian line-scans and a Shirley background. X-ray diffraction (XRD) was performed using a Bruker D8 Advance XRD system with a Cu Kα source. Raman analysis was performed using a LabRAM ARAMIS system (HORIBA

Jobin Yvon) with a 532 nm laser. The water oxidation reactions were conducted in a CHI 760D potentiostat (CH Instruments, USA) with a conventional three-electrode system by using WO_3NWs-ITO, Pt plate and Ag/AgCl (3 M KCl) electrodes as working, auxiliary and reference electrodes, respectively. In the sensor study, the electrochemical measurements were performed by using a CHI-660C electrochemical analyser (CH Instruments, USA) with a conventional three-electrode system including WO_3NWs-ITO as a working electrode, a Pt wire auxiliary electrode an Ag/AgCl (3 M KCl) reference electrode.

4.4. Results and Discussion:

4.4.1. Electrode preparation and characterization:

The fabrication process for the WO_3NWs-ITO electrode is outlined in **figure 4.1.** This is a modified version of the strategy utilized in our previous studies to create both iron oxide and copper oxide nanostructures for sensing applications.[34, 35]

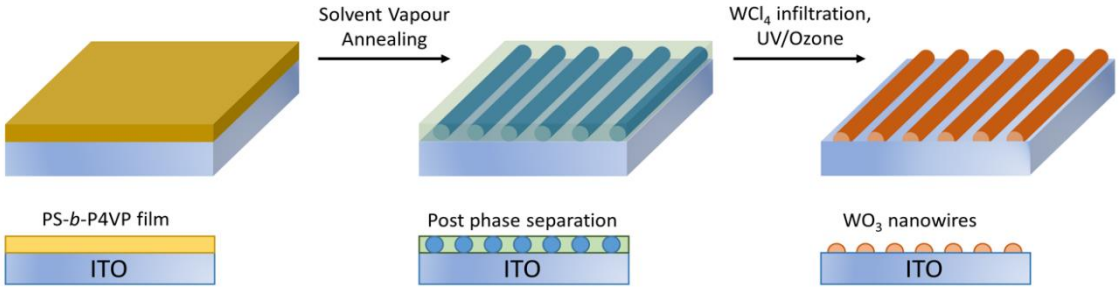

Figure 4.1. Fabrication process for WO_3 NWs nanostructure on ITO**.**

The PS-*b*-P4VP films were spin-coated onto ITO substrates at a concentration of 0.75 % w/w and were annealed in a chloroform atmosphere for approximately 1 hour. The SVA process enabled the BCP films to self-assemble into a parallel cylindrical structure with periodicity of 36 $\pm$ 1 nm. Note that the BCP solution concentration value of 0.75 % w/w is slightly higher than in previous studies, as it was found that thicker films gave more uniform coverage due to the roughness of the ITO substrates. The microphase-separated films were then swollen in ethanol to develop a porous template.[39] An ethanolic solution of WCl_4 was subsequently spin-coated onto the films, which were converted into WO_3 nanostructures via UV-ozone treatment.[38] **Figure 4.1(a, c)** show SEM and AFM images

of the phase-separated BCP film on ITO after SVA, demonstrating excellent substrate surface coverage. The average periodicity and diameter of the WO_3 features were measured (on pure Si, see **figure S4.1.)** to be approximately 36 $\pm$ 1 nm and 22 $\pm$ 4 nm respectively. The nanowire thickness was calculated to be ~6 nm from analysing topographic AFM data on a Si substrate. SEM and AFM images of the resulting WO_3 nanostructure after UV/ozone treatment are shown in **figure 4.1(b, d)** again displaying large area coverage.

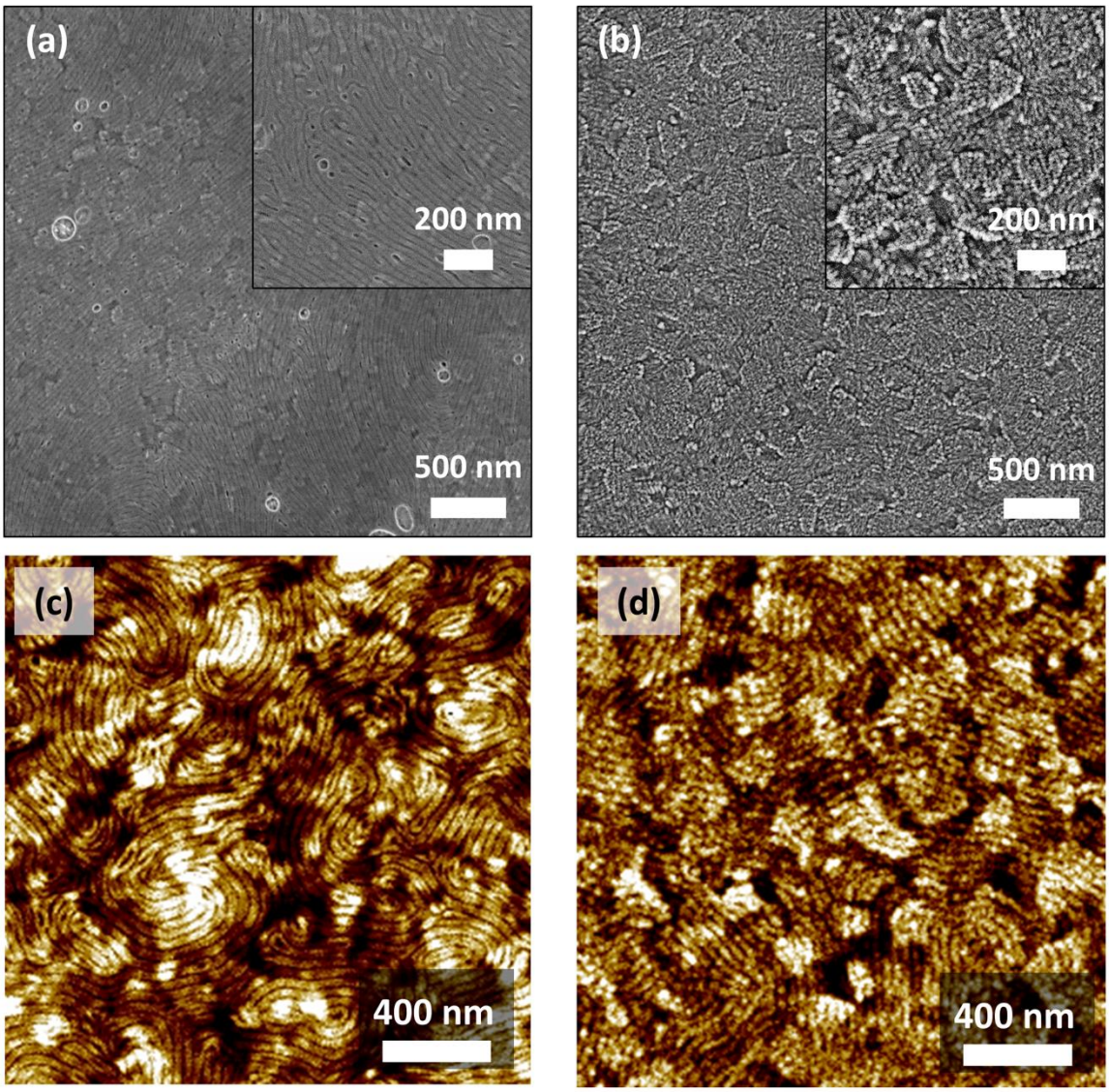

Figure 4.2. SEM and AFM images of (a, c) the PS-*b*-P4VP film spin-coated onto an ITO substrate, and (b, d) the WO_3 nanowire array after WCl_4 infiltration and UV-ozone treatment.

XPS analysis was performed in order to chemically characterize the resulting WO_3NWs-ITO material. **Figure 4.3a** shows the survey spectrum of the BCP film atop the ITO substrate. The presence of C and N is attributed to the BCP film, with some O also visible that likely arises from adsorbed oxygen on the sample surface. The notable absence of In or Sn peaks further verify the excellent surface coverage of the BCP film across the ITO. **Figure 4.3b** displays the survey spectrum of the WO_3 nanowires. W (16.9 at. %), Sn (1.5 at. %), In (5.8 at. %), and O (51.3 at. %) are present (as expected from the substrate), with C (18.1 at. %) and N (4.5 at. %) also visible that likely originate from adventitiously absorbed carbon along with some residual BCP material.

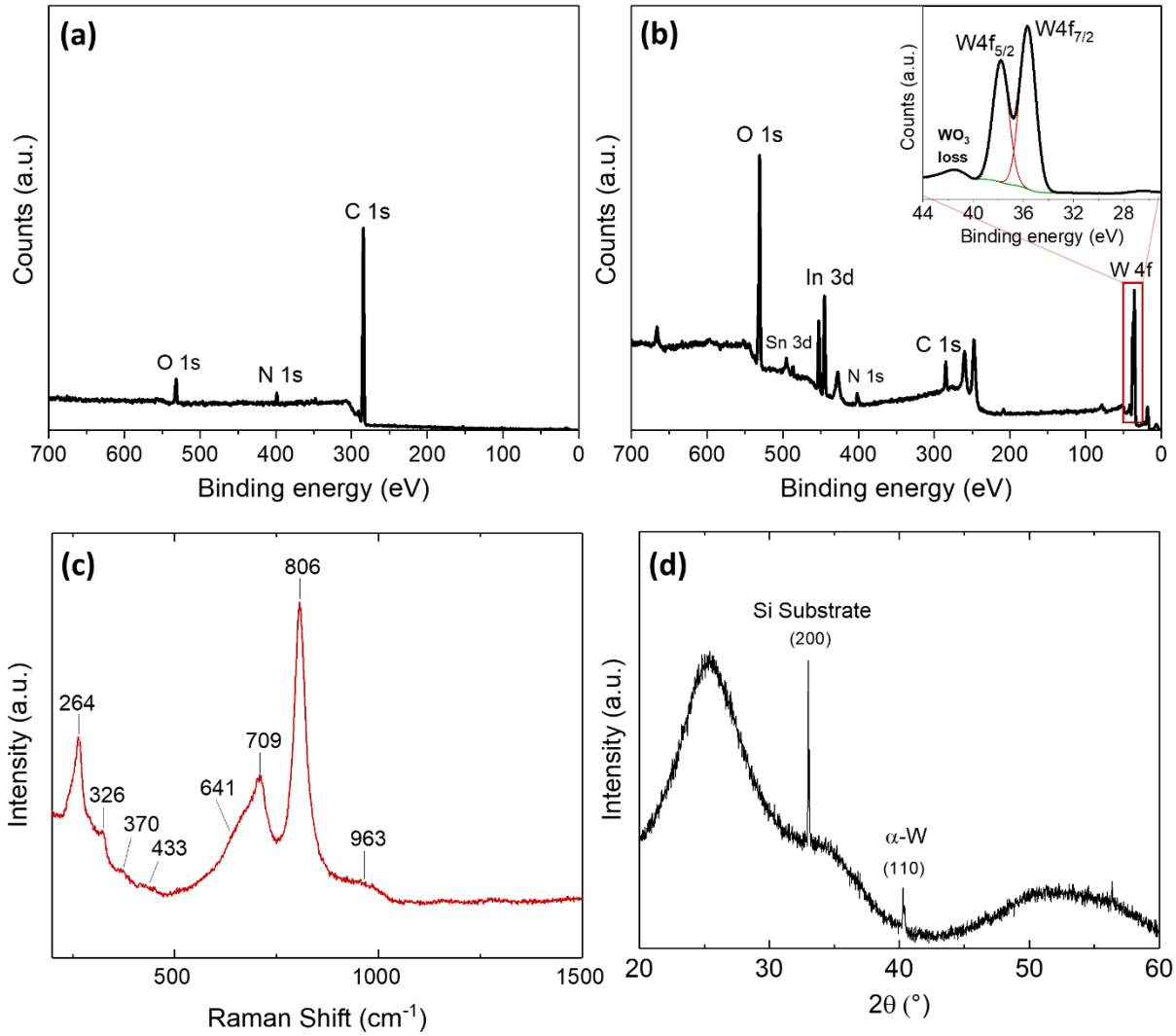

Figure 4.3. XPS survey spectra of (a) the PS-*b*-P4VP film on ITO substrate, and (b) the WO_3 nanowire array on ITO after UV/ozone. A high-resolution scan of the W4f region is shown inset. (c), (d) show the Raman and XRD spectra of the WCl_4 precursor after UV/ozone treatment.

A high-resolution scan of the W 4f region is shown inset in **figure 4.3b**, with a doublet peak associated with W $4f_{5/2}$ and W $4f_{7/2}$ (visible at 37.8 eV and 35.7 eV respectively) indicating the presence of W^{6+} from the WO_3 nanowires.[38, 40] A WO_3 loss feature is also visible at 41.5 eV. The O 1s high-resolution scan (see **figure S4.2**) displays two de-convoluted peaks at 530.6 eV and 532 3 eV, which are attributed to stoichiometric WO_3 and non-stoichiometric WO_{3-x} species respectively.[41] Investigation of the nanowire crystallinity via Raman spectroscopy and XRD was attempted, however due to the ultrathin nature of the WO_3 nanowires no detectable signal was obtained.[31, 42] Instead, Raman spectroscopy and XRD were performed on a bulk, solution cast film of the WCl_4 precursor after a similar UV/ozone treatment, which we cautiously expect will possess the same crystallinity as the WO_3 nanowires (see **figure 4.3(c, d)**).The Raman bands observed at 264, 326, 709 and 806 cm^{-1} are consistent with monoclinic tungsten oxide (*m*-WO_3).[43] The weak band visible at 433 cm^{-1} is also indicative of crystalline WO_3.[44] A notable exception are the two small asymmetric peaks observed at approximately 641 and 963 cm^{-1}, which are not attributed to *m*-WO_3. We instead assign this peaks to the presence of hydrated amorphous WO_3 in accordance with previous work.[45] The Raman results therefore indicate the formation of a mixture of both amorphous and crystalline WO_3 during the UV/ozone process. The XRD spectrum displays a broad band centred at approximately 26° with a shoulder peak at around 34°, both of which indicate the presence of mainly amorphous WO_3 with a low degree of crystallinity.[46] A small peak is visible at around 40.5°, which we attribute to some trace α-phase W that may have formed at the silicon substrate interface during UV/ozone.[47]

4.4.2 Water Oxidation Properties:

The catalytic activity of WO_3NWs-ITO electrode was examined by using linear sweep voltammetry (LSV), electronic impedance spectroscopy (EIS) and cyclic voltammetry (CV) techniques for oxygen evolution reaction (OER) by water oxidation. As shown in **figure 4.4a**, LSV measurements were carried out in the potential frame between 1.2 and 1.9 V vs. RHE with and without visible light illumination in an anaerobic 1 M KOH solution with 50 mV s^{-1} scan rate, which were compared with a bare ITO electrode. The onset overpotential of WO_3NWs-ITO electrode, both in the absence and presence of visible light illumination, was determined to be 390 mV and 240 mV respectively. Additionally, the lowest overpotential of 0.615 V was exhibited by the WO_3NWs-ITO

electrode under light illuminated conditions at a current density of 1 mA cm^{-2}. Under dark conditions, the WO_3NWs-ITO electrode shows an overpotential of 0.652 V at 1 mA cm^{-2}. Photoelectrochemical water oxidation for OER were investigated by using bulk and surface oxygen vacancies of WO_3 photoanodes and oxygen vacancies of WO_3 displayed ~0.15 V cathodic onset potential shift in comparison with bulk WO_3 photoanode.[21] Photoelectrochemical properties of vertically aligned WO_3 nanowire were investigated for the photoelectrolysis and displayed the highest saturation photocurrent of 1.43 mA cm^{-2} under solar illumination.[15] Gonçalves et al. reported that colloidal WO_3 nanowires for solar water splitting and it is reached 1.96 mA cm^{-2} at 1.23 V RHE under AM1.5G solar irradiation.[48] Nonetheless, we believe that the overall catalytic activity of WO_3NWs-ITO in this study is somewhat reduced due to the low content of catalyst on the electrode. Our future studies will attempt to improve on this initial result through further fine-tuning of the BCP inclusion process for synthesizing thicker and denser (in height and diameter) metal oxide structures.

EIS was then performed in order to further characterize the electrical behaviour of the WO_3NWs-ITO electrode. Nyquist plots of bare and WO_3NWs-ITO electrodes as shown in the **figure 4.4b**. The EIS experiments were carried out in an anaerobic 1 M KOH solution with steady potential at 1.75 V *vs.* RHE changing frequency from 0 to 150000 Hz. The impedance changes of the modified electrodes were dependent on the charge-transfer resistance value (R_{ct}), which is directly proportional to the diameter of the semicircles. The larger semicircle curve was observed for the bare ITO in Nyquist plot, indicating that the bare electrode faced too much resistance of electrons.[49] Conversely, the WO_3NWs-ITO electrode displayed significantly smaller semicircle curves under both illuminated and dark conditions. This observation can be explained by the WO_3 nanostructured surface acting as an electron transfer layer in the WO_3NWs-ITO electrode, thereby reducing charge-transfer resistance.[50] Overall, these results demonstrate that the WO_3NWs-ITO electrodes exhibit catalytic activity both in the absence and presence of light illumination, with increased catalytic activity under illumination due to the light absorption properties of WO_3.[51]

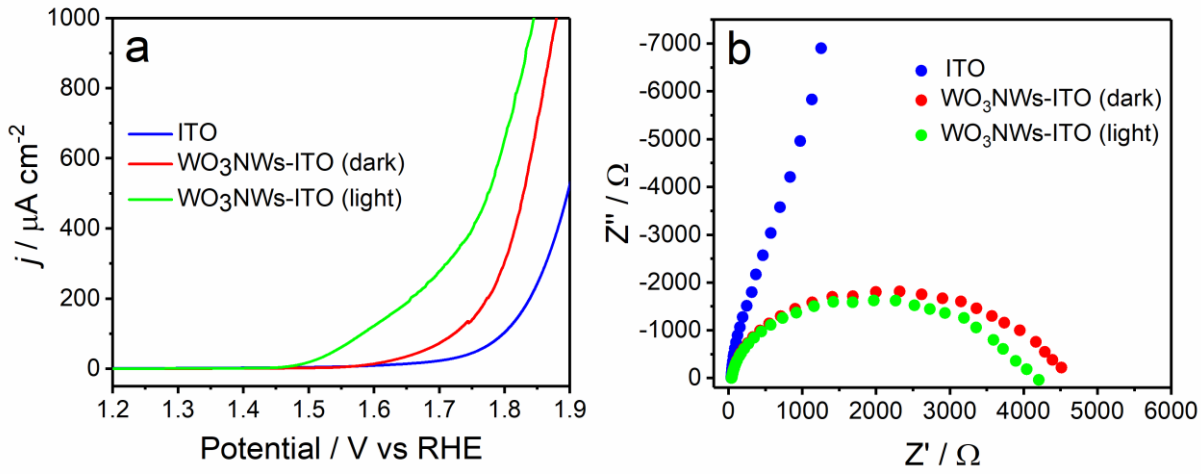

Figure 4.4. The electrocatalytic oxygen evolution polarization curves **(a)** and EIS Nyquist plots **(b)** of WO_3NWs-ITO electrodes with or without illuminated conditions.

Additionally, the double-layer capacitance (C_{dl}) value of WO_3NWs-ITO electrode was calculated using cyclic voltammetry, where no faradaic processes were detected between 1.00 and 1.10 V vs. RHE. C_{dl} values of the bare and WO_3NWs-ITO electrodes were calculated by different scan rates (10, 20, 30, 40, 50, 70, 90 mV s^{-1}) as shown **Figure S4.3(a-b)**. Capacitive current differences were plotted as a function of scan rate, with the slopes of the linear fit giving C_{dl} (**Figure S4.3c**). Hence, C_{dl} values of 0.1361 mF and 0.0687 mF were obtained for the WO_3NWs-ITO electrode and bare electrode respectively. The higher C_{dl} value indicates the greater electroactive area of the WO_3NWs-ITO electrode for catalytic activity in comparison to the bare electrode. These results further demonstrate the catalytic activity of the WO_3NWs-ITO electrode under both dark and illuminated conditions for OER.

4.4.3. Epinephrine Sensing Properties:

As a further application, the sensing performance of WO_3NWs-ITO was examined by monitoring the oxidation peak signals of epinephrine (EP). EP, also called adrenalin, is an electroactive catecholamine neurotransmitter that can be easily oxidized to epinephrinequinone.[52] EP plays a crucial role in the regulation of blood pressure along with the functioning of the central nervous system and cardiovascular system. Any abnormal deviation in EP levels can result in several diseases; [53, 54] therefore, the effective and rapid detection of EP concentrations is of great importance.

To assess the electrochemical behaviour of the modified ITO electrodes, ITO, BCP-ITO and WO_3NWs-ITO were firstly characterized by cyclic voltammetry (CV) technique using 5 mM $Fe(CN)_6^{3-/4-}$ solution in 0.1 M KCl. The CV of the WO_3NWs-ITO electrode was compared to that of the bare ITO electrode along with the BCP film on ITO, as shown in **figure 4.5a**. The WO_3NWs-ITO electrode displayed well-defined anodic and cathodic peaks at potentials of 0.426 V and -0.095 V, respectively. As illustrated of **figure 4.5a**, the untreated ITO electrode (called as ITO) displayed peaks similar to those of WO_3NWs-ITO. After deposition of the surface of ITO with the block copolymer, the BCP modified ITO electrode (called as BCP-ITO) did not show any appreciable signal for the redox reaction. Overall, both the anodic and cathodic peak currents of the WO_3NWs-ITO electrode were notably higher than that of the bare ITO and BCP/ITO electrodes, demonstrating the enhanced electrocatalytic activity of the WO_3NWs.

From CVs shown in **figure 4.5a**, the electrochemical active surface areas of both ITO and WO_3NWs-ITO were estimated according to the Randles-Sevcik equation.[55] The electrochemically active surface areas are 0.089 cm^2 and 0.163 cm^2 for ITO and WO_3NWs-ITO respectively, indicating that the WO_3NWs increased the active surface area of the electrode. Furthermore, the electron transfer ability of ITO, BCP-ITO and WO_3NWs-ITO were evaluated by electrochemical impedance spectroscopy (EIS) measurement using 5 mM $Fe(CN)_6^{3-/4-}$ solution containing 0.1 M KCl. In the Nyquist diagrams given in **figure 4.5b**, the transfer resistance (R_{ct}) values can be estimated as 9933 Ω for ITO and 19855 Ω for

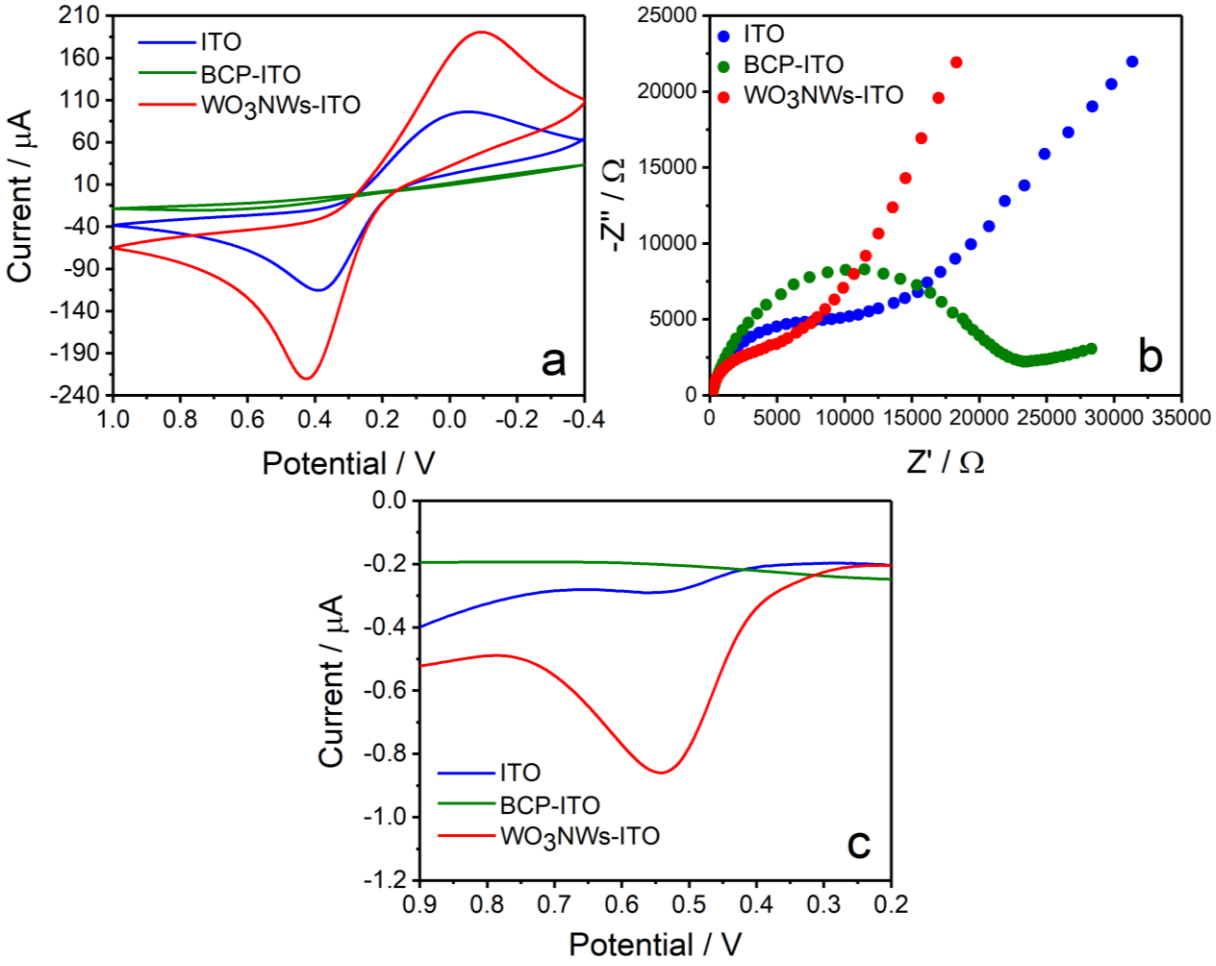

Figure 4.5. (a) CVs of ITO, BCP-ITO and WO_3NWs-ITO in 5 mM $Fe(CN)_6^{3-/4-}$ solution containing 0.1 M KCl. Scan rate: 50 mVs^{-1}. **(b)** Nyquist plots of ITO, BCP-ITO and WO_3NWs-ITO in 5 mM $Fe(CN)_6^{3-/4-}$ solution containing 0.1 M KCl. **(c)** DPVs of ITO, BCP-ITO and WO_3NWs-ITO in the presence of 10 µM Ep in 0.1 M acetate buffer solution (pH 5.4).

BCP-ITO. After the modification of ITO with WO_3NWs, the R_{ct} value of WO_3NWs-ITO decreased dramatically and the R_{ct} value was found to be 4380 Ω. The smaller resistance value of WO_3NWs-ITO can be attributed to the excellent conductivity and the large active surface area of WO_3NWs on ITO.[56-58]

To evaluate the electrochemical performance of WO_3NWs toward EP, the Differential Pulse Voltammetry (DPV)s of different modified electrodes (ITO, BCP-ITO and WO_3NWs-ITO) were also recorded in the presence of 10 µM EP in N_2-saturated 0.1 M acetate buffer solution (pH 5.4) with a scan rate of 50 mVs^{-1}. As can be observed in

figure 4.5c, the DPV signal of 10 µM EP obtained from ITO is significantly weaker in comparison to that of WO_3NWs-ITO. Furthermore, no oxidation peak is evident for the BCP-ITO in the potential range of 0.2 and 0.9 V. These results demonstrate that WO_3NWs possess excellent electrocatalytic activity for the electrooxidation of EP.

Additionally, the DPV technique was employed to investigate the analytical characteristics of the WO_3NWs-ITO. **Figure 4.6a** shows DPV signals of WO_3NWs-ITO for different concentrations of EP in 0.1 M acetate buffer solution (pH 5.4). The peak currents increased

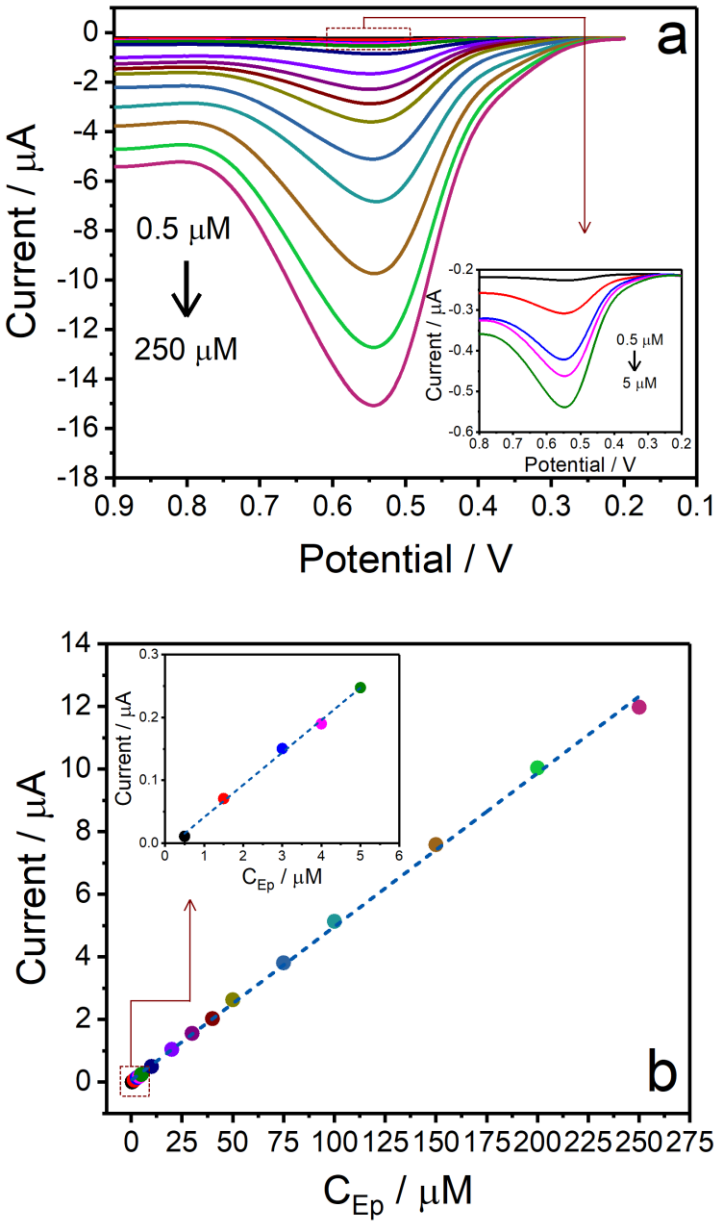

Figure 4.6. (a) DPVs of WO_3NWs-ITO in 0.1 M acetate buffer solution (pH 5.4) containing different concentration of Ep. **(b)** Calibration plot for detection of Ep.

linearly with the increasing of EP concentration in the concentration range of 0.5 and 250 μM. **Figure 4.6b** shows the variation in response currents of the WO_3NWs-ITO as a function of EP concentration. A statistical analysis of the calibration plot yielded a linear regression equation of I_{Ep} (μA) = 0.0638 + 0.0491C_{Ep} (μM) (R=0.9988) with a detection limit of 0.086 μM (3SD/m).[59] To compare the sensing performance of WO_3NWs-ITO with other EP sensors reported in recent years, the analytical characteristics (linear range, detection limit and sensitivity) of these sensors are summarized in **Table 4.1**.

<	Technique	Linear range (μM)	Detection limit (μM)	Sensitivity (μA μM^{-1})	Practical use	Reference
AuNPs/cysteic acid/GCE	DPV	0.4 – 11.7	0.080	1.2631	human blood serum sample	60
CTAB-SnO_2/GCE	SWV	0.1 – 250	0.01	0.092*	human urine sample	61
Au/PILs/PPyNTs	DPV	35 – 960	0.2989	0.04278*	-	62
EDDPT/GO/CPE	DPV	1.5 – 600	0.65	0.0754*	drug sample	54
PDMS@cZIF/GCE	DPV	1.0 – 60	0.13	0.112*	rat blood sample	63
CPE/Fe_3O_4	DPV	0.4 – 270	0.05	0.0555*	human blood plasma sample	64
MIP/AuNPs/GCE	DPV	0.09 – 100	0.076	-	drug sample	65
CdO/PANI/mpg-C_3N_4/GCE	DPV	0.05 – 80 100 – 1000	0.011	0.0393* 0.0066*	human blood serum	66
AZOTEG/CPE	DPV	0.1 – 75	0.013	0.5312*	drug sample	67
CoAlOOH/GO/GCE	DPV	0.1 – 25	0.023	1.5323	drug sample	53
WO_3NWs-ITO	DPV	0.5 – 250	0.086	0.0491	drug sample	This work

* This value was calculated from the equation of the calibration plot given in the publication.

Table 4.1. Comparison of major analytical characteristics of the different modified electrodes for detection of Ep.

It can be seen that the analytical performance of WO_3NWs-ITO is comparable to previous reports on the determination of EP, further proving the effectiveness of the BCP patterning strategy for cheap and scalable fabrication of sensing devices. The repeatability of WO_3NWs-ITO was also tested by monitoring seven repetitive measurements of 10 μM EP using the same electrode. The relative standard deviation (RSD) is found to be 1.95% for repeatability, thereby revealing a high degree of durability of WO_3NWs-ITO with stable responses.

To assess the selectivity of the WO_3NWs-ITO sensor, the interfering effect of some potential coexisting compounds (A, G, DA, Phe, AA, UA, and Glu) was examined using the DPV technique. In the oxidation peak potential of EP, the peak currents of the interfering compounds (100 μM) in 0.1 M acetate buffer solution (pH 5.4) were compared and the results were summarized in **Figure 6**. No oxidation peaks were found for A, G, Phe and Glu in the potential range of the study. As for other compounds, the peak potential separation values are over 100 mV,[68] and the current deviations caused by the interferents are not exceeding 10%. These results exhibit that WO_3NWs-ITO has acceptable selectivity for the detection of EP.

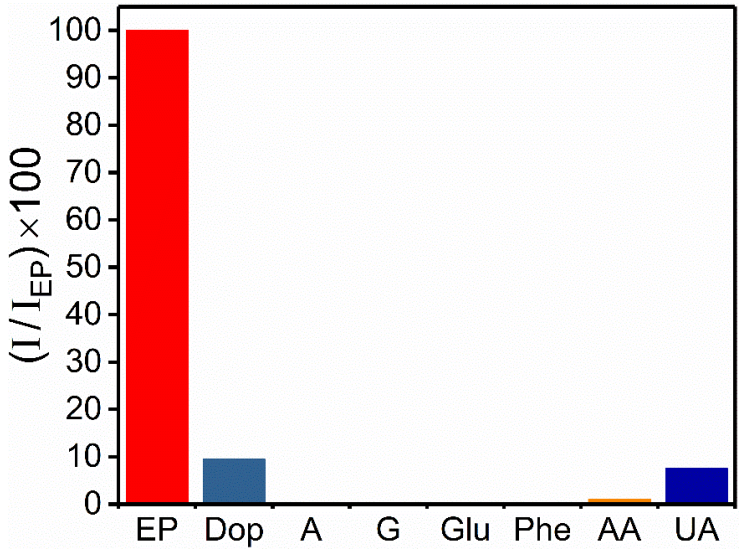

Figure 4.7. Effect of various interfering compounds for the detection of EP on WO_3NWs-ITO.

The practical applicability of WO_3NWs-ITO was evaluated by detecting the EP amount contained within two kinds of commercial drug samples (epinephrine ampules) using the standard addition method. Prior to the measurement, the injection solution containing EP

(1 mg mL^{-1}) was diluted to the working concentration range of WO_3NWs-ITO with 0.1 M (pH 5.4) acetate buffer solution. The results are listed in **Table 4.2**. The practical test values are very close to the standard value of the EP ampule label, which indicates satisfactory recovery percentages for the detection of EP in practical applications.

Sample	Given (μM)	Added (μM)	Found (μM)	Recovery (%)
	20	0	19.60	–
Sample 1	20	10	29.41	98.03
	20	20	39.25	98.12
	20	0	19.54	–
Sample 2	20	10	29.30	97.67
	20	20	39.10	97.75

Table 4.2. Determination of EP in the drug samples using WO_3NWs-ITO.

4.5. Conclusion:

In summary, we have demonstrated the successful synthesis, development and electrochemical testing of a novel nanostructured WO_3 catalytic device using a low-cost and highly scalable BCP-based approach. The water oxidation properties of WO_3NWs-ITO electrode were investigated in the absence and presence of light illumination. Secondly, the sensing capabilities of the WO_3NWs-ITO electrode were examined for the oxidation of EP, demonstrating an enhanced oxidation peak current and robust catalytic activity. The linear concentration range for the WO_3NWs-ITO electrode was measured to be 0.5 μM – 250 μM, with a notably low detection limit of 0.086 μM. Moreover, the WO_3NWs-ITO electrode displayed excellent stability and reproducibility, along with a high degree of selectivity in the presence of a range of interfering compounds. Testing with commercial drug samples containing EP also showed a high degree of sensitivity, proving the feasibility of such a device for its potential use in commercial applications. In summary, the results of this study provide a new candidate method for synthesizing highly responsive and selective WO_3-based electrocatalytic devices, further reinforcing the practicality of BCP-based fabrication routes for constructing catalytic materials.

4.6. References:

1. Wang, J.; van Ree, T.; Wu, Y.; Zhang, P.; Gao, L., 8 - Metal oxide semiconductors for solar water splitting. In *Metal Oxides in Energy Technologies*, Wu, Y., Ed. Elsevier: 2018; pp 205-249.
2. Thu, C.; Ehrenreich, P.; Wong, K. K.; Zimmermann, E.; Dorman, J.; Wang, W.; Fakharuddin, A.; Putnik, M.; Drivas, C.; Koutsoubelitis, A.; Vasilopoulou, M.; Palilis, L. C.; Kennou, S.; Kalb, J.; Pfadler, T.; Schmidt-Mende, L., Role of the Metal-Oxide Work Function on Photocurrent Generation in Hybrid Solar Cells. *Scientific Reports* **2018,** *8* (1), 3559.
3. Concina, I.; Ibupoto, Z. H.; Vomiero, A., Semiconducting Metal Oxide Nanostructures for Water Splitting and Photovoltaics. *Advanced Energy Materials* **2017,** *7* (23), 1700706.
4. Comini, E.; Baratto, C.; Faglia, G.; Ferroni, M.; Vomiero, A.; Sberveglieri, G., Quasi-one dimensional metal oxide semiconductors: Preparation, characterization and application as chemical sensors. *Progress in Materials Science* **2009,** *54* (1), 1-67.
5. Teusch, T.; Klüner, T., Understanding the Water Splitting Mechanism on WO3(001)—A Theoretical Approach. *The Journal of Physical Chemistry C* **2019,** *123* (46), 28233-28240.
6. Chen, H.; Bo, R.; Tran-Phu, T.; Liu, G.; Tricoli, A., One-Step Rapid and Scalable Flame Synthesis of Efficient WO3 Photoanodes for Water Splitting. *ChemPlusChem* **2018,** *83* (7), 569-576.
7. Staerz, A.; Kobald, A.; Russ, T.; Weimar, U.; Hémeryck, A.; Barsan, N., Thermal Water Splitting on the WO3 Surface: Experimental Proof. *ACS Applied Electronic Materials* **2020,** *2* (10), 3254-3262.
8. Ma, M.; Zhang, K.; Li, P.; Jung, M. S.; Jeong, M. J.; Park, J. H., Dual Oxygen and Tungsten Vacancies on a WO3 Photoanode for Enhanced Water Oxidation. *Angewandte Chemie International Edition* **2016,** *55* (39), 11819-11823.
9. Dey, A., Semiconductor metal oxide gas sensors: A review. *Materials Science and Engineering: B* **2018,** *229*, 206-217.
10. Staerz, A.; Somacescu, S.; Epifani, M.; Kida, T.; Weimar, U.; Barsan, N., WO3-Based Gas Sensors: Identifying Inherent Qualities and Understanding the Sensing Mechanism. *ACS Sensors* **2020,** *5* (6), 1624-1633.
11. Takács, M.; Dücső, C.; Lábadi, Z.; Pap, A. E., Effect of Hexagonal WO3 Morphology on NH3 Sensing. *Procedia Engineering* **2014,** *87*, 1011-1014.
12. Boudiba, A.; Zhang, C.; Bittencourt, C.; Umek, P.; Olivier, M.-G.; Snyders, R.; Debliquy, M., SO2 Gas Sensors based on WO3 Nanostructures with Different Morphologies. *Procedia Engineering* **2012,** *47*, 1033-1036.
13. Horprathum, M.; Srichaiyaperk, T.; Samransuksamer, B.; Wisitsoraat, A.; Eiamchai, P.; Limwichean, S.; Chananonnawathorn, C.; Aiempanakit, K.; Nuntawong, N.; Patthanasettakul, V.; Oros, C.; Porntheeraphat, S.; Songsiriritthigul, P.; Nakajima, H.; Tuantranont, A.; Chindaudom, P., Ultrasensitive Hydrogen Sensor Based on Pt-Decorated WO3 Nanorods Prepared by Glancing-Angle dc Magnetron Sputtering. *ACS Applied Materials & Interfaces* **2014,** *6* (24), 22051-22060.
14. Staerz, A.; Weimar, U.; Barsan, N., Understanding the Potential of WO_3 Based Sensors for Breath Analysis. *Sensors (Basel)* **2016,** *16* (11), 1815.
15. Su, J.; Feng, X.; Sloppy, J. D.; Guo, L.; Grimes, C. A., Vertically Aligned WO3 Nanowire Arrays Grown Directly on Transparent Conducting Oxide Coated Glass: Synthesis and Photoelectrochemical Properties. *Nano Letters* **2011,** *11* (1), 203-208.

16. Li, Y.; Zhang, J. Z., Hydrogen generation from photoelectrochemical water splitting based on nanomaterials. *Laser & Photonics Reviews* **2010,** *4* (4), 517-528.
17. Nunes, D.; Pimentel, A.; Gonçalves, A.; Pereira, S.; Branquinho, R.; Barquinha, P.; Fortunato, E.; Martins, R., Metal oxide nanostructures for sensor applications. *Semiconductor Science and Technology* **2019,** *34* (4), 043001.
18. Gogova, D.; Stoyanov, G.; Gesheva, K. A., Optimization of the growth rate of electrochromic WO3 coatings, in-situ grown by chemical vapor deposition at atmospheric pressure. *Renewable Energy* **1996,** *8* (1), 546-550.
19. Cantalini, C.; Wlodarski, W.; Li, Y.; Passacantando, M.; Santucci, S.; Comini, E.; Faglia, G.; Sberveglieri, G., Investigation on the O3 sensitivity properties of WO3 thin films prepared by sol–gel, thermal evaporation and r.f. sputtering techniques. *Sensors and Actuators B: Chemical* **2000,** *64* (1), 182-188.
20. Diao, J.; Yuan, W.; Qiu, Y.; Cheng, L.; Guo, X., A hierarchical oxygen vacancy-rich WO3 with "nanowire-array-on-nanosheet-array" structure for highly efficient oxygen evolution reaction. *Journal of Materials Chemistry A* **2019,** *7* (12), 6730-6739.
21. Zhang, J.; Chang, X.; Li, C.; Li, A.; Liu, S.; Wang, T.; Gong, J., WO3 photoanodes with controllable bulk and surface oxygen vacancies for photoelectrochemical water oxidation. *Journal of Materials Chemistry A* **2018,** *6* (8), 3350-3354.
22. Zhu, T.; Chong, M. N.; Chan, E. S., Nanostructured Tungsten Trioxide Thin Films Synthesized for Photoelectrocatalytic Water Oxidation: A review. *ChemSusChem* **2014,** *7* (11), 2974-2997.
23. Ansari, S.; Ansari, M. S.; Satsangee, S. P.; Jain, R., WO3 decorated graphene nanocomposite based electrochemical sensor: A prospect for the detection of anti-anginal drug. *Analytica Chimica Acta* **2019,** *1046*, 99-109.
24. Jing, S.; Zheng, H.; Zhao, L.; Qu, L.; Yu, L., A novel electrochemical sensor based on WO3 nanorods-decorated poly(sodium 4-styrenesulfonate) functionalized graphene nanocomposite modified electrode for detecting of puerarin. *Talanta* **2017,** *174*, 477-485.
25. Baytak, A. K.; Duzmen, S.; Teker, T.; Aslanoglu, M., A novel composite electrode based on tungsten oxide nanoparticles and carbon nanotubes for the electrochemical determination of paracetamol. *Materials Science and Engineering: C* **2015,** *57*, 164-170.
26. Kafizas, A.; Francàs, L.; Sotelo-Vazquez, C.; Ling, M.; Li, Y.; Glover, E.; McCafferty, L.; Blackman, C.; Darr, J.; Parkin, I., Optimizing the Activity of Nanoneedle Structured WO3 Photoanodes for Solar Water Splitting: Direct Synthesis via Chemical Vapor Deposition. *The Journal of Physical Chemistry C* **2017,** *121* (11), 5983-5993.
27. Hawker, C. J.; Russell, T. P., Block Copolymer Lithography: Merging "Bottom-Up" with "Top-Down" Processes. *MRS Bulletin* **2005,** *30* (12), 952-966.
28. Bates, C. M.; Maher, M. J.; Janes, D. W.; Ellison, C. J.; Willson, C. G., Block Copolymer Lithography. *Macromolecules* **2014,** *47* (1), 2-12.
29. Bates, F.; Fredrickson, G., Block Copolymers—Designer Soft Materials. *Physics Today* **1999,** *52*, 32-38.
30. Cummins, C.; Ghoshal, T.; Holmes, J. D.; Morris, M. A., Strategies for Inorganic Incorporation using Neat Block Copolymer Thin Films for Etch Mask Function and Nanotechnological Application. *Advanced Materials* **2016,** *28* (27), 5586-5618.

31. Giraud, E. C.; Mokarian-Tabari, P.; Toolan, D. T. W.; Arnold, T.; Smith, A. J.; Howse, J. R.; Topham, P. D.; Morris, M. A., Highly Ordered Titanium Dioxide Nanostructures via a Simple One-Step Vapor-Inclusion Method in Block Copolymer Films. *ACS Applied Nano Materials* **2018,** *1* (7), 3426-3434.
32. Cummins, C.; Lundy, R.; Walsh, J. J.; Ponsinet, V.; Fleury, G.; Morris, M. A., Enabling future nanomanufacturing through block copolymer self-assembly: A review. *Nano Today* **2020,** *35*, 100936.
33. Zou, Y.; Zhou, X.; Ma, J.; Yang, X.; Deng, Y., Recent advances in amphiphilic block copolymer templated mesoporous metal-based materials: assembly engineering and applications. *Chemical Society Reviews* **2020,** *49* (4), 1173-1208.
34. Bas, S. Z.; Cummins, C.; Borah, D.; Ozmen, M.; Morris, M. A., Electrochemical Sensing of Hydrogen Peroxide Using Block Copolymer Templated Iron Oxide Nanopatterns. *Analytical Chemistry* **2018,** *90* (2), 1122-1128.
35. Bas, S. Z.; Cummins, C.; Selkirk, A.; Borah, D.; Ozmen, M.; Morris, M. A., A Novel Electrochemical Sensor Based on Metal Ion Infiltrated Block Copolymer Thin Films for Sensitive and Selective Determination of Dopamine. *ACS Applied Nano Materials* **2019,** *2* (11), 7311-7318.
36. Zhu, Y.; Lin, Q.; Zhong, Y.; Tahini, H. A.; Shao, Z.; Wang, H., Metal oxide-based materials as an emerging family of hydrogen evolution electrocatalysts. *Energy & Environmental Science* **2020,** *13* (10), 3361-3392.
37. Cummins, C.; Gangnaik, A.; Kelly, R. A.; Borah, D.; O'Connell, J.; Petkov, N.; Georgiev, Y. M.; Holmes, J. D.; Morris, M. A., Aligned silicon nanofins via the directed self-assembly of PS-b-P4VP block copolymer and metal oxide enhanced pattern transfer. *Nanoscale* **2015,** *7* (15), 6712-6721.
38. Cummins, C.; Bell, A. P.; Morris, M. A., Creating Active Device Materials for Nanoelectronics Using Block Copolymer Lithography. *Nanomaterials (Basel)* **2017,** *7* (10), 304.
39. Ghoshal, T.; Maity, T.; Senthamaraikannan, R.; Shaw, M. T.; Carolan, P.; Holmes, J. D.; Roy, S.; Morris, M. A., Size and space controlled hexagonal arrays of superparamagnetic iron oxide nanodots: magnetic studies and application. *Scientific Reports* **2013,** *3* (1), 2772.
40. Barreca, D.; Carta, G.; Gasparotto, A.; Rossetto, G.; Tondello, E.; Zanella, P., A Study of Nanophase Tungsten Oxides Thin Films by XPS. *Surface Science Spectra* **2001,** *8* (4), 258-267.
41. Senthil, K.; Yong, K., Growth and characterization of stoichiometric tungsten oxide nanorods by thermal evaporation and subsequent annealing. *Nanotechnology* **2007,** *18* (39), 395604.
42. Wei, Z.; Akbari, M. K.; Hai, Z.; Ramachandran, R. K.; Detavernier, C.; Verpoort, F.; Kats, E.; Xu, H.; Hu, J.; Zhuiykov, S., Ultra-thin sub-10 nm Ga2O3-WO3 heterostructures developed by atomic layer deposition for sensitive and selective C2H5OH detection on ppm level. *Sensors and Actuators B: Chemical* **2019,** *287*, 147-156.
43. Santato, C.; Odziemkowski, M.; Ulmann, M.; Augustynski, J., Crystallographically Oriented Mesoporous WO3 Films: Synthesis, Characterization, and Applications. *Journal of the American Chemical Society* **2001,** *123* (43), 10639-10649.
44. Singh, T.; Müller, R.; Singh, J.; Mathur, S., Tailoring surface states in WO3 photoanodes for efficient photoelectrochemical water splitting. *Applied Surface Science* **2015,** *347*, 448-453.

45. Daniel, M. F.; Desbat, B.; Lassegues, J. C.; Gerand, B.; Figlarz, M., Infrared and Raman study of WO3 tungsten trioxides and WO3, xH2O tungsten trioxide tydrates. *Journal of Solid State Chemistry* **1987,** *67* (2), 235-247.
46. Qu, H.; Zhang, X.; Pan, L.; Gao, Z.; Ma, L.; Zhao, J.; Li, Y., One-pot preparation of crystalline-amorphous double-layer structured WO3 films and their electrochromic properties. *Electrochimica Acta* **2014,** *148*, 46-52.
47. Lee, J.-S.; Cho, J.; You, C.-Y., Growth and characterization of α and β-phase tungsten films on various substrates. *Journal of Vacuum Science & Technology A* **2016,** *34* (2), 021502.
48. Gonçalves, R. H.; Leite, L. D. T.; Leite, E. R., Colloidal WO3 Nanowires as a Versatile Route to Prepare a Photoanode for Solar Water Splitting. *ChemSusChem* **2012,** *5* (12), 2341-2347.
49. Shahamirifard, S. A.; Ghaedi, M., A new electrochemical sensor for simultaneous determination of arbutin and vitamin C based on hydroxyapatite-ZnO-Pd nanoparticles modified carbon paste electrode. *Biosensors and Bioelectronics* **2019,** *141*, 111474.
50. Wu, Q.; Bu, Q.; Li, S.; Lin, Y.; Zou, X.; Wang, D.; Xie, T., Enhanced interface charge transfer via n-n WO3/Ti–Fe2O3 heterojunction formation for water splitting. *Journal of Alloys and Compounds* **2019,** *803*, 1105-1111.
51. Huang, X.; Zhao, G.; Wang, G., Sub-nano CoOx attached onto WO3 for efficient photocatalytic and photoelectrochemical water oxidation. *Journal of Materials Chemistry A* **2017,** *5* (47), 24631-24635.
52. Sainz, R.; del Pozo, M.; Vilas-Varela, M.; Castro-Esteban, J.; Pérez Corral, M.; Vázquez, L.; Blanco, E.; Peña, D.; Martín-Gago, J. A.; Ellis, G. J.; Petit-Domínguez, M. D.; Quintana, C.; Casero, E., Chemically synthesized chevron-like graphene nanoribbons for electrochemical sensors development: determination of epinephrine. *Scientific Reports* **2020,** *10* (1), 14614.
53. Wu, C.; Li, J.; Liu, X.; Zhang, H.; Li, R.; Wang, G.; Wang, Z.; Li, Q.; Shangguan, E., Simultaneous voltammetric determination of epinephrine and acetaminophen using a highly sensitive CoAl-OOH/reduced graphene oxide sensor in pharmaceutical samples and biological fluids. *Materials Science and Engineering: C* **2021,** *119*, 111557.
54. Tezerjani, M. D.; Benvidi, A.; Dehghani Firouzabadi, A.; Mazloum-Ardakani, M.; Akbari, A., Epinephrine electrochemical sensor based on a carbon paste electrode modified with hydroquinone derivative and graphene oxide nano-sheets: Simultaneous determination of epinephrine, acetaminophen and dopamine. *Measurement* **2017,** *101*, 183-189.
55. Ponnaiah, S. K.; Periakaruppan, P.; Vellaichamy, B., New Electrochemical Sensor Based on a Silver-Doped Iron Oxide Nanocomposite Coupled with Polyaniline and Its Sensing Application for Picomolar-Level Detection of Uric Acid in Human Blood and Urine Samples. *The Journal of Physical Chemistry B* **2018,** *122* (12), 3037-3046.
56. Cai, Z.-X.; Li, H.-Y.; Yang, X.-N.; Guo, X., NO sensing by single crystalline WO3 nanowires. *Sensors and Actuators B: Chemical* **2015,** *219*, 346-353.
57. Anithaa, A. C.; Lavanya, N.; Asokan, K.; Sekar, C., WO3 nanoparticles based direct electrochemical dopamine sensor in the presence of ascorbic acid. *Electrochimica Acta* **2015,** *167*, 294-302.
58. Li, Y.; Gao, Y.; Cao, Y.; Li, H., Electrochemical sensor for bisphenol A determination based on MWCNT/melamine complex modified GCE. *Sensors and Actuators B: Chemical* **2012,** *171-172*, 726-733.

59. Villalonga, R.; Díez, P.; Eguílaz, M.; Martínez, P.; Pingarrón, J. M., Supramolecular Immobilization of Xanthine Oxidase on Electropolymerized Matrix of Functionalized Hybrid Gold Nanoparticles/Single-Walled Carbon Nanotubes for the Preparation of Electrochemical Biosensors. *ACS Applied Materials & Interfaces* **2012,** *4* (8), 4312-4319.
60. Karim-Nezhad, G.; Khorablou, Z., Selective analysis of epinephrine in the presence of uric acid by using an amplified electrochemical sensor employing a gold nanoparticle decorated cysteic acid film. *Analytical Methods* **2017,** *9* (45), 6394-6402.
61. Lavanya, N.; Sekar, C., Electrochemical sensor for simultaneous determination of epinephrine and norepinephrine based on cetyltrimethylammonium bromide assisted SnO2 nanoparticles. *Journal of Electroanalytical Chemistry* **2017,** *801*, 503-510.
62. Mao, H.; Zhang, H.; Jiang, W.; Liang, J.; Sun, Y.; Zhang, Y.; Wu, Q.; Zhang, G.; Song, X.-M., Poly(ionic liquid) functionalized polypyrrole nanotubes supported gold nanoparticles: An efficient electrochemical sensor to detect epinephrine. *Materials Science and Engineering: C* **2017,** *75*, 495-502.
63. Zhang, J.; Wang, D.; Li, Y., Ratiometric Electrochemical Sensors Associated with Self-Cleaning Electrodes for Simultaneous Detection of Adrenaline, Serotonin, and Tryptophan. *ACS Applied Materials & Interfaces* **2019,** *11* (14), 13557-13563.
64. Arani, N. H.; Ghoreishi, S. M.; Khoobi, A., Increasing the electrochemical system performance using a magnetic nanostructured sensor for simultaneous determination of l-tyrosine and epinephrine. *Analytical Methods* **2019,** *11* (9), 1192-1198.
65. Liu, F.; Kan, X., Conductive imprinted electrochemical sensor for epinephrine sensitive detection and double recognition. *Journal of Electroanalytical Chemistry* **2019,** *836*, 182-189.
66. Bonyadi, S.; Ghanbari, K.; Ghiasi, M., All-electrochemical synthesis of a three-dimensional mesoporous polymeric g-C3N4/PANI/CdO nanocomposite and its application as a novel sensor for the simultaneous determination of epinephrine, paracetamol, mefenamic acid, and ciprofloxacin. *New Journal of Chemistry* **2020,** *44* (8), 3412-3424.
67. Avcı, O.; Perk, B.; Ören Varol, T.; Tepeli Büyüksünetçi, Y.; Hakli, Ö.; Anik, Ü., A polyoxy group branched diazo dye as an alternative material for the fabrication of an electrochemical epinephrine sensor. *New Journal of Chemistry* **2019,** *43* (47), 18575-18581.
68. Demir, N.; Atacan, K.; Ozmen, M.; Bas, S. Z., Design of a new electrochemical sensing system based on MoS2–TiO2/reduced graphene oxide nanocomposite for the detection of paracetamol. *New Journal of Chemistry* **2020,** *44* (27), 11759-11767.

4.7 – Chapter 4 Appendix

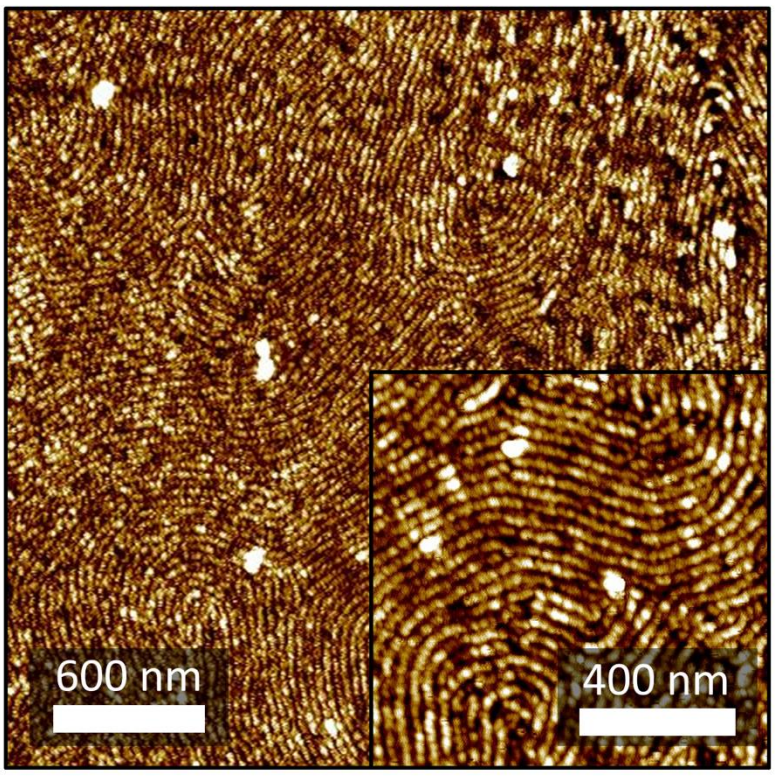

Figure S4.1: AFM images of the WO_3 nanowires on a plain Si substrate.

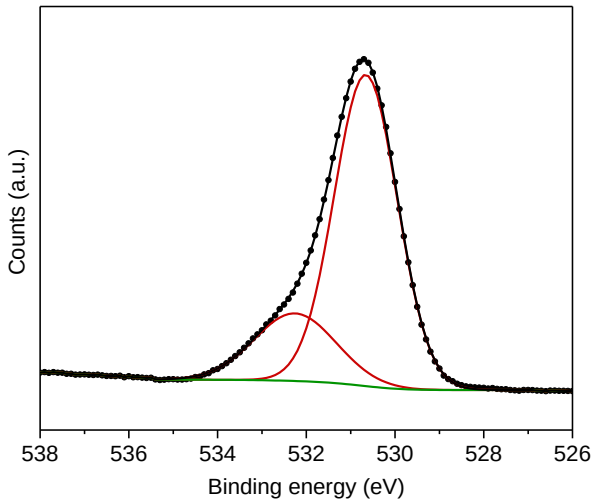

Figure S4.2: High-resolution XPS scan of the O1s region of the WO_3 nanowire array on ITO.

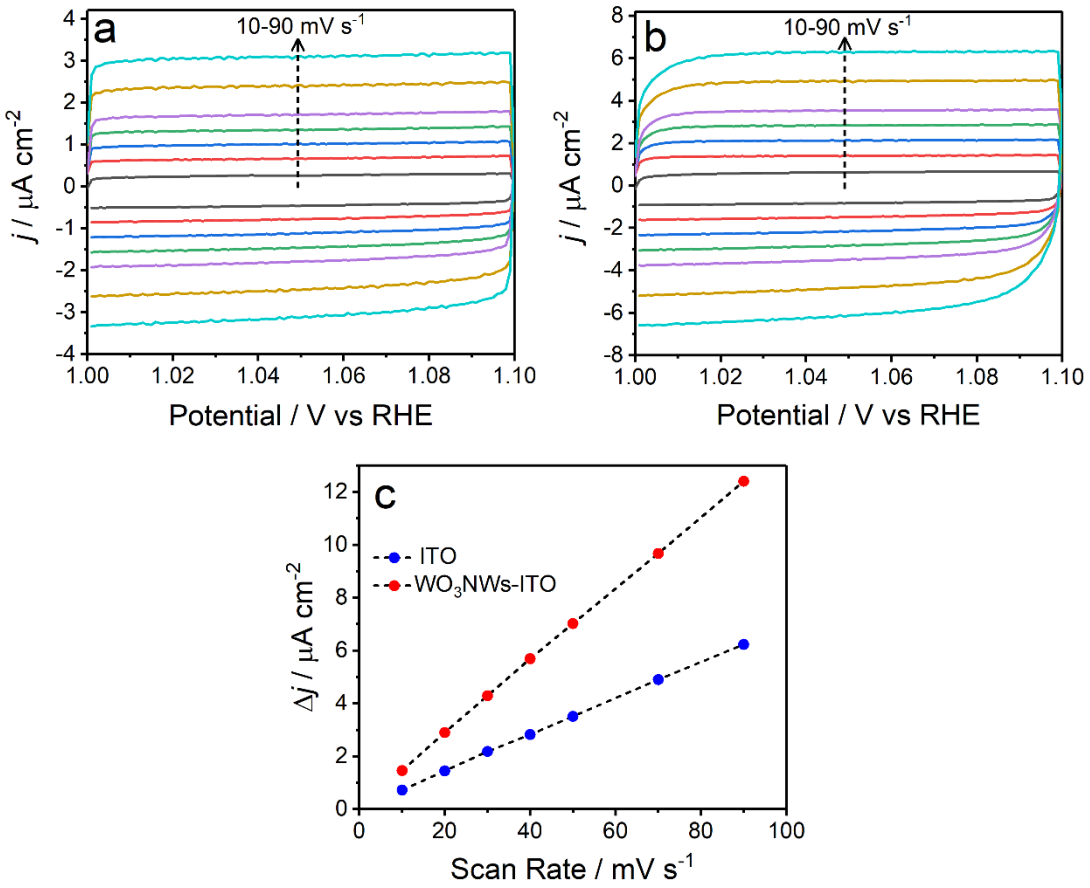

Figure S4.3. Cyclic voltammograms of **(a)** ITO and **(b)** WO_3NWs-ITO electrodes at different scan rates (10, 20, 30, 40, 50, 70, and 90 mV s^{-1}). **(c)** Plots of C_{dl} linear fitting of the capacitive currents of electrodes.

5. Conclusions & Future Work:

Despite decades of extensive research, BCP-derived nanostructures remain a rapidly evolving field with an ever-increasing diversity of applications. The ability of BCP systems to easily self-assemble into sub-10 nm features originally garnered interest from an electronics perspective, however in more recent times BCPs have found use in applications such as optics, sensing, membranes among many others.[1] The adoption of BCP-based materials across such disparate fields is credited to their unique production advantages, which include low cost, ease of scalability, dimensional tuneability, and high degree of ordering over large areas. Nonetheless, there remains a number of critical issues that hinder the successful translation of BCP-based technology from the research lab to industry. In the case of optical applications such as antireflective coatings, the ability to reliably produce patterns with domain periods in excess of 150 nm is one of the most crucial roadblocks to industrial adoption.[2] Additionally, for applications such as catalysis or sensing, a greater degree of understanding and control over the formation and performance of BCP-templated metal and metal oxide structures is essential.[3] This thesis aimed to address these challenges by firstly, developing a strategy for rapid and repeatable self-assembly of large-period BCP structures, and secondly, constructing and testing novel catalytic materials via BCP templating.

In chapter 2, a strategy for the rapid self-assembly of an UHMW PS-*b*-P2VP BCP system was developed through the use of a custom-designed SVA chamber. We showed that in order to get such UHMW systems to self-assemble, the BCP films must be swollen to very high levels of solvent concentration. Lamellar structures with domain periods of ~190 nm were fabricated in rapid annealing times of ~10 minutes through a controlled SVA process. The orientational ordering of the structures was shown to be directly proportional to the solvent concentration, up to a maximum concentration value at which the films undergo an order-disorder transition to a melt-like state. The length of time that a BCP film was held at a particular solvent concentration, along with the swelling rate, did not noticeably influence the ordering of the BCP system. The resulting lamellar patterns were successfully utilised for pattern transfer using a liquid phase infiltration method, yielding high aspect ratio nanowall structures. In terms of future work, this strategy should be expanded to include multiple UHMW BCP systems and molecular weights. Additionally, the independent role of the solvent mixture in facilitating the self-

assembly warrants further examination – ideally using the Hansen parameters as a guideline for optimal polymer-solvent matching. The ultimate goal of this work should be to develop a process whereby the feature sizes and morphology of larger BCP systems can be precisely tailored to a desired structure. With regards to producing BCP domain spacings in excess of 200 nm, it seems likely that future breakthroughs will rely on a combination of approaches for UHMW BCP self-assembly that have been individually developed in recent years; these include the strategy outlined in this chapter, the work by Doerk et al. using BCP-homopolymer mixtures,[4] along with tailoring surface energies and solvent choices as described by Cummins et al.[5]

Chapter 3 outlined the synthesis and characterisation of freestanding 3D Au and Pt nanowall structures via BCP templating. The UHMW PS-*b*-P2VP system from chapter 2 was utilised as the scaffold for coordinating metal ions via a LPI strategy. Upon O_2 plasma etching, the polymer scaffold was removed leaving 3D metal nanostructures on Si substrates. A positive correlation was observed between the thickness of the BCP scaffold film and the height of the Au or Pt structures, with maximum heights of over 225 nm achieved using a ~370 nm thick BCP film. The Au nanowall structures were utilised as photocatalysts for the degradation of methyl orange, revealing a positive correlation between the photocatalytic performance and the height of the Au features. The reusability of the Au structures was examined via multiple degradation runs on the same samples, which showed little or no decrease in catalytic performance during each subsequent test. Nonetheless, the overall catalytic performance of the Au structures was mediocre, with exposure times in excess of 5 hours required for significant degradation. Since the thickness appeared to play a significant role in the catalytic performance, a future study should examine whether structures created using 'bulk' BCP films (with thicknesses in excess of 1 μm) can further expedite the degradation process. Moreover, the influence of the BCP domain period and/or morphology on the catalytic performance should be thoroughly examined. Recently published work also documented the ability of BCP templates to coordinate multiple metal species for catalytic purposes;[6] hence this may be an additional avenue by which to further fine-tune the performance of these structures.

Chapter 4 details the fabrication of a novel WO_3-ITO catalytic device using a PS-*b*-P4VP BCP system as a template atop an ITO substrate. A BCP layer consisting of a cylindrical

PS-*b*-P4VP system was firstly deposited on ITO substrates, which was then micro-phase separated using SVA. A tungsten chloride precursor was selectively infiltrated into the P4VP domains using a LPI method, which after UV/O_3 treatment yielded large-area tungsten oxide surface nanowires. The resulting device was successfully applied for use as a photoanode for the oxygen evolution reaction. The epinephrine sensing capabilities of the device were also explored, which exhibited high durability over multiple measurements along with excellent interference abilities in the presence of interfering species. Additionally, the epinephrine concentrations of commercial drug samples were determined to a high degree of accuracy. Similarly to chapter 3, one possible avenue of future research would be to examine whether the thickness or morphology of the metal oxide structures have any effect on the device performance.

While this thesis has provided new strategies and techniques for expanding the frontiers of BCP applications, many challenges are yet to be overcome before such applications can become industrially viable. With regards to large period BCP patterning, the true 'size limit' has yet to be definitively determined – this will likely require broad studies encompassing multiple BCP families and a combination of self-assembly strategies. The potential of more 'exotic' systems such as bottlebrush or rod-coil BCPs to produce large features is also relatively unexplored. In term of producing applied materials via metal/metal oxide BCP templating, there remains a critical lack of understanding of the precise mechanisms of precursor infiltration; more specifically, why do certain precursors coordinate well with certain BCP systems while others do not? Although very recent work has begun to address this question for vapour phase precursors,[7] few studies currently exist that examine the mechanisms of LPI.

In summary, while huge progress has been made in the understanding and development of novel BCP materials, there remains a number of roadblocks that will challenge the future direction of the field. Addressing the aforementioned issues in this chapter will be essential to further the adoption of BCP technologies in modern society.

5.1. References:

1. Cummins, C.; Lundy, R.; Walsh, J. J.; Ponsinet, V.; Fleury, G.; Morris, M. A., Enabling future nanomanufacturing through block copolymer self-assembly: A review. *Nano Today* **2020,** *35*, 100936.
2. Mir, S. H.; Rydzek, G.; Nagahara, L. A.; Khosla, A.; Mokarian-Tabari, P., Review—Recent Advances in Block-Copolymer Nanostructured Subwavelength Antireflective Surfaces. *Journal of The Electrochemical Society* **2019,** *167* (3), 037502.
3. Cummins, C.; Morris, M. A., Using block copolymers as infiltration sites for development of future nanoelectronic devices: Achievements, barriers, and opportunities. *Microelectronic Engineering* **2018,** *195*, 74-85.
4. Doerk, G. S.; Li, R.; Fukuto, M.; Yager, K. G., Wet Brush Homopolymers as "Smart Solvents" for Rapid, Large Period Block Copolymer Thin Film Self-Assembly. *Macromolecules* **2020,** *53* (3), 1098-1113.
5. Cummins, C.; Alvarez-Fernandez, A.; Bentaleb, A.; Hadziioannou, G.; Ponsinet, V.; Fleury, G., Strategy for Enhancing Ultrahigh-Molecular-Weight Block Copolymer Chain Mobility to Access Large Period Sizes (>100 nm). *Langmuir* **2020,** *36* (46), 13872-13880.
6. Lee, J.; Mishra, A. K.; Choi, C.; Kim, D.; Kim, E. Y.; Yong, K.; Kim, J. K., Three-Dimensional Nanoporous Metal Structures from Poly(2-vinylpyridine)-block-Poly(4-vinylpyridine) Copolymer Thin Film. *ACS Applied Materials & Interfaces* **2020,** *12* (13), 15667-15674.
7. Ren, Y.; McGuinness, E. K.; Huang, C.; Joseph, V. R.; Lively, R. P.; Losego, M. D., Reaction–Diffusion Transport Model to Predict Precursor Uptake and Spatial Distribution in Vapor-Phase Infiltration Processes. *Chemistry of Materials* **2021**.